

DTIC FILE COPY

# HARDENING SURVEILLANCE ILLUMINATION USING AIRCRAFT ANTENNAS

J. P. Donohoe  
C. D. Taylor

Mississippi State University  
United International Engineering, Incorporated  
Albuquerque, NM 87106

June 1990

Final Report

DTIC  
ELECTE  
JUL 30 1990  
S D & D

Approved for public release; distribution unlimited.

Weapons Laboratory  
Air Force Systems Command  
Kirtland Air Force Base, NM 87117-6008

AD-A225 143



This final report was prepared by the Weapons Laboratory, Kirtland Air Force Base, New Mexico, under Job Order 37630167. Mr Tyrone C. Tran (NTAAT) was the Laboratory Project Officer-in-Charge.

When Government drawings, specifications, or other data are used for any purpose other than in connection with a definitely Government-related procurement, the United States Government incurs no responsibility or any obligation whatsoever. The fact that the Government may have formulated or in any way supplied the said drawings, specifications, or other data, is not to be regarded by implication, or otherwise in any manner construed, as licensing the holder, or any other person or corporation; or as conveying any rights or permission to manufacture, use, or sell any patented invention that may in any way be related thereto.

This report has been authored by employees and a contractor of the United States Government. Accordingly, the United States Government retains a nonexclusive royalty-free license to publish or reproduce the material contained herein, or allow others to do so, for the United States Government purposes.

This report has been reviewed by the Public Affairs Office and is releasable to the National Technical Information Service (NTIS). At NTIS, it will be available to the general public, including foreign nationals.

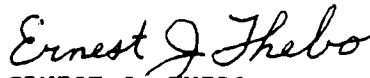
If your address has changed, if you wish to be removed from our mailing list, or if your organization no longer employs the addressee, please notify WL/NTAAT, Kirtland AFB, NM 87117-6008 to help us maintain a current mailing list.

This report has been reviewed and is approved for publication.

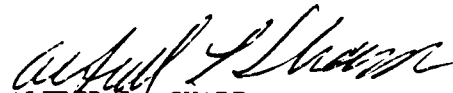


TYRONE C. TRAN  
Project Officer

FOR THE COMMANDER



ERNEST J. THEBO  
Major, USAF  
Chief, Applications Branch



ALFRED L. SHARP  
Chief, Aircraft and Missiles Division

DO NOT RETURN COPIES OF THIS REPORT UNLESS CONTRACTUAL OBLIGATIONS OR NOTICE ON A SPECIFIC DOCUMENT REQUIRES THAT IT BE RETURNED.

# REPORT DOCUMENTATION PAGE

Form Approved  
OMB No. 0704-0188

Public reporting burden for this collection of information is estimated to average 1 hour per response, including the time for reviewing instructions, searching existing data sources, gathering and maintaining the data needed, and completing and reviewing the collection of information. Send comments regarding this burden estimate or any other aspect of this collection of information, including suggestions for reducing this burden, to Washington Headquarters Services, Directorate for Information Operations and Reports, 1215 Jefferson Davis Highway, Suite 1204, Arlington, VA 22202-4302, and to the Office of Management and Budget, Paperwork Reduction Project (0704-0188), Washington, DC 20503

<b>1. AGENCY USE ONLY (Leave blank)</b>		<b>2. REPORT DATE</b> June 1990	<b>3. REPORT TYPE AND DATES COVERED</b> Final Report - Mar 89-Jan 90	
<b>4. TITLE AND SUBTITLE</b> HARDENING SURVEILLANCE ILLUMINATION USING AIRCRAFT ANTENNAS			<b>5. FUNDING NUMBERS</b> JON: 3763 TA: 01 WU: 67 PE: 64711F C: F29601-88-C-0001	
<b>6. AUTHOR(S)</b> Donohoe, J. P. Taylor, C. D.				
<b>7. PERFORMING ORGANIZATION NAME(S) AND ADDRESS(ES)</b> Mississippi State University United International Engineering, Incorporated Albuquerque, NM 87106			<b>8. PERFORMING ORGANIZATION REPORT NUMBER</b>	
<b>9. SPONSORING / MONITORING AGENCY NAME(S) AND ADDRESS(ES)</b> Weapons Laboratory Kirtland AFB, NM 87117-6008			<b>10. SPONSORING / MONITORING AGENCY REPORT NUMBER</b> WL-TR-90-27	
<b>11. SUPPLEMENTARY NOTES</b>				
<b>12a. DISTRIBUTION / AVAILABILITY STATEMENT</b> Approved for public release; distribution unlimited.			<b>12b. DISTRIBUTION CODE</b>	
<b>13. ABSTRACT (Maximum 200 words)</b> Aircraft maintenance depots and main operating bases need to be able to perform quick checks of the EMP hardness of their systems without removing them from service for any length of time. Preliminary tests have shown that the onboard HF antennas of the EMP Test-Bed Aircraft (EMPTAC) may be capable of providing the HF excitation required to effectively monitor the EMP hardness of aircraft systems. The surface current and charge distributions on the EMPTAC which result from swept frequency excitation of the HF radio antennas are computed over a range of 0.5 to 100 MHz using various antenna drive configurations. The computational analysis is performed by using two separate frequency-dependent techniques: the method-of-moments technique and the physical optics approximation. These calculations are then compared with the excitation provided from an overhead plane wave and with measured data from EMPTAC tests.				
<b>14. SUBJECT TERMS</b> EMP Hardness Surveillance HF Antennas			<b>15. NUMBER OF PAGES</b> 142	
			<b>16. PRICE CODE</b>	
<b>17. SECURITY CLASSIFICATION OF REPORT</b> UNCLASSIFIED	<b>18. SECURITY CLASSIFICATION OF THIS PAGE</b> UNCLASSIFIED	<b>19. SECURITY CLASSIFICATION OF ABSTRACT</b> UNCLASSIFIED	<b>20. LIMITATION OF ABSTRACT</b>	

## CONTENTS

<u>Section</u>	<u>Page</u>
1.0 INTRODUCTION	1
2.0 A METHOD-OF-MOMENTS SOLUTION FOR THE EMPTAC SURFACE CURRENT AND CHARGE	3
2.1 THE BODY OF REVOLUTION MODEL	3
2.2 THE METHOD-OF-MOMENTS SOLUTION TECHNIQUE	7
2.3 EXCITATION OF THE EMPTAC BY AN INCIDENT PLANE WAVE	8
2.4 EXCITATION OF THE EMPTAC VIA ONBOARD HF ANTENNAS	11
2.5 EMPTAC TEST POINT LOCATIONS	13
3.0 EMPTAC RESPONSE USING THE METHOD-OF-MOMENTS SOLUTION TECHNIQUE	18
3.1 RESPONSE OF THE EMPTAC TO PLANE WAVE EXCITATION	18
3.1.1 Incident Electric Field Parallel to the EMPTAC Fuselage	19
3.1.2 Incident Electric Field Perpendicular to the EMPTAC Fuselage	19
3.2 RESPONSE OF THE EMPTAC TO VARIOUS DRIVE CONFIGURATIONS OF THE ONBOARD HF ANTENNAS	19
3.2.1 Response of the EMPTAC to Excitation of the Fin-Cap Antenna (0.5 to 20 MHz)	35
3.2.2 Response of the EMPTAC to Excitation of the Nose and Fin-Cap Antenna (0.5 to 20 MHz)	35
3.2.3 Response of the EMPTAC to Excitation of the Port Wing Antenna (0.5 to 20 MHz)	35
3.2.4 Response of the EMPTAC to Excitation of the Port and Starboard Wing Antennas (0.5 to 20 MHz)	55
4.0 EMPTAC RESPONSE USING THE PHYSICAL OPTICS APPROXIMATION	71
4.1 RESPONSE OF THE EMPTAC TO PLANE WAVE EXCITATION	71
4.2 RESPONSE OF THE EMPTAC TO VARIOUS DRIVE CONFIGURATIONS OF THE ONBOARD HF ANTENNAS	74
4.2.1 Response of the EMPTAC to Excitation of the Fin-Cap Antenna (20 to 100 MHz)	74
4.2.2 Response of the EMPTAC to Excitation of the Nose and Fin-Cap Antennas (20 to 100 MHz)	74
4.2.3 Response of the EMPTAC to Excitation of the Port Wing Antenna (20 to 100 MHz)	85
4.2.4 Response of the EMPTAC to Excitation of the Port and Starboard Wing Antennas (20 to 100 MHz)	85

CONTENTS (CONCLUDED)

<u>Section</u>		<u>Page</u>
5.0	EMPTAC RESPONSE DATA FROM THE HPD PULSER	102
6.0	COMPARISON OF THE EMPTAC NATURAL MODES EXCITED VIA PLANE WAVE AND HF ANTENNA EXCITATION RESULTS AND CONCLUSIONS	114
7.0	RESULTS AND CONCLUSIONS	125
	REFERENCES	128

Account For

UTIS - CARAI

HW - TAB

Unprocessed

Distribution

By

Distribution

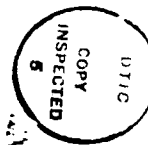
Availability Codes

Dist

Approved by

Special

A-1



## FIGURES

<u>Figure</u>		<u>Page</u>
1.	The EMPTAC body of revolution model.	4
2.	Sweep angles of EMPTAC wings.	5
3.	Body of revolution of radius (r) located a distance (h) above a ground plane.	10
4.	The EMPTAC HF antenna feed point locations.	14
5.	The EMPTAC test point locations (see Tables 2 and 3 for specific locations).	15
6.	The EMPTAC normalized current density on the top of the front fuselage (10.29 m from the nose) for topside plane wave incidence with E    to the fuselage.	20
7.	The EMPTAC normalized current density on the bottom of the front fuselage (10.29 m from the nose) for topside plane wave incidence with E    to the fuselage.	21
8.	The EMPTAC normalized current density on the top of the mid fuselage (18.69 m from the wing-fuselage junction) for topside plane wave incidence with E    to the fuselage.	22
9.	The EMPTAC normalized current density on the bottom of the mid fuselage (18.69 m from the wing-fuselage junction) for topside plane wave incidence with E    to the fuselage.	23
10.	The EMPTAC normalized current density on the top of the port wing (3.9 m from the wing-fuselage junction) for topside plane wave incidence with E    to the fuselage.	24
11.	The EMPTAC normalized current density on the top of the port wing (11.7 m from the wing-fuselage junction) for topside plane wave incidence with E    to the fuselage.	25
12.	The EMPTAC normalized charge density on the tip of the nose for topside plane wave incidence with E    to the fuselage.	26
13.	The EMPTAC normalized charge density on the tip of the vertical stabilizer for topside plane wave incidence with E    to the fuselage.	27
14.	The EMPTAC normalized charge density on the tip of the port wing for topside plane wave incidence with E    to the fuselage.	28

## FIGURES (CONTINUED)

<u>Figure</u>		<u>Page</u>
15.	The EMPTAC normalized current density on the top of the port wing (11.7 m from the wing-fuselage junction) for topside plane wave incidence with $E \perp$ to the fuselage.	29
16.	The EMPTAC normalized current density on the top of the port wing (3.9 m from the wing-fuselage junction) for topside plane wave incidence with $E \perp$ to the fuselage.	30
17.	The EMPTAC normalized charge density on the tip of the port wing for topside plane wave incidence with $E \perp$ to the fuselage.	31
18.	Radiation resistance of the HF antenna model between 500 kHz and 20 MHz.	33
19.	Magnitude of the total incident fields at points on the EMPTAC for fin-cap antenna drive ( $P_{\text{rad}} = 10 \text{ W}$ ).	34
20.	The EMPTAC normalized current density on the top of the front fuselage (10.29 m from the nose) for fin-cap antenna excitation.	36
21.	The EMPTAC normalized current density on the bottom of the front fuselage (10.29 m from the nose) for fin-cap antenna excitation.	37
22.	The EMPTAC normalized current density on the top of the mid-fuselage (18.69 m from the wing-fuselage junction) for fin-cap antenna excitations.	38
23.	The EMPTAC normalized current density on the bottom of the mid-fuselage (18.69 m from the wing-fuselage junction) for fin-cap antenna excitation.	39
24.	The EMPTAC normalized current density on the top of the port wing (3.9 m from the wing-fuselage junction) for fin-cap antenna excitation.	40
25.	The EMPTAC normalized current density on the top of the port wing (11.7 m from the wing-fuselage junction) for fin-cap antenna excitation.	41
26.	The EMPTAC normalized charge density on the tip of the nose for fin-cap antenna excitation.	42
27.	The EMPTAC normalized charge density on the tip of the port wing for fin-cap antenna excitation.	43

## FIGURES (CONTINUED)

<u>Figure</u>		<u>Page</u>
28.	The EMPTAC normalized current density on the top of the front fuselage (10.29 m from the nose) for nose and fin-cap antenna excitation.	44
29.	The EMPTAC normalized current density on the bottom of the front fuselage (10.29 m from the nose) for nose and fin-cap antenna excitation.	45
30.	The EMPTAC normalized current density on the top of the mid fuselage (18.69 m from the wing-fuselage junction) for nose and fin-cap antenna excitation.	46
31.	The EMPTAC normalized current density on the bottom of the mid fuselage (18.69 m from the wing-fuselage junction) for nose and fin-cap antenna excitation.	47
32.	The EMPTAC normalized current density on the top of the port wing (3.9 m from the wing-fuselage junction) for nose and fin-cap antenna excitation.	48
33.	The EMPTAC normalized current density on the top of the port wing (11.7 m from the wing-fuselage junction) for nose and fin-cap antenna excitation.	49
34.	The EMPTAC normalized charge density on the tip of the port wing for nose and fin-cap antenna excitation.	50
35.	The EMPTAC normalized current density on the top of the front fuselage (10.29 m from the nose) for port wing antenna excitation.	51
36.	The EMPTAC normalized current density on the bottom of the front fuselage (10.29 m from the nose) for port wing antenna excitation.	52
37.	The EMPTAC normalized current density on the top of the mid fuselage (18.69 m from the wing-fuselage junction) for port wing antenna excitation.	53
38.	The EMPTAC normalized current density on the bottom of the mid fuselage (18.69 m from the wing-fuselage junction) for port wing antenna excitation.	54
39.	The EMPTAC normalized current density on the top of the port wing (3.9 m from the wing-fuselage junction) for port wing antenna excitation.	56

## FIGURES (CONTINUED)

<u>Figure</u>		<u>Page</u>
40.	The EMPTAC normalized current density on the top of the port wing (11.7 m from the wing-fuselage junction) for port wing antenna excitation.	57
41.	The EMPTAC normalized current density on the top of the starboard wing (3.9 m from the wing-fuselage junction) for port wing antenna excitation.	58
42.	The EMPTAC normalized current density on the top of the starboard wing (11.7 m from the wing-fuselage junction) for port wing antenna excitation.	59
43.	The EMPTAC normalized charge density on the tip of the nose for port wing antenna excitation.	60
44.	The EMPTAC normalized charge density on the tip of the vertical stabilizer for port wing antenna excitation.	61
45.	The EMPTAC normalized charge density on the tip of the starboard wing for port wing antenna excitation.	62
46.	The EMPTAC normalized current density on the top of the front fuselage (10.29 m from the nose) for port and starboard wing antenna excitation.	63
47.	The EMPTAC normalized current density on the bottom of the front fuselage (10.29 m from the nose) for starboard and port wing antenna excitation.	64
48.	The EMPTAC normalized current density on the top of the mid fuselage (18.69 m from the wing-fuselage junction) for port and starboard wing antenna excitation.	65
49.	The EMPTAC normalized current density on the bottom of the mid fuselage (18.69 m from the wing-fuselage junction) for port and starboard wing antenna excitation.	66
50.	The EMPTAC normalized current density on the top of the port wing (3.9 m from the wing-fuselage junction) for port and starboard wing antenna excitation.	67
51.	The EMPTAC normalized current density on the top of the port wing (11.7 m from the wing-fuselage junction) for port and starboard wing antenna excitation.	68
52.	The EMPTAC normalized charge density on the tip of the nose for port and starboard wing antenna excitation.	69
53.	The EMPTAC normalized charge density on the tip of the vertical stabilizer for port and starboard wing antenna excitation.	70

## FIGURES (CONTINUED)

<u>Figure</u>		<u>Page</u>
54.	The EMPTAC normalized current density on the top of the front fuselage (10.29 m from the nose) for fin-cap antenna excitation (physical optics approximation).	75
55.	The EMPTAC normalized current density on the bottom of the front fuselage (10.29 m from the nose) for fin-cap antenna excitation (physical optics approximation).	76
56.	The EMPTAC normalized current density on the top of the mid fuselage (18.69 m from the wing-fuselage junction) for fin-cap antenna excitation (physical optics approximation).	77
57.	The EMPTAC normalized current density on the bottom of the mid fuselage (18.69 m from the wing-fuselage junction) for fin-cap antenna excitation (physical optics approximation).	78
58.	The EMPTAC normalized current density on the top of the port wing (3.9 m from the wing-fuselage junction) for fin-cap antenna excitation (physical optics approximation).	79
59.	The EMPTAC normalized current density on the top of the port wing (11.7 m from the wing-fuselage junction) for fin-cap antenna excitation (physical optics approximation).	80
60.	The EMPTAC normalized current density on the top of the front fuselage (10.29 m from the nose) for nose and fin-cap antenna excitation (physical optics approximation).	81
61.	The EMPTAC normalized current density on the bottom of the fuselage (10.29 m from the nose) and fin-cap antenna excitation (physical optics approximation).	82
62.	The EMPTAC normalized current density on the top of the mid fuselage (18.69 m from the wing-fuselage junction) for nose and fin-cap antenna excitation (physical optics approximation).	83
63.	The EMPTAC normalized current density on the bottom of the mid fuselage junction) for nose and fin-cap antenna excitation (physical optics approximation).	84
64.	The EMPTAC normalized current density on the top of the port wing (3.9 m from the wing-fuselage junction) for nose and fin-cap antenna excitation (physical optics approximation).	86
65.	The EMPTAC normalized current density on the top of the port wing (11.7 m from the wing-fuselage junction) for nose and fin-cap antenna excitation (physical optics approximation).	87

## FIGURES (CONTINUED)

<u>Figure</u>		<u>Page</u>
66.	The EMPTAC normalized current density on the top of the front fuselage (10.29 m from the nose) for port wing antenna excitation (physical optics approximation).	88
67.	The EMPTAC normalized current density on the bottom of the front fuselage (10.29 m from the nose) for port wing antenna excitation (physical optics approximation).	89
68.	The EMPTAC normalized current density on the top of the mid fuselage (18.69 m from the wing-fuselage junction) for port wing antenna excitation (physical optics approximation).	90
69.	The EMPTAC normalized current density on the bottom of the mid fuselage (18.69 m from the wing-fuselage junction) for port wing antenna excitation (physical optics approximation).	91
70.	The EMPTAC normalized current density on the top of the port wing (3.9 m from the wing-fuselage junction) for port wing antenna excitation (physical optics approximation).	92
71.	The EMPTAC normalized current density on the top of the port wing (11.7 m from the wing-fuselage junction) for port wing antenna excitation (physical optics approximation).	93
72.	The EMPTAC normalized current density on the top of the starboard wing (3.9 m from the wing-fuselage junction) for port wing antenna excitation (physical optics approximation).	94
73.	The EMPTAC normalized current density on the top of the starboard wing (11.7 m from the wing-fuselage junction) for port wing antenna excitation (physical optics approximation).	95
74.	The EMPTAC normalized current density on the top of the front fuselage (10.29 m from the nose) for port and starboard wing antenna excitation (physical optics approximation).	96
75.	The EMPTAC normalized current density on the bottom of the front fuselage (10.29 m from the nose) for starboard and port wing antenna excitation (physical optics approximation).	97
76.	The EMPTAC normalized current density on the top of the mid fuselage (18.69 m from the wing-fuselage junction) for port and starboard wing antenna excitation (physical optics approximation).	98

## FIGURES (CONTINUED)

<u>Figures</u>	<u>Page</u>
77. The EMPTAC normalized current density on the bottom of the mid fuselage (18.69 m from the wing-fuselage junction) for port and starboard wing antenna excitation (physical optics approximation).	99
78. The EMPTAC normalized current density on the top of the port wing (3.9 m from the wing-fuselage junction) for port and starboard wing antenna excitation (physical optics approximation).	100
79. The EMPTAC normalized current density on the top of the port wing (11.7 m from the wing-fuselage junction) for port and starboard wing antenna excitation (physical optics approximation).	101
80. The EMPTAC surface current density on the top of the front fuselage (test point #1) (experimental data obtained from the HPD pulser, E    fuselage).	103
81. The EMPTAC surface current density on the bottom of the front fuselage (test point #2) (experimental data obtained from the HPD pulser, E    fuselage).	104
82. The EMPTAC surface current density on the top of the mid fuselage (test point #3) (experimental data obtained from the HPD pulser, E    fuselage).	105
83. The EMPTAC surface current density on the bottom of the mid fuselage (test point #4) (experimental data obtained from the HPD pulser, E    fuselage).	106
84. The EMPTAC surface current density on the top of the port wing (test point #5) (experimental data obtained from the HPD pulser, E $\perp$ to fuselage).	107
85. The EMPTAC surface current density on the top of the starboard wing (test point #7) (experimental data obtained from the HPD pulser, E $\perp$ to fuselage).	108
86. The EMPTAC surface current density on the top of the starboard wing (test point #8) (experimental data obtained from the HPD pulser, E $\perp$ to fuselage).	109
87. The EMPTAC surface charge density on the nose of the aircraft (test point #9) (experimental data obtained from the HPD pulser, E    to fuselage).	110
88. The EMPTAC surface charge density on the vertical stabilizer (test point #10) (experimental data obtained from the HPD pulser, E    to fuselage).	111

## FIGURES (CONCLUDED)

<u>Figure</u>		<u>Page</u>
89.	The EMPTAC surface charge density on the tip of the port wing (test point #11) (experimental data obtained from the HPD pulser, $E \perp$ to fuselage).	112
90.	The EMPTAC surface charge density on the tip of the starboard wing (test point #12) (experimental data obtained from the HPD pulser, $E \perp$ to fuselage).	113
91.	The EMPTAC normalized current density along the top of the forward fuselage at the first symmetric resonance (2.54 MHz) for symmetric plane wave and HF antenna excitations.	117
92.	The EMPTAC normalized current density along the top of the forward fuselage at the second symmetric resonance (4.64 MHz) for symmetric plane wave and HF antenna excitations.	118
93.	The EMPTAC normalized current density along the top of the mid fuselage at the first symmetric resonance (2.54 MHz) for symmetric plane wave and HF antenna excitations.	119
94.	The EMPTAC normalized current density along the top of the mid fuselage at the second symmetric resonance (4.64 MHz) for symmetric plane wave and HF antenna excitations.	120
95.	The EMPTAC normalized current density along the top of the port wing at the first symmetric resonance (2.54 MHz) for symmetric plane wave and HF antenna excitations.	121
96.	The EMPTAC normalized current density along the top of the port wing at the second symmetric resonance (4.64 MHz) for symmetric plane wave and HF antenna excitations.	122
97.	The EMPTAC normalized current density along the top of the wings at the first antisymmetric resonance (3.62 MHz) for antisymmetric plane wave and HF antenna excitations.	123
98.	The EMPTAC normalized current density along the top of the wings at the second antisymmetric resonance (9.85 MHz) for antisymmetric plane wave and HF antenna excitations.	124

## 1.0 INTRODUCTION

The Electromagnetic Pulse (EMP) hardness of an aircraft system may be monitored using one of several global systems currently available such as the Hardness Surveillance Illuminator (HSI) or the Horizontally Polarized Dipole (HPD). The primary drawback associated with these monitoring systems is that the aircraft must be taken out of service for approximately 2 weeks. Thus, the hardness monitoring systems currently available are of practical use only for spot checking or requalifying an aircraft after a major modification. A method of performing periodic quick checks of EMP hardness for every aircraft in a fleet is needed. This technique would be especially useful following a major maintenance action.

One technique which has been developed for quick checks of system hardness is Single Point Excitation for Hardness Surveillance (SPEHS) (Refs. 1 and 2). However, the SPEHS technique works effectively only when the aircraft is excited at its resonant frequency. Therefore, the frequency range of operation for the SPEHS technique lies within the 1 to 3 MHz range. Excitation of an aircraft in this frequency range makes the SPEHS technique inadequate with regard to diagnosing faults in radio frequency (RF) gaskets, RF filters and cable shields. Failures of these elements may be identified by examining changes in their transfer reactance which requires a range of data including frequencies much higher than the resonant frequency of the aircraft under test.

Preliminary tests have shown that the onboard high frequency (HF) antennas of the EMP Test-bed Aircraft (EMPTAC) (Boeing 720B) may be capable of providing the HF excitation required to effectively monitor the EMP hardness of aircraft systems. The EMPTAC HF antennas are located at the end of the starboard wing and at the top of the vertical stabilizer. The EMPTAC HF antennas are designed for operation over the 3 to 30 MHz range. Yet, tests have shown that the HF antennas of the EMPTAC are capable of operations up to 100 MHz. The problem is determining the surface charge and current distributions which result when the EMPTAC aircraft is illuminated by various HF antenna configurations over the frequency range of interest.

The surface current and charge distributions on the EMPTAC which result for swept frequency excitation of the HF radio antennas are computed over a range of 0.5 to 100 MHz. The external responses of the EMPTAC are computed for both the inflight and ground alert modes. In the ground alert mode, the ground plane beneath the aircraft is assumed to be perfectly conducting. The computational analysis is performed using two separate techniques which are dependent on the frequency of operation. A method-of-moments technique (Ref. 3) is applied for frequencies of approximately 20 MHz and less for which the aircraft is modelled by intersecting conductive bodies of revolution. For frequencies above 20 MHz, the physical optics approximation is used to determine the limitations of exciting the aircraft via the HF antenna. The natural modes of the aircraft are obtained numerically as shown by Taylor and Crow (Ref. 4). The excitation of these natural modes using various configurations of the HF antennas are investigated.

The surface current and charge distributions induced at various points on the EMPTAC are computed for four different HF antenna excitation configurations:

- fin-cap antenna only
- fin-cap and nose antenna
- one wing-tip probe
- two wing-tip probes

The symmetric and antisymmetric modes of the aircraft are determined from the resulting data. The current and charge distributions which result from the aforementioned excitation configurations are compared with the distributions which result from excitation of the aircraft on the ground by an overhead plane wave. These results are also compared with measured data from EMPTAC tests.

## 2.0 A METHOD-OF-MOMENTS SOLUTION FOR THE EMPTAC SURFACE CURRENT AND CHARGE

The current and charge densities which are excited on the surface of an aircraft by an incident of electromagnetic field may be computed numerically using the method of moments (Ref. 3). The method of moments is an integral equation solution technique which may be applied to complex geometries. An accurate method-of-moments solution for the EMPTAC surface current and charge requires an accurate geometric model for the outer conducting surface of the aircraft. An accurate yet relatively simple description of the outer skin of the EMPTAC is obtained using intersecting bodies of revolution (right-circular cylinders and ellipsoids) Ref. 5).

### 2.1 THE BODY OF REVOLUTION MODEL

The body of revolution model for the EMPTAC (Boeing 720B) is shown in Figure 1. The skin of the aircraft is modelled using nine distinct bodies of revolution which are designated as  $(S_1, S_2, \dots, S_9)$ . Each body of revolution is subdivided into current zones of equal length with  $N_n$  denoting the total number of current zones on the  $n$ th body of revolution ( $S_n$ ). The following portions of the EMPTAC are modelled by simple ellipsoids: wings, horizontal stabilizers, front fuselage, aft fuselage, and upper portion of the vertical stabilizer. The lower portion of the vertical stabilizer is modelled by a cylinder of constant radius while the mid fuselage consists of a constant radius portion and a tapered radius portion. A complete description of each body of revolution is given in Table 1. The sweep angle of the wings, horizontal stabilizers and vertical stabilizer are shown in Figure 2.

The variation in radius along each of the ellipsoids listed in Table 1 is defined according to the maximum radius ( $R_n$ ) and total length ( $L_n$ ). The radius of the  $n$ th body of revolution as a function of length is given by

$$r_n(s) = R_n \left[ 1 - \left( \frac{s}{L_n} \right)^2 \right]^{1/2} \quad n = 1, 2, 3, 4, 6, 9 \quad (1)$$

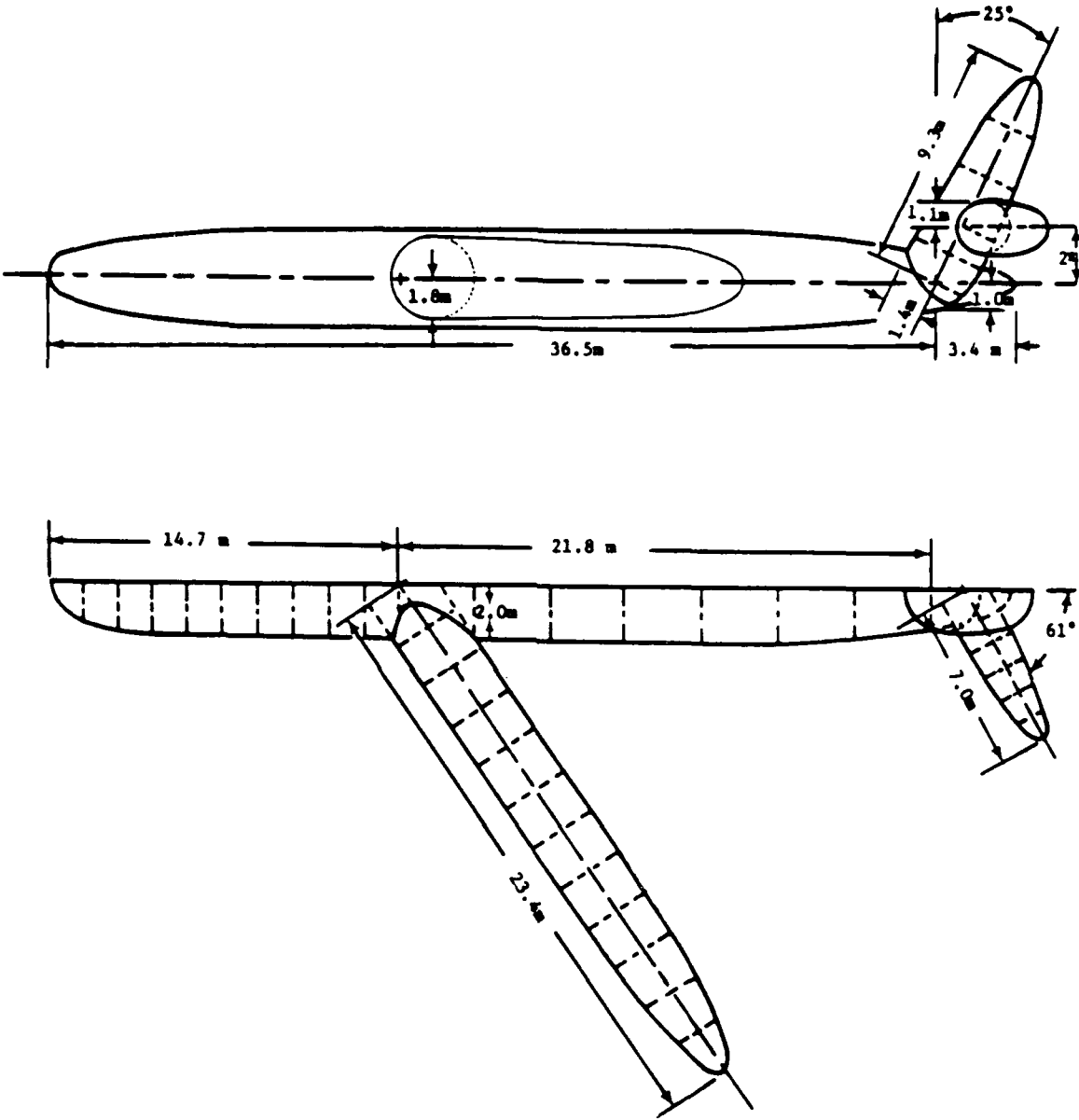
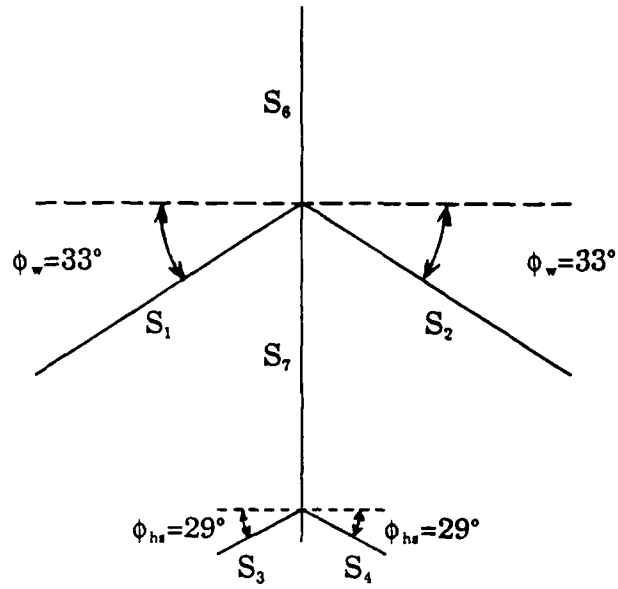
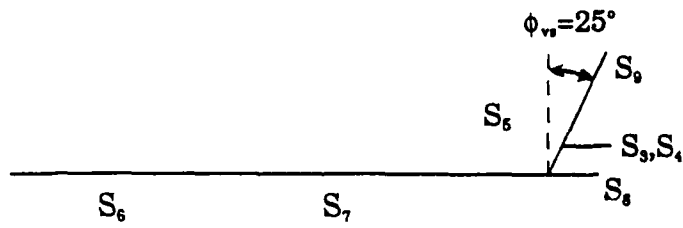


Figure 1. The EMPTAC Body of Revolution Model.



(a) Vertical stabilizer.



(b) Wings and horizontal stabilizers.

Figure 2. Sweep angles of EMPTAC wings.

Table 1. Description of the individual elements for the EMPTAC body of revolution model.

Element	Physical Description	Body of Revolution Type	Number of Current Zones	Total Length (m)	Maximum Radius (m)
S <sub>1</sub>	Port Wing	Ellipsoid	N <sub>1</sub> =12	L <sub>1</sub> =23.4	R <sub>1</sub> =1.8
S <sub>2</sub>	Starboard Wing	Ellipsoid	N <sub>2</sub> =12	L <sub>2</sub> =23.4	R <sub>2</sub> =1.8
S <sub>3</sub>	Port Horizontal Stabilizer	Ellipsoid	N <sub>3</sub> =6	L <sub>3</sub> =7.0	R <sub>3</sub> =1.1
S <sub>4</sub>	Starboard Horizontal Stabilizer	Ellipsoid	N <sub>4</sub> =6	L <sub>4</sub> =7.0	R <sub>4</sub> =1.1
S <sub>5</sub>	Lower Portion of the Vertical Stabilizer	Right Circular Cylinder	N <sub>5</sub> =2	L <sub>5</sub> =2.21	R <sub>5</sub> =1.4
S <sub>6</sub>	Forward Fuselage	Ellipsoid	N <sub>6</sub> =10	L <sub>6</sub> =14.7	R <sub>6</sub> =2.0
S <sub>7</sub>	Mid Fuselage	(a) Right Circular Cylinder	N <sub>7a</sub> =4	L <sub>7</sub> =21.7	R <sub>7a</sub> =2.0
		(b) Truncated Ellipsoid	N <sub>7b</sub> =3		R <sub>7b</sub> =2.0
S <sub>8</sub>	Aft Fuselage	Ellipsoid	N <sub>8</sub> =4	L <sub>8</sub> =3.4	R <sub>8</sub> =1.36
S <sub>9</sub>	Upper Portion of the Vertical Stabilizer	Ellipsoid	N <sub>9</sub> =3	L <sub>9</sub> =7.09	R <sub>9</sub> =1.4

where  $s$  defines the length along the axis of the ellipsoid ( $s = 0$  defines the point of maximum radius). The lower portion of the vertical stabilizer ( $S_5$ ) is a constant radius cylinder with  $r_5(s) = R_5$ . The radius along the tapered portion of the mid fuselage ( $S_7$ ) is given by

$$r_7(s) = R_7 \left\{ 1 - \left[ \frac{s - 4L_7/7}{3L_7 + L_8} \right]^2 \right\}^{1/2} \quad 4L_7/7 \leq s \leq L_7 \quad (2)$$

The aft fuselage ( $S_8$ ) is defined according to Equation 1 given the radius of the mid fuselage at the tapered end [ $r_7(L_7)$ ].

For ground alert mode computations, the EMPTAC body of revolution model is located above a perfectly conducting ground plane of infinite extent. The vertical distance from the center line of the EMPTAC fuselage to the ground plane is assumed to be 3.2 m.

## 2.2 THE METHOD-OF-MOMENTS SOLUTION TECHNIQUE

The external responses of the EMPTAC to both plane wave excitation and HF antenna excitation are determined using the method of moments. The particular method-of-moments solution technique utilized is an extension of Hallen's integral equation for thin wires to bodies of revolution (Ref. 5). The extended boundary condition defined by Taylor and Wilton (Ref. 6) is implemented using the intersecting bodies of revolution model for the EMPTAC. The extended boundary condition requires that the total electric field vanish at all points within each conducting body of revolution.

The individual bodies of revolution are subdivided into electrically short current zones. The circumferential component of current over each zone is assumed to be negligible in comparison to the axial current component. Therefore, the method-of-moments solution technique is inherently limited to low frequencies (<20 MHz). The total axial current along the  $n$ th zone of the  $j$ th body of revolution is defined by

$$I_j(s_j) = \frac{I_j(s_{j,n+1}) \sin[k(s_j - s_{j,n})] + I_j(s_{j,n}) \sin[k(s_{j,n+1} - s_j)]}{\sin[k(s_{j,n+1} - s_{j,n})]} \quad (3)$$

where  $I_j(s_{j,n})$  and  $I_j(s_{j,n+1})$  define the end currents and  $s_j$  defines the distance along the  $j$ th body of revolution. The King and Wu (Ref. 7) boundary conditions are enforced at all junctions along with Kirchoff's Current Law. A system of complex linear algebraic equations is generated such that the unknown current coefficients may be determined through a simple matrix inversion.

### 2.3 EXCITATION OF THE EMPTAC BY AN INCIDENT PLANE WAVE

The unit step response of the EMPTAC to a uniform plane wave incident from above is computed for both the inflight and ground alert modes assuming two distinct polarizations of the incident field: (a) the incident electric field parallel to the fuselage and (b) the incident electric field perpendicular to the fuselage. The incident wave is assumed to arrive at the center line of the fuselage at time  $t = 0$ . The magnitude of the incident electric field is assumed to be 1 V/m.

The total axial current density induced on an isolated, electrically thin body of revolution may be used to approximate the surface current density. At low frequency where the circumference of the structure cross section is more than a wavelength, the contribution of the circumferential current to the surface current density can be neglected. The contribution to the surface current density from the total axial current is

$$J_s(s) \approx \frac{I(s)}{2\pi r(s)} \quad (4)$$

where  $I(s)$  is the total axial current and  $r(s)$  is the body of revolution radius as a function of length. A more accurate representation of the surface

current includes the magnetostatic contribution (Ref. 8 and 9).

Accordingly, the surface current density may be written as

$$J_s(s, \phi) \approx \frac{I(s)}{2\pi r(s)} + 2\hat{\phi} \cdot \bar{H}^{inc} \quad (5)$$

where  $\hat{\phi}$  represents a unit vector defined in the right-hand sense with respect to the direction of positive axial current. Equation 5 represents the formulation used in this research to obtain the current density at specified points on the aircraft in the inflight mode. The corresponding surface charge density ( $\rho_s$ ) on the body of revolution is defined in terms of the surface current density using the equation of continuity given by

$$\rho_s = \frac{j}{\omega} \text{div } \bar{J}_s \quad (6)$$

where  $\omega$  represents the radian frequency of the incident field.

In the ground alert mode, the effect of both the incident and ground reflected fields must be included in the computation of the body of revolution surface current density. Also, a body of revolution located near a conducting ground plane experiences the so-called proximity effect which describes the crowding of current on the body of revolution region closest to the ground plane (Ref. 5). Thus, the surface current density on a body of revolution of radius  $r(s)$  located a distance  $h$  above a conducting ground plane as shown in Figure 3 may be written as

$$J_s(s, \phi) \approx \frac{I(s)}{2\pi r(s)} f(s, \phi) + 2\hat{\phi} \cdot (\bar{H}^{inc} + \bar{H}^{ref}) \quad (7)$$

where the function  $f(s, \phi)$  is defined by

$$f(s, \phi) = \frac{\{1 - [r(s)/h]^2\}^{1/2}}{\{1 + [r(s)/h] \sin \phi\}} \quad (8)$$

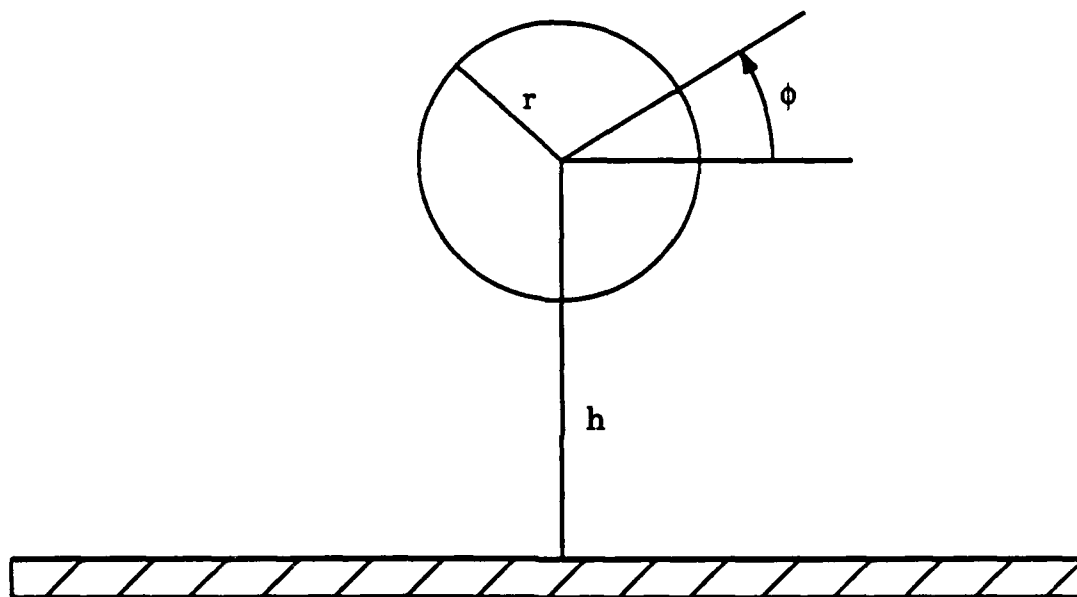


Figure 3. Body of revolution of radius ( $r$ ) located a distance ( $h$ ) above a ground plane.

Again, the surface charge density is found through the equation of continuity given in Equation 6.

#### 2.4 EXCITATION OF THE EMPTAC VIA ONBOARD HF ANTENNAS

To evaluate the effectiveness of exciting the EMPTAC HF antennas for hardness surveillance, the EMPTAC is assumed to have four antennas which are located at the tip of the nose, at the end of the port wing, at the end of the starboard wing and at the tip of the vertical stabilizer (fin-cap). The antennas are heretofore referred to as

- antenna #1, nose antenna
- antenna #2, port wing antenna
- antenna #3, starboard wing antenna
- antenna #4, fin-cap antenna

Each antenna is assumed to be 2 m in length and tunable over the frequency range of interest to match the driving amplifier (Ref. 9).

Several factors must be considered when selecting the antenna models to be used in conjunction with the body of revolution (method of moments) solution technique. Foremost, the antenna models should accurately describe the physical interaction of the antennas with the aircraft. One possible technique of modelling the HF antennas is to include the antennas as additional bodies of revolution. However, the resulting wing and fin-cap antennas would not accurately represent the physical behavior of the axial current on the wings and the vertical stabilizer. The actual EMPTAC wing and fin-cap antennas would be driven at a point near the edge of a conductor (i.e., the wing tips and the tip of the vertical stabilizer). The resulting current driven onto the skin of the aircraft would be confined predominately to the conducting edge, thus producing a small axial component of current. An antenna connected to the end point of a body of revolution (wing, vertical stabilizer) would drive the entire aircraft skin current in an axial direction producing an inaccurate physical model.

Assuming the skin currents produced by the wing and fin-cap antennas are confined to the respective conductor edges, the contributions to the axial currents produced by driving these antennas are considered negligible. Using

the previous assumption, the axial currents on the aircraft may be assumed to be dependent on the incident and scattered fields only. Thus, the four EMPTAC HF antennas are assumed to be electrically isolated from the aircraft. Even though the EMPTAC nose antenna drives current onto the aircraft fuselage in an axial direction, the electrically isolated nose antenna model is assumed to yield accurate results with the exception of points on the fuselage close to the nose antenna.

The body of revolution computational model used for the plane wave excitation (see paragraph 2.3) is modified by replacing the incident plane wave electric field components by the corresponding field components produced by the specific antenna drive configuration. Each antenna is modelled as an infinitely thin center-fed dipole of length  $2h$  with a current distribution give by

$$I_z(z) = I_z(0) \frac{\sin[k(h - |z|)]}{\sin(kh)} \quad (9)$$

where  $z$  defines the distance along the length of the antenna with the feed point located at  $z = 0$ . Assuming the current distribution in Equation 9, the complete electromagnetic field of the antenna may be expressed in closed form (Ref. 10). The resulting electromagnetic field of an infinitely thin center-fed dipole of length  $2h$  lying along the  $z$ -axis with its feed point located at the cylindrical coordinate origin is

$$E_\rho(\bar{r}) = \frac{j\omega\mu I_z(0)}{4\pi k\rho} \left[ \frac{z-h}{R_{1h}} e^{-jkR_{1h}} + \frac{z+h}{R_{2h}} e^{-jkR_{2h}} - \frac{2z}{\gamma} \cos(kh) e^{-jk\gamma} \right] \quad (10)$$

$$E_z(\vec{r}) = - \frac{j\omega\mu I_z(0)}{4\pi k} \left[ \frac{e^{-jkR_{1h}}}{R_{1h}} + \frac{e^{-jkR_{2h}}}{R_{2h}} - \frac{2}{\gamma} \cos(kh)e^{-jk\gamma} \right] \quad (11)$$

and

$$H_\phi(\vec{r}) = \frac{jI_z(0)}{4\pi} \left[ e^{-jkR_{1h}} + e^{-jkR_{2h}} - 2\cos(kh)e^{-jk\gamma} \right] \quad (12)$$

where

$$R_{1h} = [(h - z)^2 + \rho^2]^{1/2} \quad (13)$$

$$R_{2h} = [(h + z)^2 + \rho^2]^{1/2} \quad (14)$$

and

$$\gamma = [z^2 + \rho^2] \quad (15)$$

The feed point of the nose antenna is located at the end point of  $S_6$  as shown in Figure 4. The location of the wing and fin-cap antenna feed points are offset from the axes of the respective bodies of revolution in order to account for the width of the wing-tips and fin-cap. Thus, the feed points of the wing and fin-cap antennas are located 1.5 m forward of the corresponding body of revolution end point (Fig. 4).

## 2.5 EMPTAC TEST POINT LOCATIONS

The points on the aircraft where the surface current and charge are computed are shown in Figure 5. The exact locations of the respective test points are shown in Table 2 (current test points) and Table 3 (charge test points). The current test points are defined as test points #1 through #8 while the charge test points are test points #9 through #12. The current and charge densities at the test points located on the starboard wing (#7, #8 and #12) are considered only for antisymmetric excitation of the HF antennas.

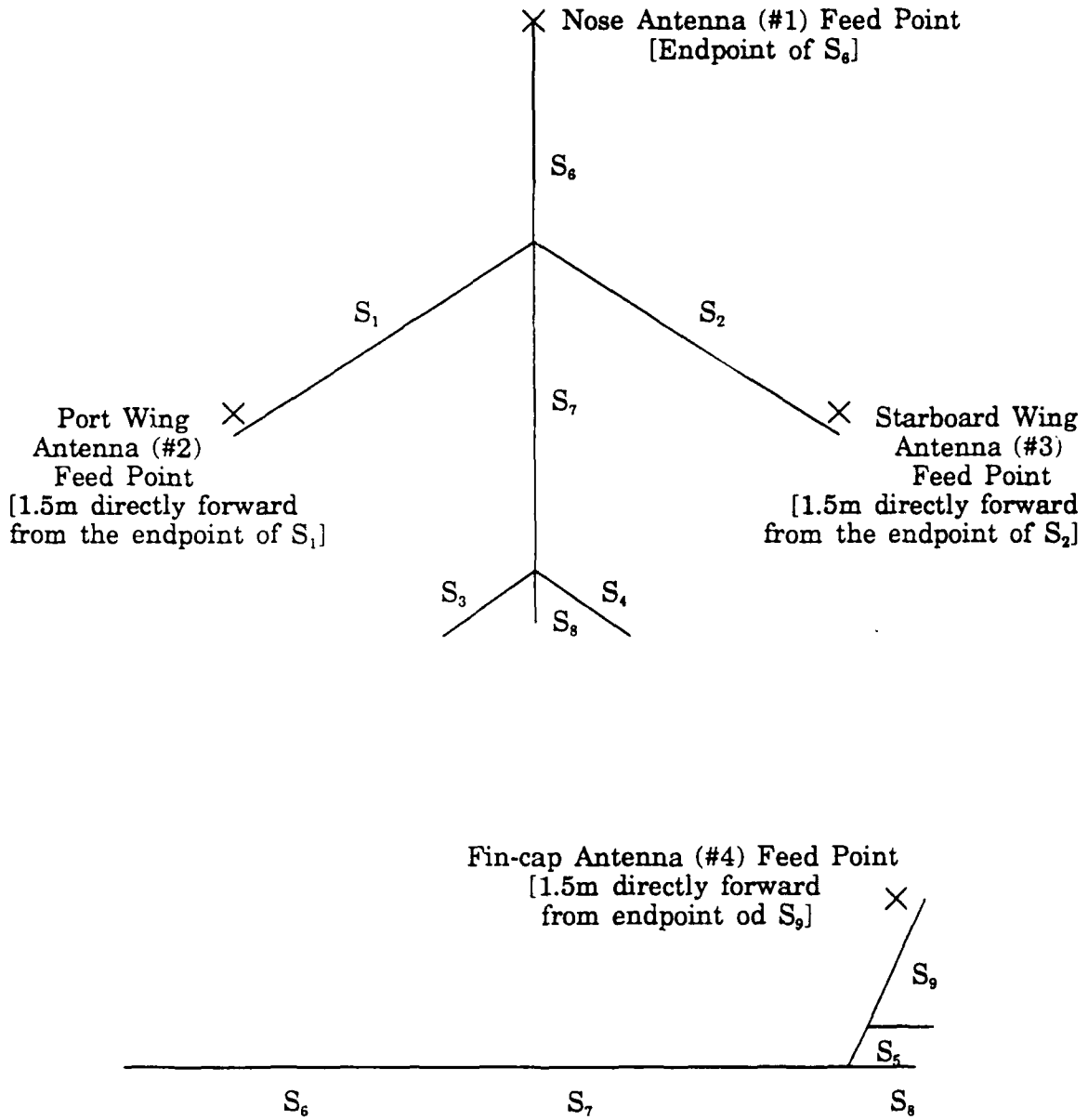


Figure 4. The EMPTAC HF antenna feed point locations.

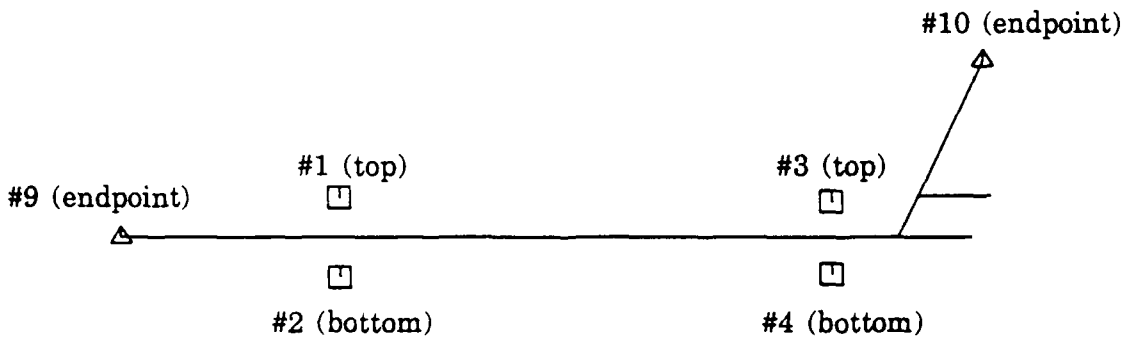
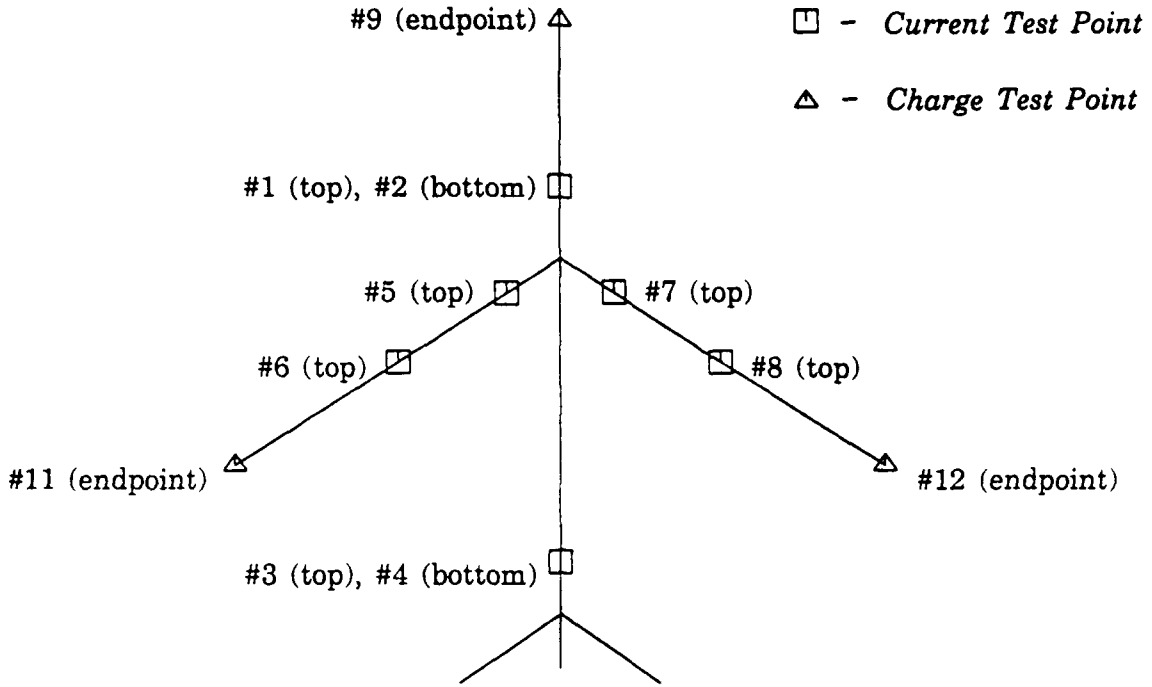


Figure 5. The EMPTAC test point locations (see Tables 2 and 3 for specific locations).

Table 2. Description of the EMPTAC current test points.

Test Point #	Element	Element Radius (m) at Test Point	Location Description
1	S <sub>6</sub>	1.91	Top side of front fuselage, 10.29 m from the nose as measured along the axis of S <sub>6</sub>
2	S <sub>6</sub>	1.91	Bottom side of front fuselage, 10.29 m from the nose as measured along the axis of S <sub>6</sub>
3	S <sub>7</sub>	1.74	Top side of mid fuselage, 18.69 m from the wing-fuselage junction as measured along the axis of S <sub>7</sub>
4	S <sub>7</sub>	1.74	Bottom side of mid fuselage, 18.69 m from the wing-fuselage junction as measured along the axis of S <sub>7</sub>
5	S <sub>1</sub>	1.77	Top side of port wing, 3.9 m from the wing-fuselage junction as measured along the axis of S <sub>1</sub>
6	S <sub>1</sub>	1.56	Top side of port wing, 11.7 m from the wing-fuselage junction as measured along the axis of S <sub>1</sub>
7	S <sub>2</sub>	1.77	Top side of starboard wing, 3.9 m from the wing-fuselage junction as measured along the axis of S <sub>2</sub>
8	S <sub>2</sub>	1.56	Top side of starboard wing, 11.7 m from the wing-fuselage junction as measured along the axis of S <sub>2</sub>

Table 3. Description of the EMPTAC charge test points.

---

Test Point #	Element	Location Description
9	S <sub>6</sub>	Tip of the nose
10	S <sub>1</sub>	Tip of the port wing
11	S <sub>2</sub>	Tip of the starboard wing
12	S <sub>9</sub>	Tip of the vertical stabilizer

---

### 3.0 EMPTAC RESPONSE USING THE METHOD-OF-MOMENTS SOLUTION TECHNIQUE

The external responses of the EMPTAC due to plane wave excitation and the excitation via onboard HF antennas are considered in this section for frequencies between 500 kHz and 20 MHz. The surface responses presented are obtained using the body of revolution model and the method-of-moments solution technique discussed in Section 2.0. The EMPTAC responses for frequencies between 20 and 100 MHz are presented in Section 4.0.

#### 3.1 RESPONSE OF THE EMPTAC TO PLANE WAVE EXCITATION

The external response of the EMPTAC to a plane wave incident from above is presented in this section for both the inflight and ground alert modes. Two distinct polarizations of the incident plane wave are considered for each mode of operation:

- the electric field parallel to the aircraft fuselage
- the electric field perpendicular to the aircraft fuselage

The EMPTAC surface current and charge densities produced by any plane wave incident may be obtained through a linear superposition of the two given polarizations.

The magnitude of the incident electric field is assumed to be 1 V/m for both polarizations ( $E_0 = 1$  V/m). The surface current density obtained for each polarization is normalized using the magnitude of the total incident magnetic field ( $H_0 = 1/\eta_0$  A/m) where  $\eta_0$  is the intrinsic impedance of free space ( $\eta_0 = 120\pi \Omega$ ). The resulting normalized value of  $J_s/H_0$  versus frequency is plotted. The surface charge density is normalized in a similar manner according to the magnitude of the total incident electric flux density ( $D_0 = 1/\epsilon_0$  C/m<sup>2</sup>) where  $\epsilon_0$  is the free space permittivity ( $\epsilon_0 = 8.854$  pF/m). The resulting normalized value is plotted for  $\rho_s/D_0$  versus frequency. The normalized surface current and charge densities are plotted over the range of 500 kHz to 20 MHz.

### 3.1.1 Incident Electric Field Parallel to the EMPTAC Fuselage

The normalized responses of the EMPTAC to excitation by a topside-incident plane wave with the electric field parallel to the aircraft fuselage are shown in Figures 6 through 14. Figures 6 and 7 represent the normalized current density on the top and bottom of the front fuselage (test points #1 and #2, respectively). Figures 8 and 9 represent the normalized current density on the top and bottom of the mid fuselage (test points #3 and #4, respectively). Figures 10 and 11 represent the normalized current density at points on the top of the port wing (test points #5 and #6), respectively. Figures 12 through 14 represent the normalized charge densities on the tip of the nose (test point #9), on the tip of the vertical stabilizer (test point #10), and on the tip of the port wing (test point #11), respectively. The starboard wing responses (test points, #7, #8 and #12) predicted by the method-of-moments solution are identical to those of the port wing.

### 3.1.2 Incident Electric Field Perpendicular to the EMPTAC Fuselage

The normalized responses of the EMPTAC to excitation by a topside-incident plane wave with the electric field perpendicular to the aircraft fuselage are shown in Figures 15 through 17. Negligible responses are obtained for all test points which are located on the fuselage and vertical stabilizer (test points #1, #2, #3, #4, #9 and #10) since the electric field is perpendicular to these segments. Figures 15 and 16 represent the normalized current density at points on the top of the port wing (test points #5 and #6, respectively). Figure 17 represents the normalized charge density on the tip of the port wing (test point #11). Again, the responses on the starboard wing (test points #7, #8 and #12) equal those on the port wing.

## 3.2 RESPONSE OF THE EMPTAC TO VARIOUS DRIVE CONFIGURATIONS OF THE ONBOARD HF ANTENNAS

The external responses of the EMPTAC to various drive configurations of the onboard HF antennas are presented for both the inflight and ground alert modes. Four distinct drive configurations are considered for each mode of operation:

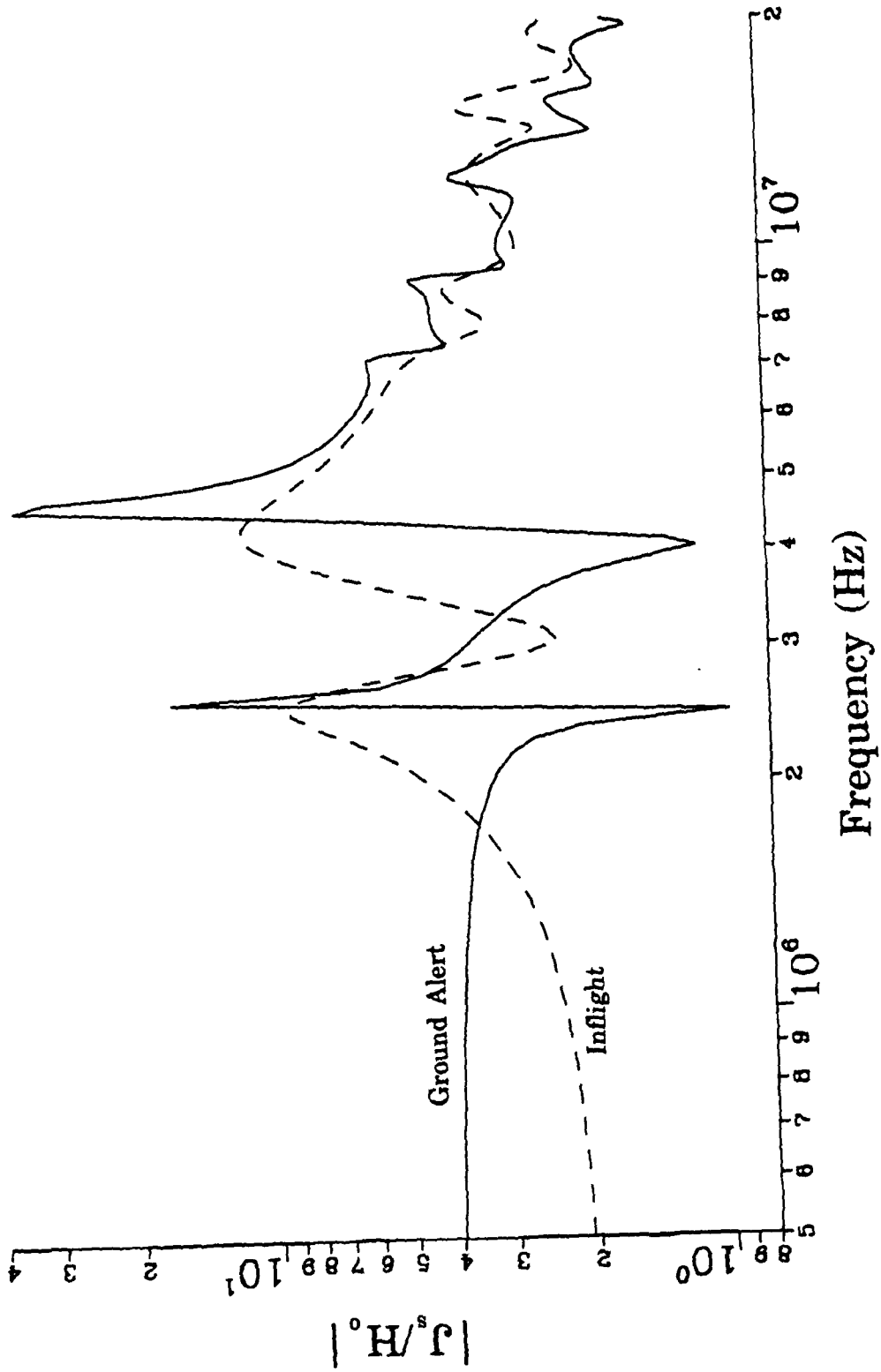


Figure 6. The EMPTAC normalized current density on the top of the front fuselage (10.29 m from the nose) for topside plane wave incidence with  $E||$  to the fuselage.

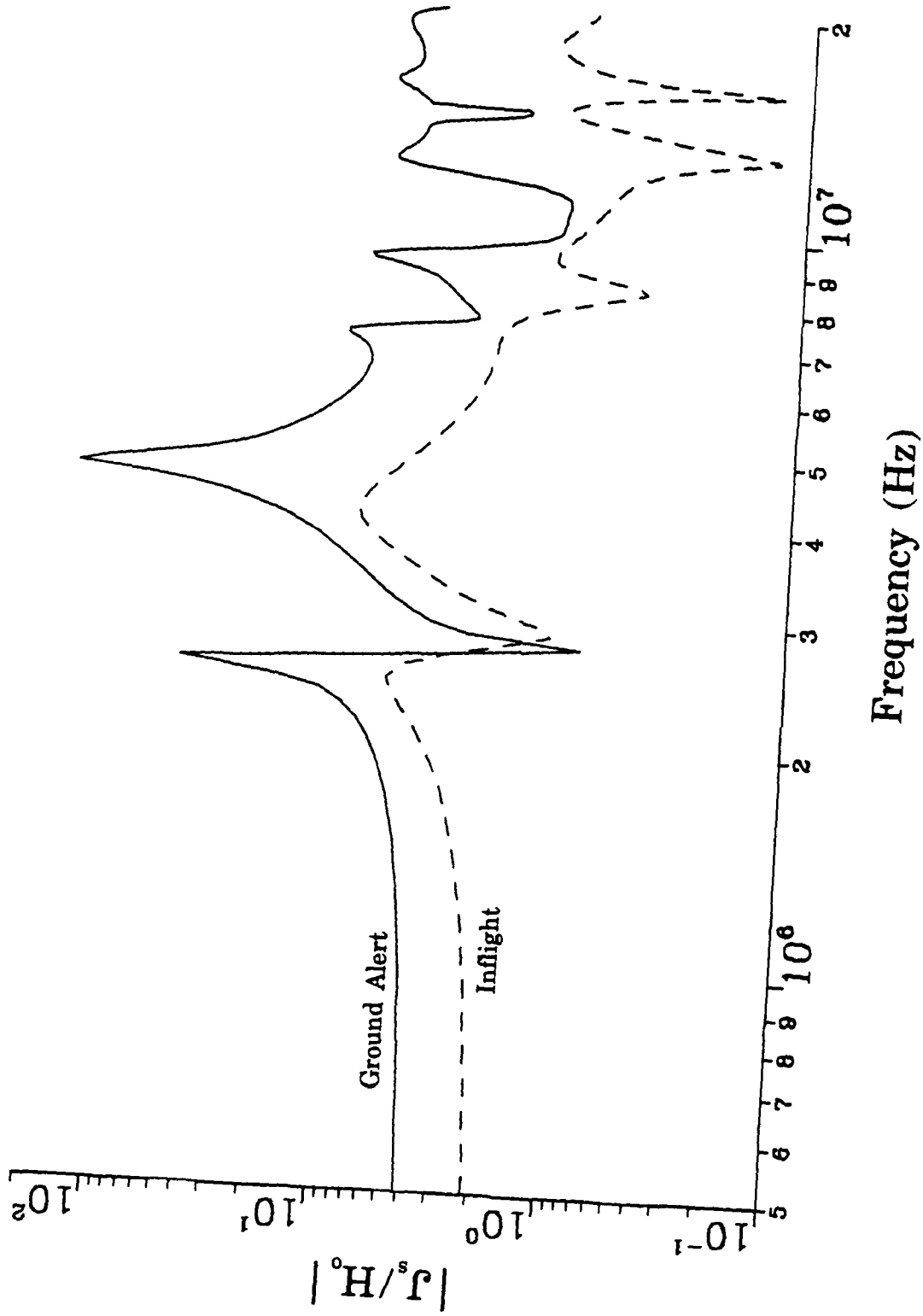


Figure 7. The EMPTAC normalized current density on the bottom of the front fuselage (10.29 m from the nose) for topside plane wave incidence with  $E \parallel$  to the fuselage.

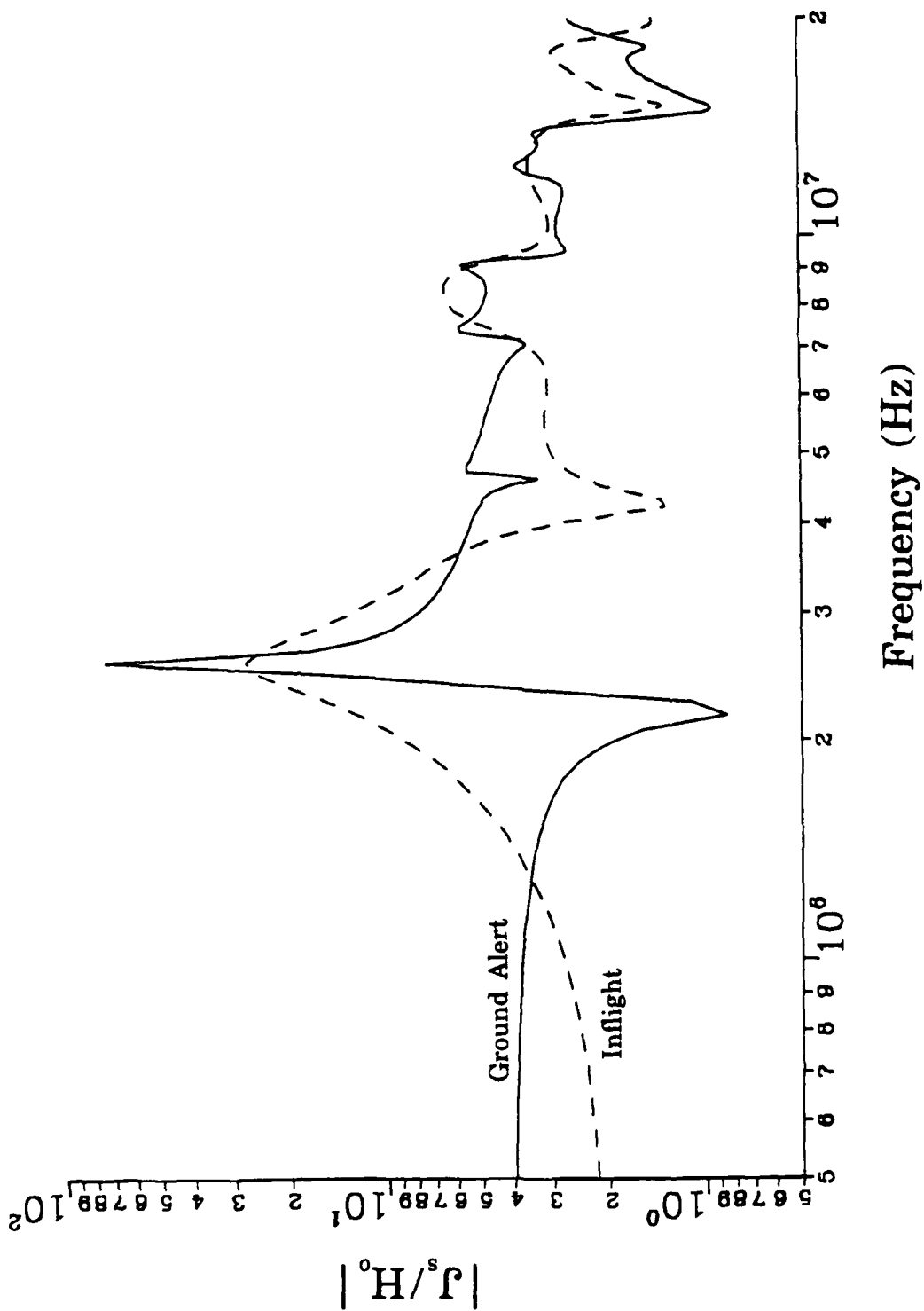


Figure 8. The EMPTAC normalized current density on the top of the mid fuselage (18.69 m from the wing-fuselage junction) for topside plane wave incidence with  $E \parallel$  to the fuselage.

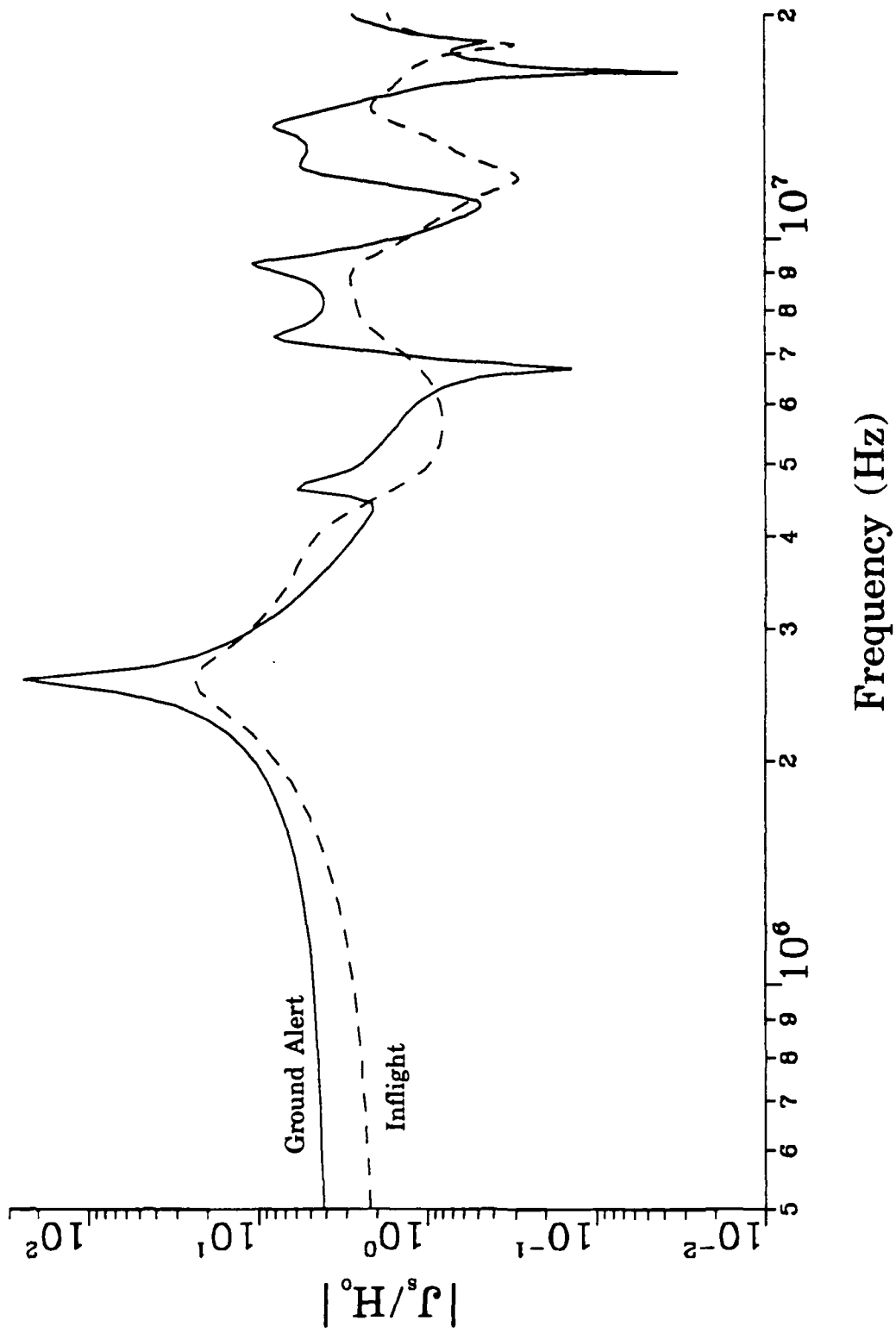


Figure 9. The EMPTAC normalized current density on the bottom of the mid fuselage (18.69 m from the wing-fuselage junction) for topside plane wave incidence with  $E \parallel$  to the fuselage.

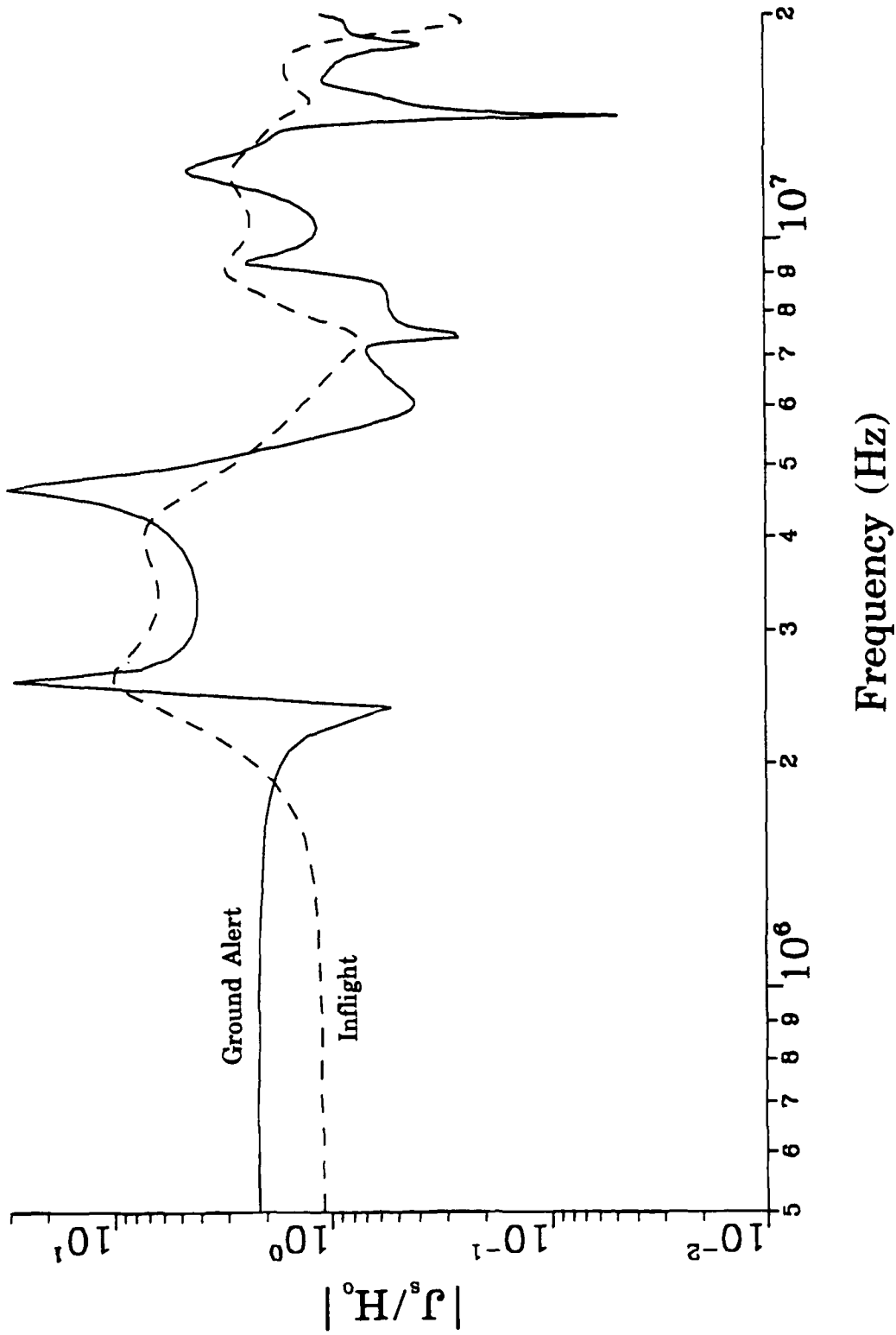


Figure 10. The EMPTAC normalized current density on the top of the port wing (3.9 m from the wing-fuselage junction) for topside plane wave incidence with  $E \parallel$  to the fuselage.

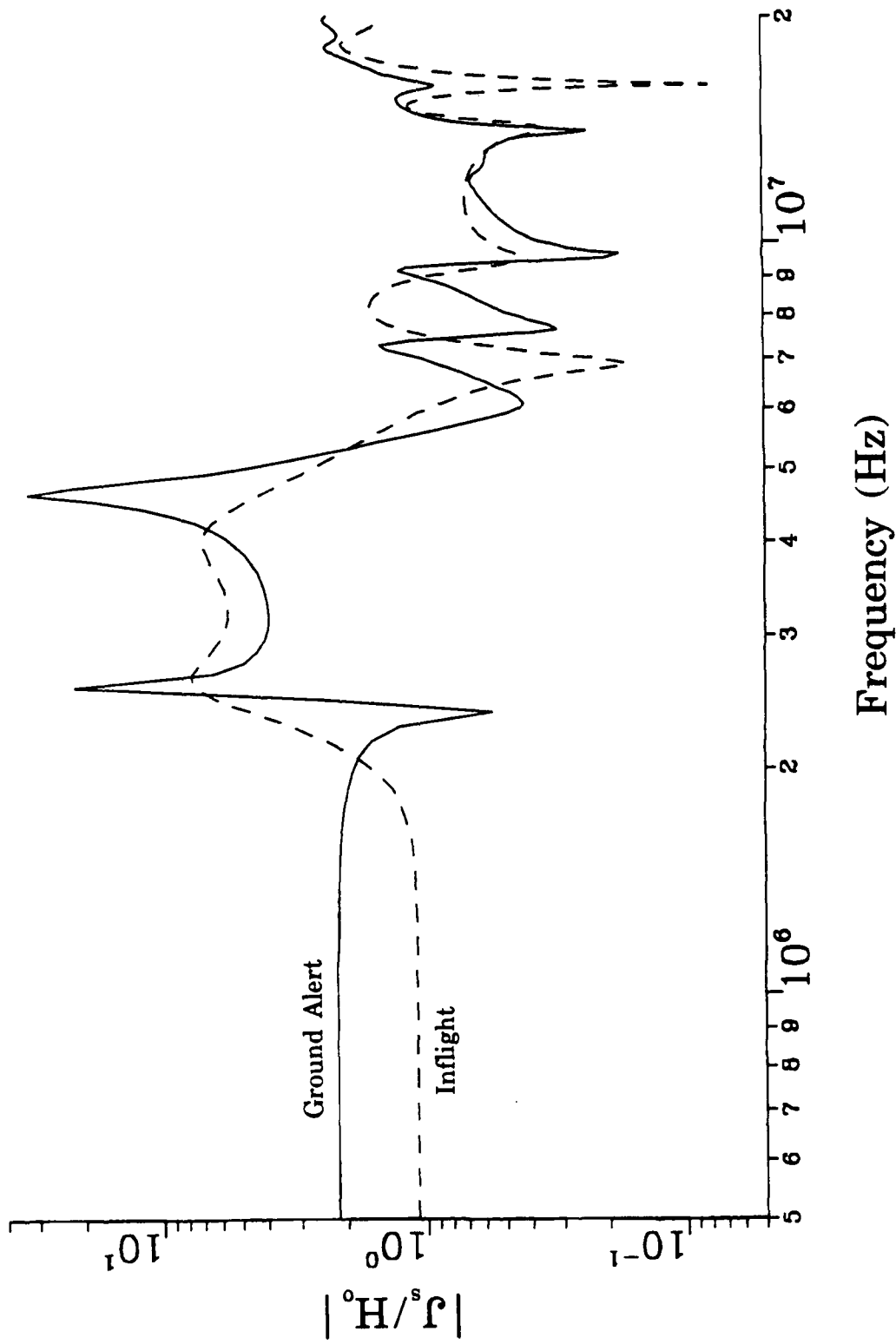


Figure 11. The EMPTAC normalized current density on the top of the port wing (11.7 m from the wing-fuselage junction) for topside plane wave incidence with  $E \parallel$  to the fuselage.

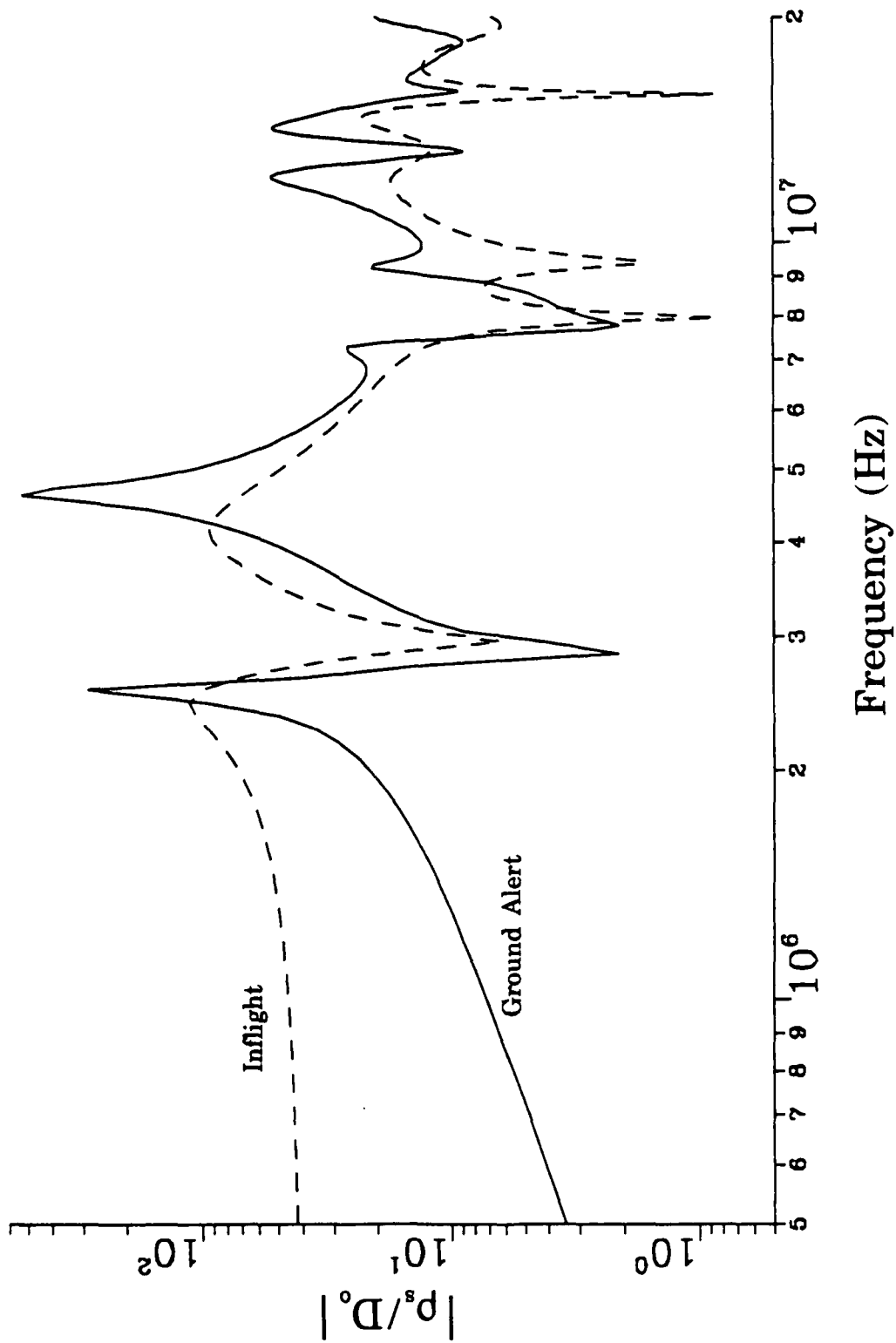


Figure 12. The EMPTAC normalized charge density on the tip of the nose for topside plane wave incidence with  $E \parallel$  to the fuselage

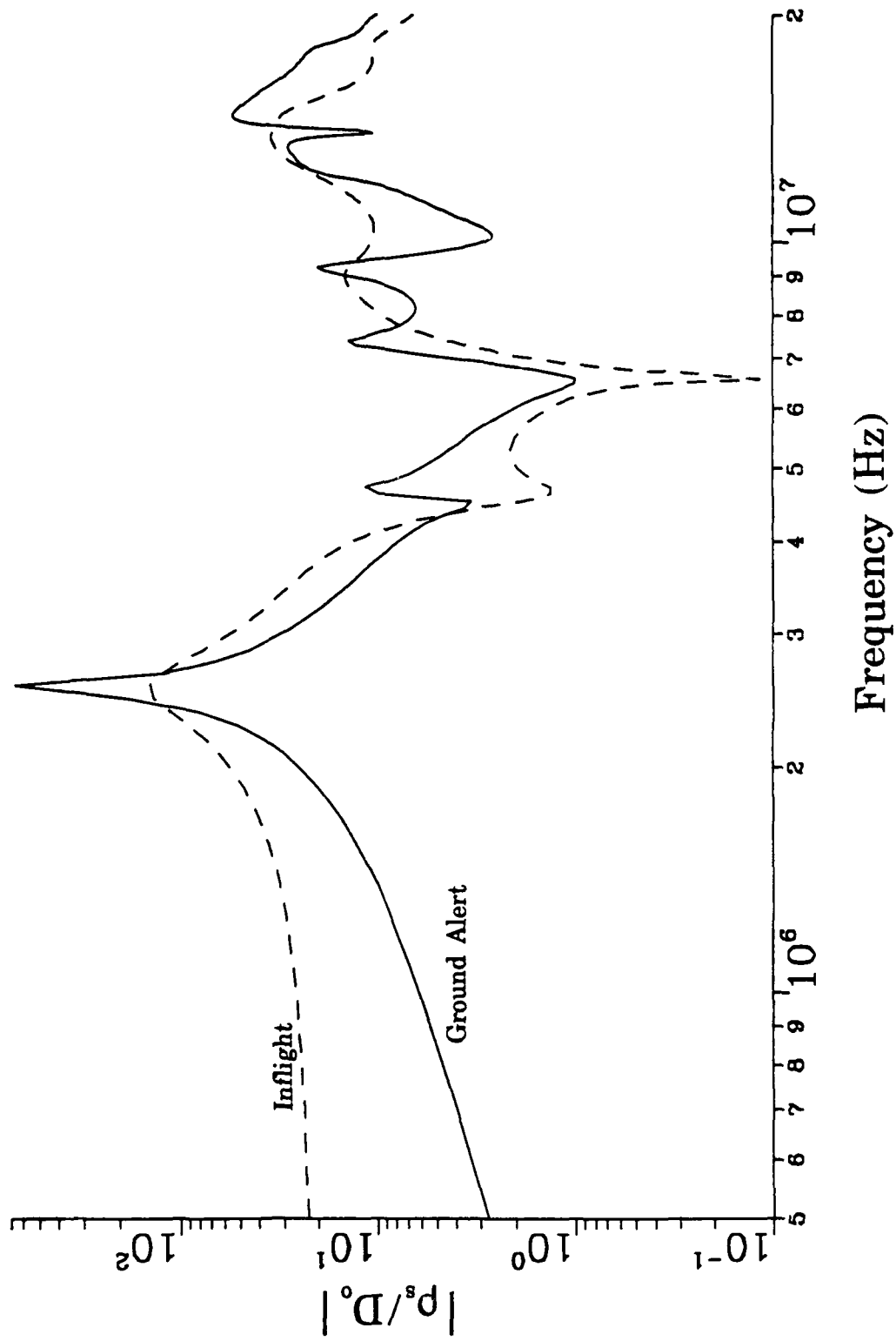


Figure 13. The EMPTAC normalized charge density on the tip of the vertical stabilizer for topside plane wave incidence with E || to the fuselage.

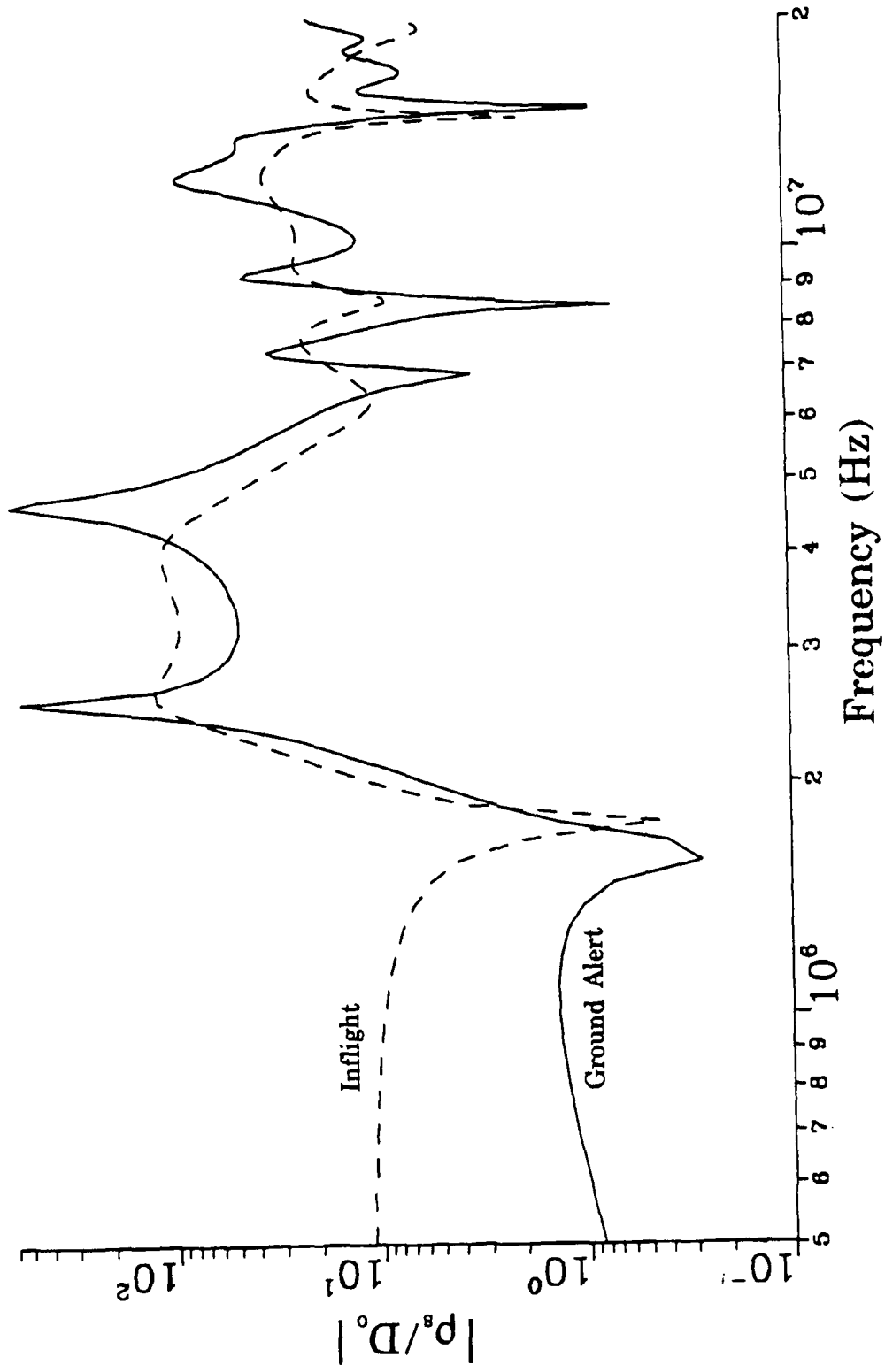


Figure 14. The EMPTAC normalized charge density on the tip of the port wing for topside plane wave incidence with  $E||$  to the fuselage.

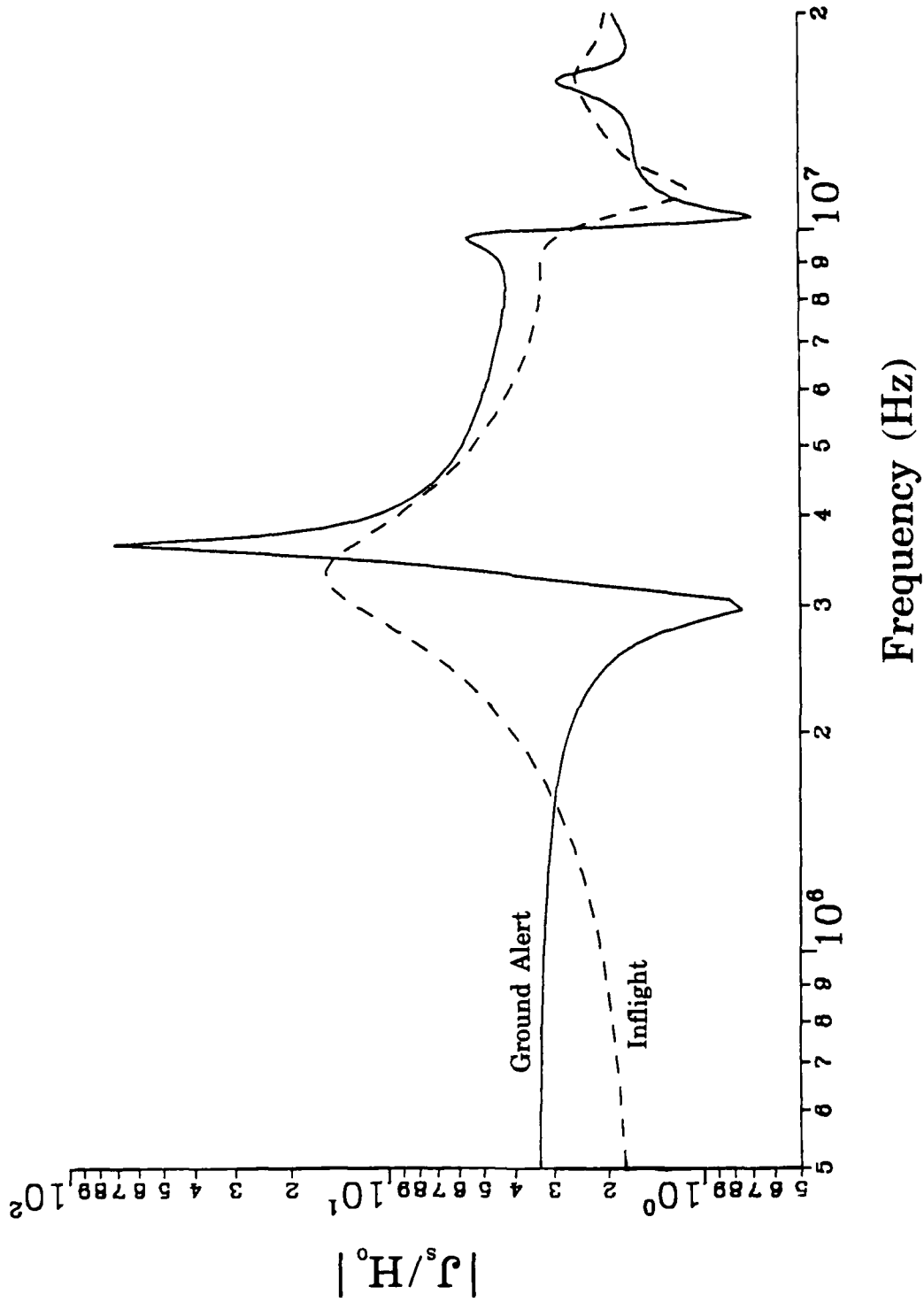


Figure 15. The EMPTAC normalized current density on the top of the port wing (3.9 m from the wing-fuselage junction) for topside plane wave incidence with  $E \perp$  to the fuselage.

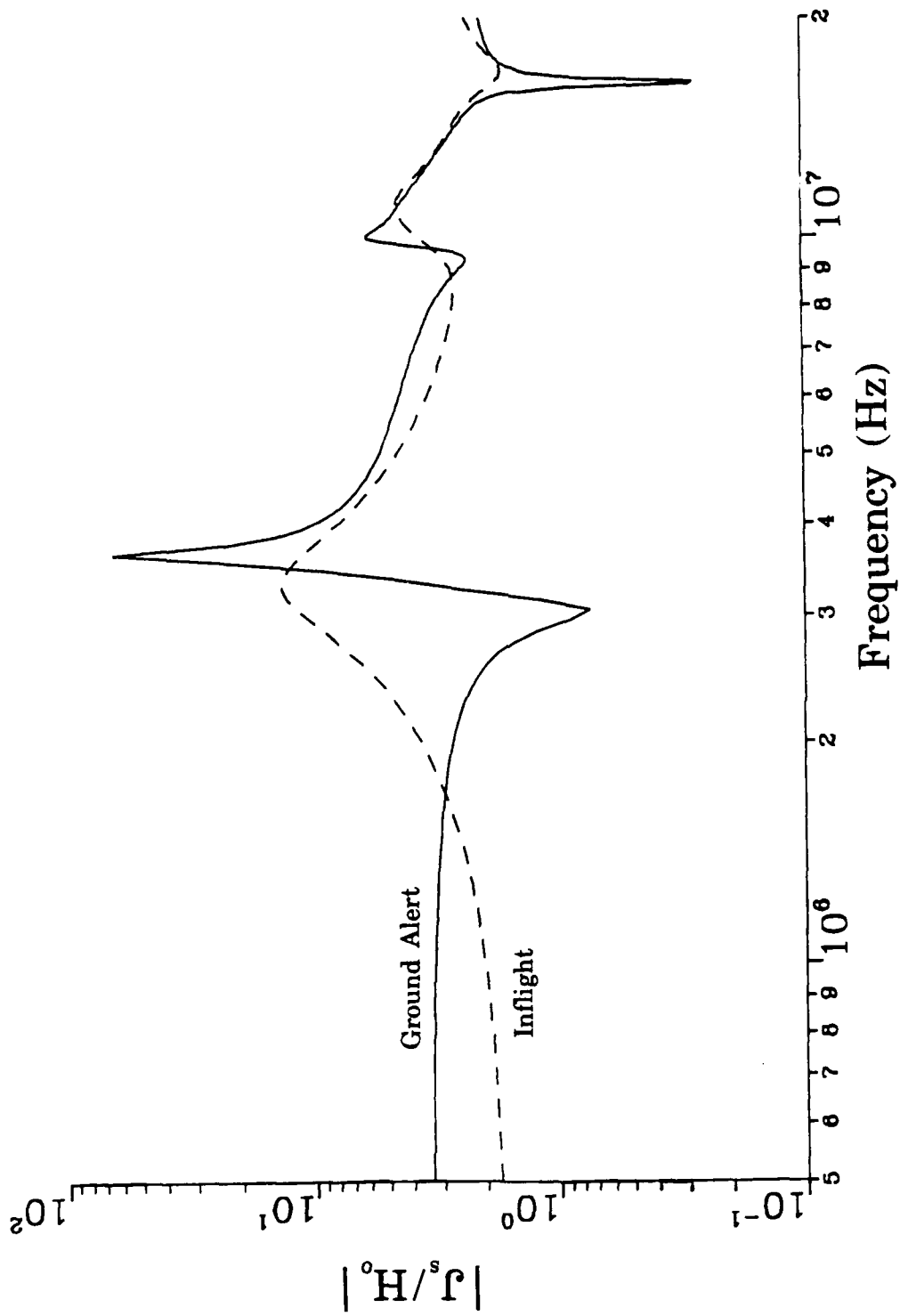


Figure 16. The EMPTAC normalized current density on the top of the port wing (11.7 m from the wing-fuselage junction) for topside plane wave incidence with  $E \perp$  to the fuselage.

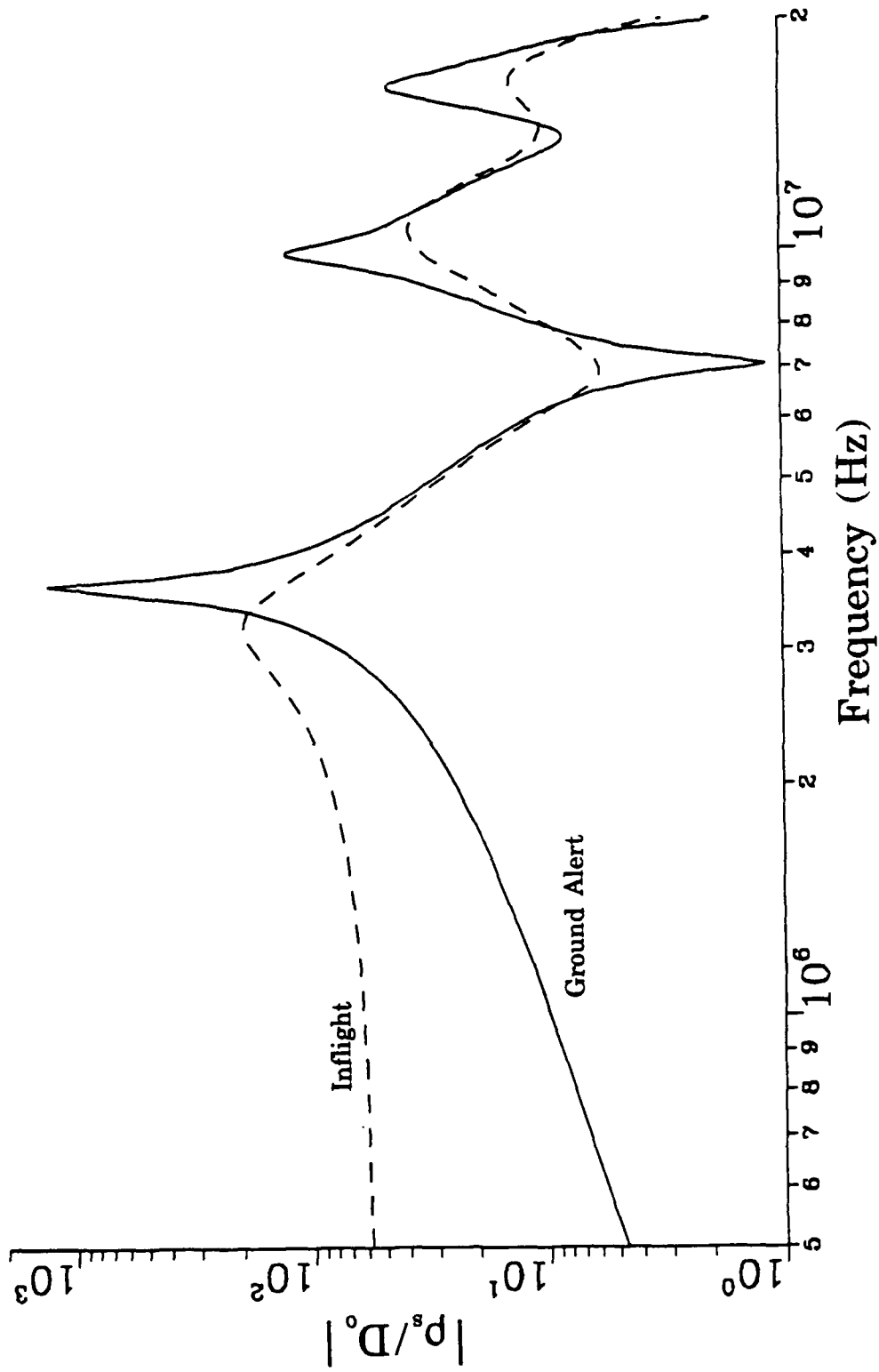


Figure 17. The EMPTAC normalized charge density on the tip of the port wing for topside plane wave incidence with  $E \perp$  to the fuselage.

- o the fin-cap antenna only
- o the fin-cap and nose antennas
- o the port wing antenna only
- o the port and starboard wing antennas

To generate incident fields which are comparable in magnitude to the plane wave excitations considered in paragraph 3.1, the average power radiated by each active antenna ( $P_{\text{rad}}$ ) is assumed to be 10 W over the frequency range of interest (500 kHz to 100 MHz).

Given a constant radiated power of 10 W over the entire frequency range, the resulting peak antenna drive current ( $I_0$ ) varies according to

$$P_{\text{rad}} = \frac{1}{2} |I_0|^2 R_r \quad (16)$$

where  $R_r$  is the radiation resistance of the antenna. The radiation resistance of the infinitely thin center-fed dipole of length 2 m versus frequency is shown in Figure 18. At low frequencies, extremely large drive currents are required to radiate 10 W due to the small values of radiation resistance. Therefore, the incident fields produced by the HF antenna model are significantly larger at low frequencies. Figure 19 illustrates the total incident electric and magnetic fields at certain points on the EMPTAC when the fin-cap antenna is driven with  $P_{\text{rad}} = 10$  W. As the frequency increases, the incident field magnitudes become relatively constant at values similar to those of the incident plane wave considered previously. The variation in magnitude of the incident field components with frequency skews the EMPTAC surface responses. The surface responses are excited by HF antennas toward the lower frequencies when compared to the surface responses excited by an incident plane wave.

The EMPTAC surface responses to HF antenna excitation are computed for the inflight and ground alert modes. The surface current approximation used for plane wave excitation of the EMPTAC are also used for HF antenna excitation. Specifically, Equation 5 is used for the inflight mode while Equation 7 is used for the ground alert mode. The surface responses are normalized using the same constants as was used for the plane wave responses ( $J_s/H_0$  and  $\rho_s/D_0$ ).

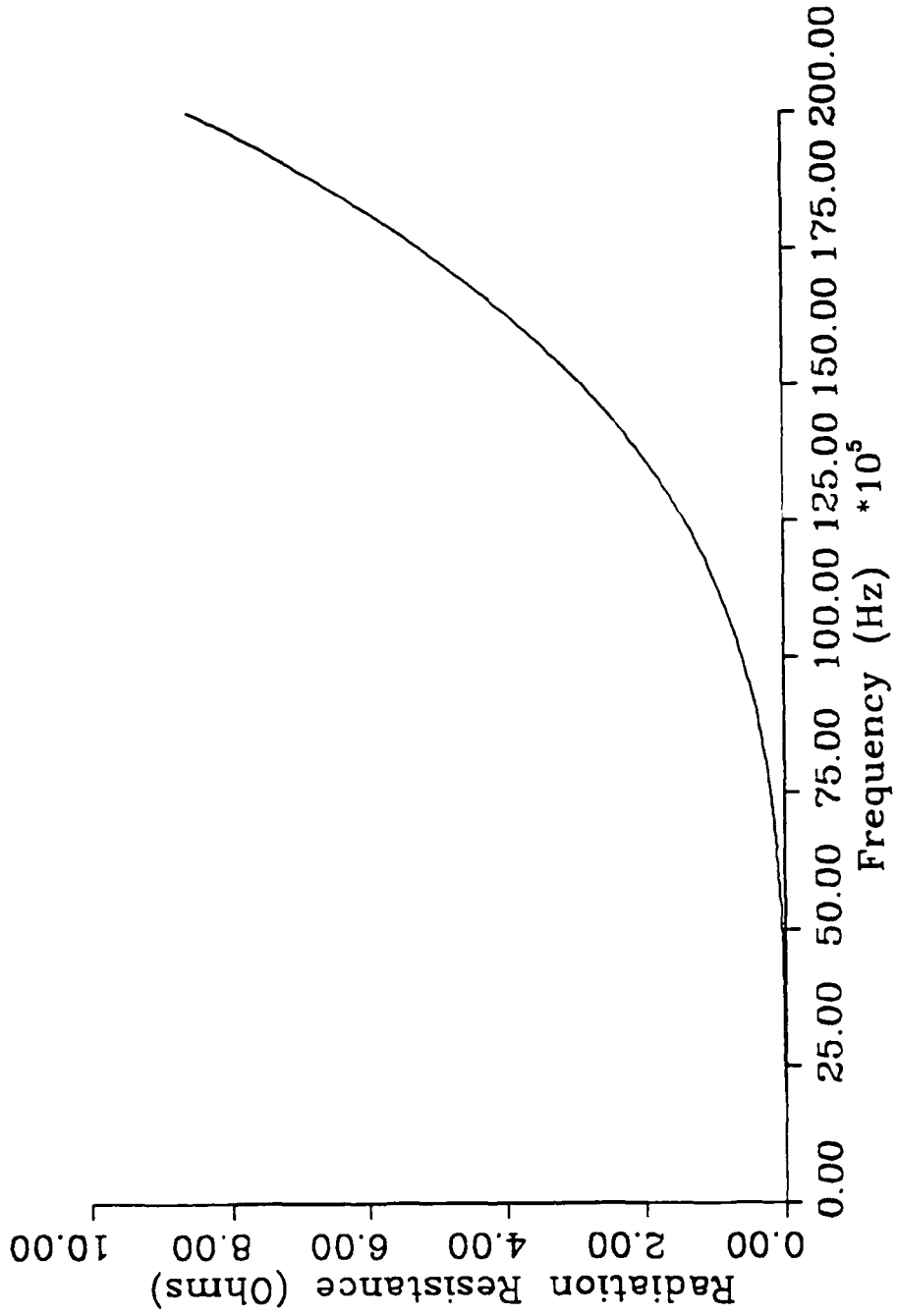
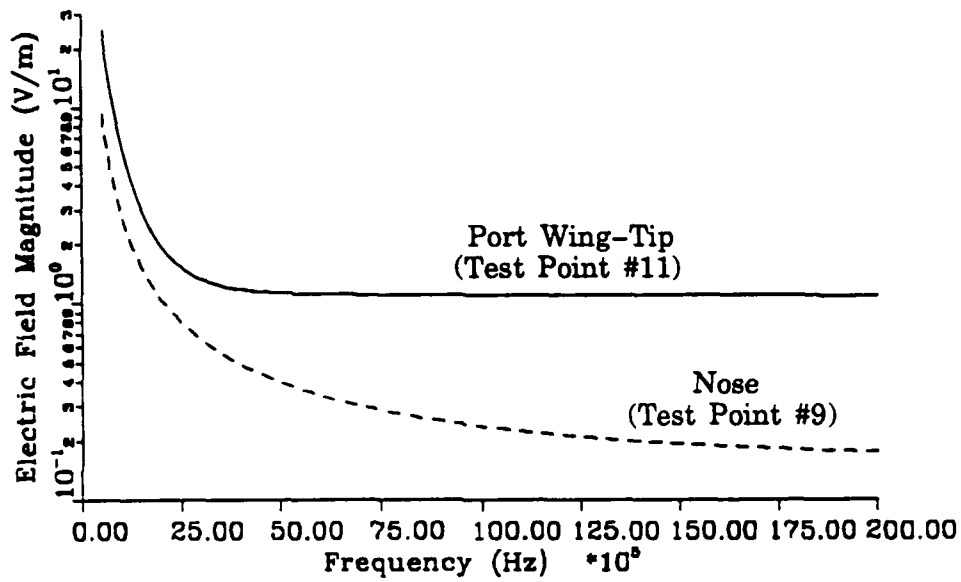
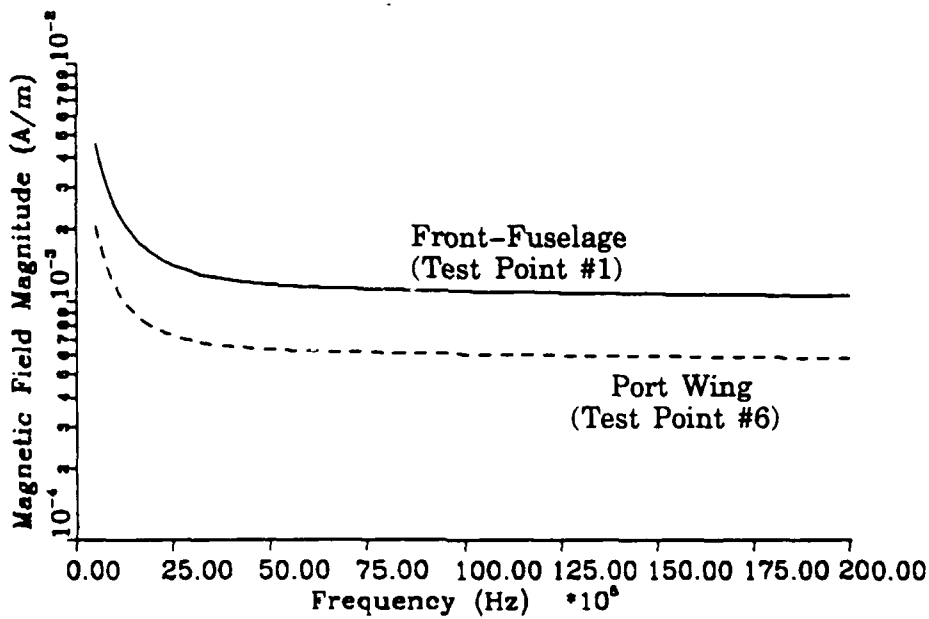


Figure 18. Radiation resistance of the HF antenna model between 500 kHz and 20 MHz.



(a) Electric field at the nose (test point #9) and the tip of the port wing (test point #11).



(b) Magnetic field on the top of the port wing (test point #6) and on top of the front fuselage (test point #1).

Figure 19. Magnitude of the total incident fields at points on the EMPTAC for fin-cap antenna drive ( $P_{rad} = 10$  W).

### 3.2.1 Response of the EMPTAC to Excitation of the Fin-Cap Antenna (0.5 to 20 MHz)

The normalized responses of the EMPTAC to excitation of the fin-cap antenna are shown in Figures 20 through 27. Figures 20 and 21 represent the normalized current density on the top and bottom of the front fuselage (test points #1 and #2, respectively). Figures 22 and 23 represent the normalized current density on the top and bottom of the mid fuselage (test points #3 and #4, respectively). Figures 24 and 25 represent the normalized current density at points on the top of the port wing (test points #5 and #6, respectively). Figures 26 and 27 represent the normalized charge densities on the tip of the nose (test point #9) and on the tip of the port wing (test point #11, respectively). The starboard wing responses (test points #7, #8 and #12) predicted by the method-of-moments solution are identical to those of the port wing.

### 3.2.2 Response of the EMPTAC to Excitation of the Nose and Fin-Cap Antenna (0.5 to 20 MHz)

The normalized responses of the EMPTAC to simultaneous excitation of the nose and fin-cap antennas are shown in Figures 28 through 34. Figures 28 and 29 represent the normalized current density on the top and bottom of the front fuselage (test points #1 and #2, respectively). Figures 30 and 31 represent the normalized current density on the top and bottom of the mid fuselage (test points #3 and #4, respectively). Figures 32 and 33 represent the normalized current density at points on the top of the port wing (test points #5 and #6, respectively). Figure 34 represents the normalized charge density on the tip of the port wing (test point #11). The starboard wing responses (test points #7, #8 and #12) predicted by the method-of-moments solution are identical to those of the port wing.

### 3.2.3 Response of the EMPTAC to Excitation of the Port Wing Antenna (0.5 to 20 MHz)

The normalized responses of the EMPTAC to excitation of the port wing antenna are shown in Figures 35 through 45. Figures 35 and 36 represent the normalized current density on the top and bottom of the front fuselage (test points #1 and #2, respectively). Figures 37 and 38 represent the normalized

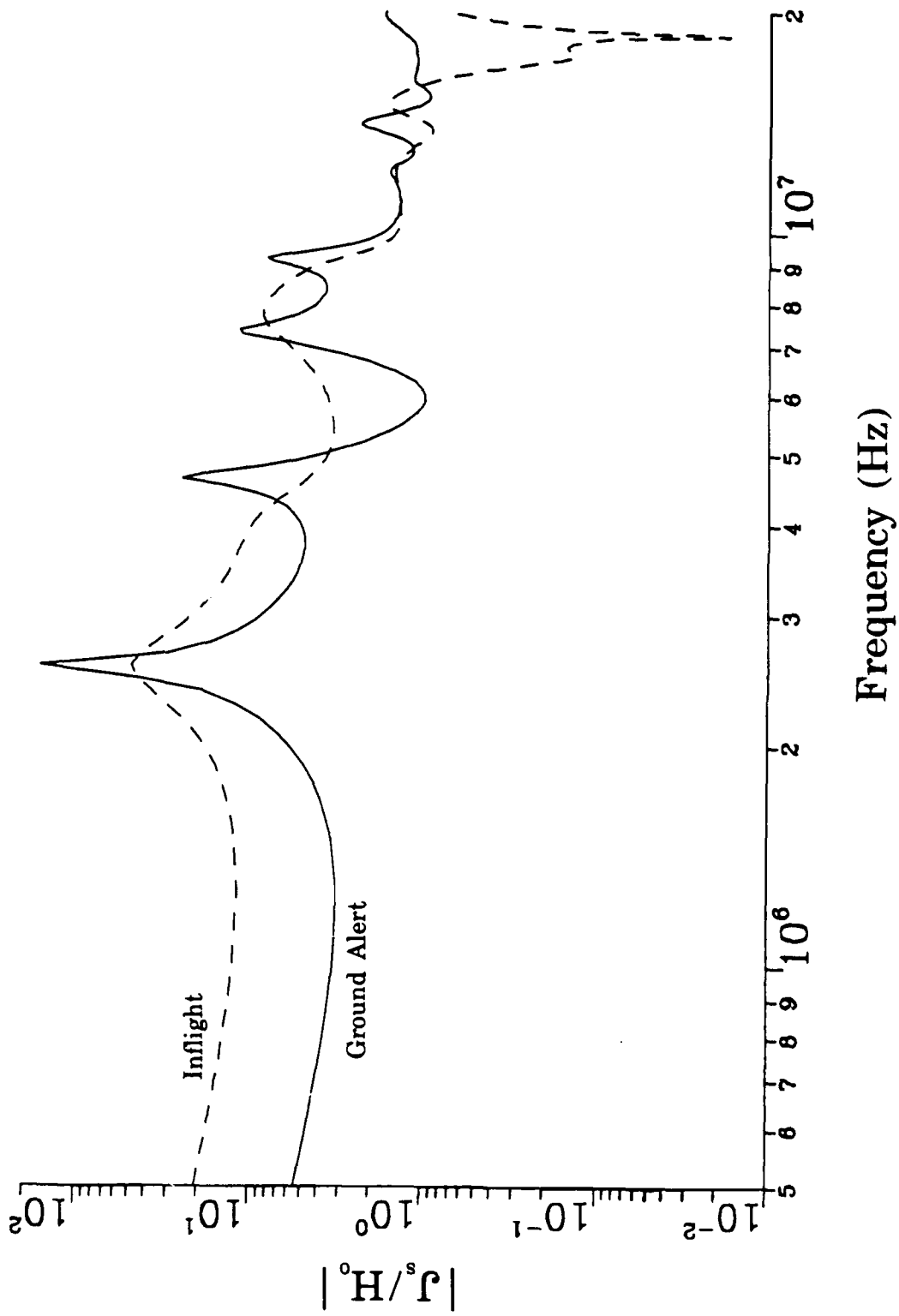


Figure 20. The EMPTAC normalized current density on the top of the front fuselage (10.29 m from the nose) for fin-cap antenna excitation.

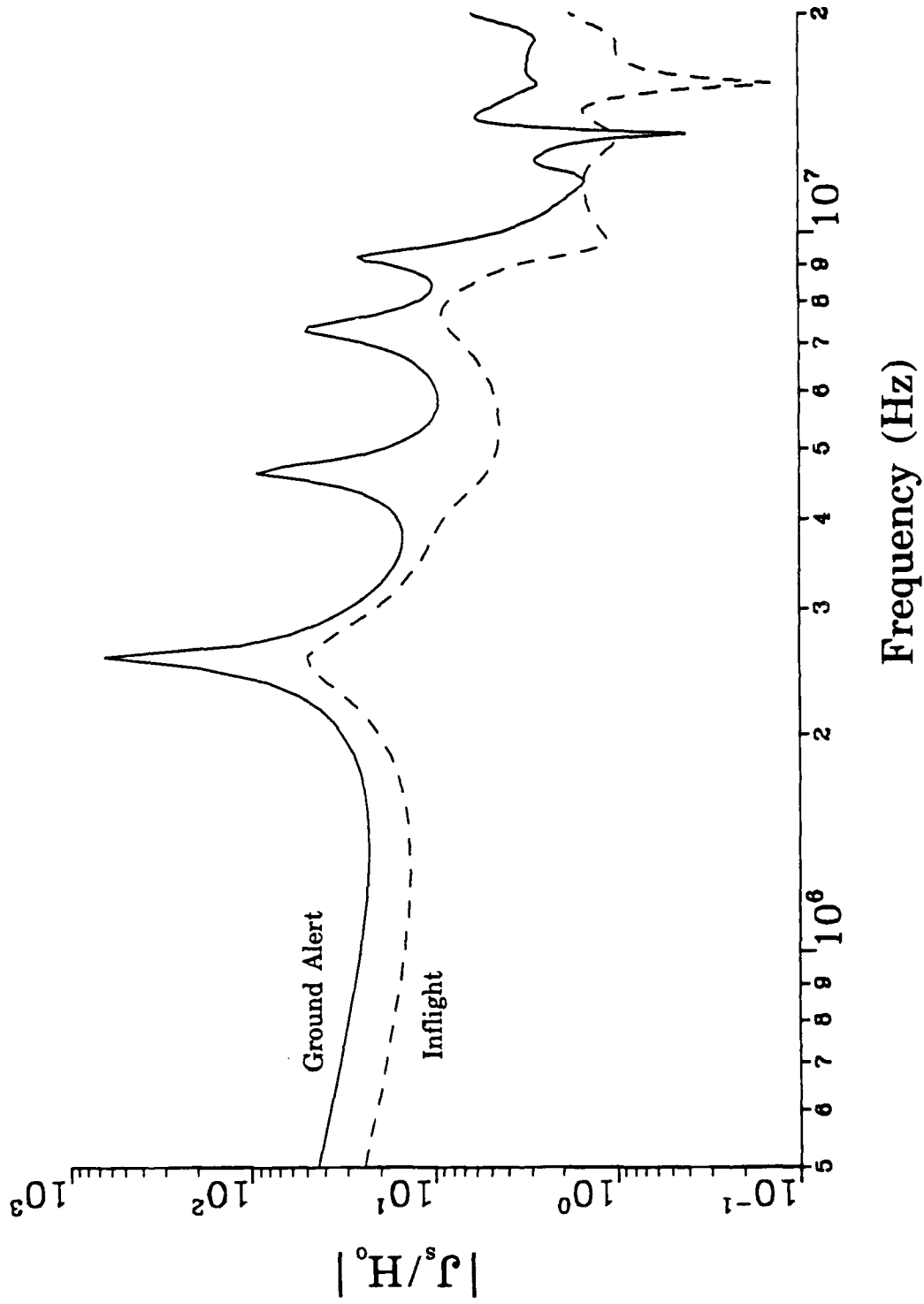


Figure 21. The EMPTAC normalized current density on the bottom of the front fuselage (10.29 m from the nose) for fin-cap antenna excitation.

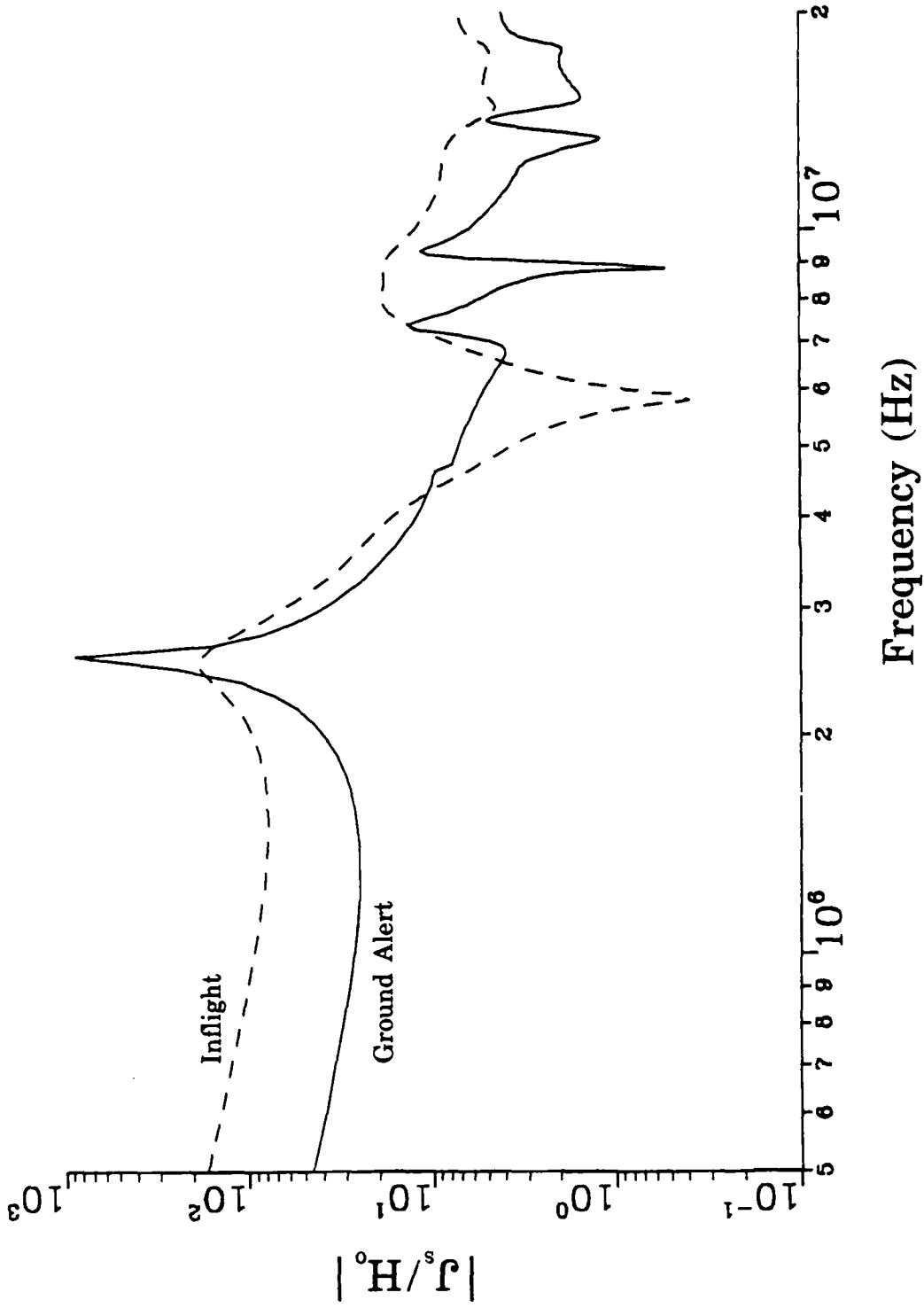


Figure 22. The EMP-TAC normalized current density on the top of the mid fuselage (18.69 m from the wing-fuselage junction) for fin-cap antenna excitation.

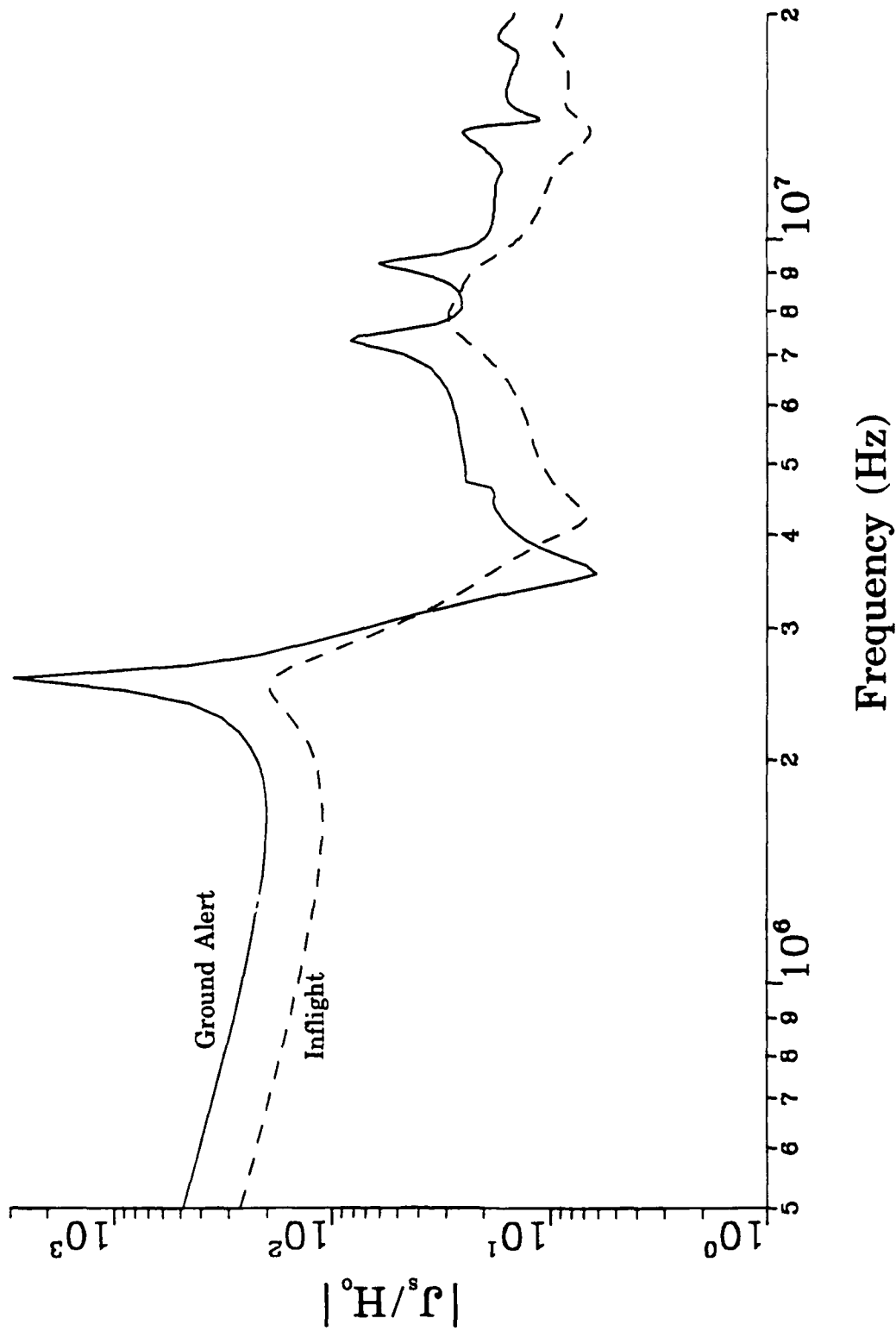


Figure 23. The EMPTAC normalized current density on the bottom of the mid fuselage (18.69 m from the wing-fuselage junction) for fin-cap antenna excitation.

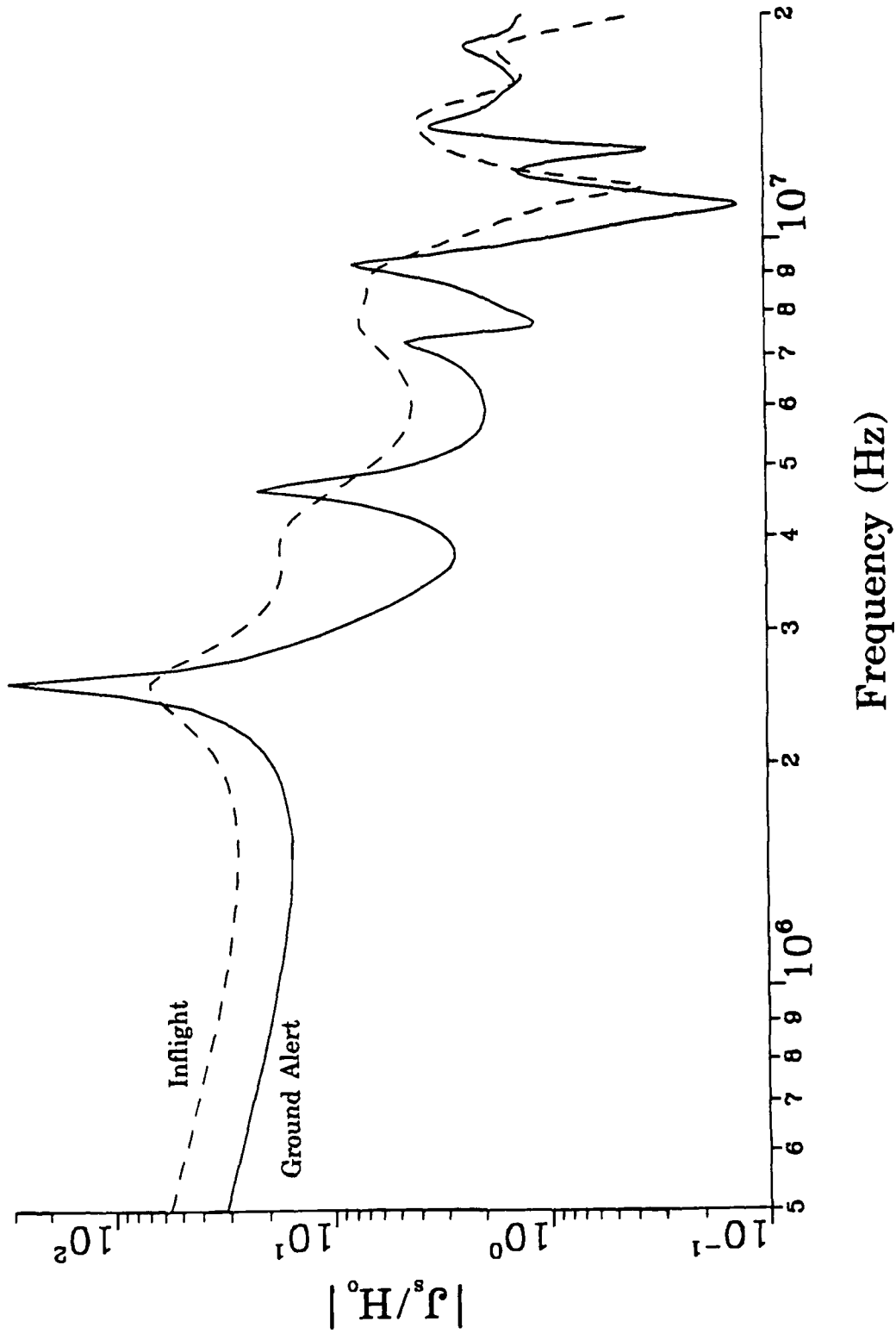


Figure 24. The EMPTAC normalized current density on the top of the port wing (3.9 m from the wing-fuselage junction) for fin-cap antenna excitation.

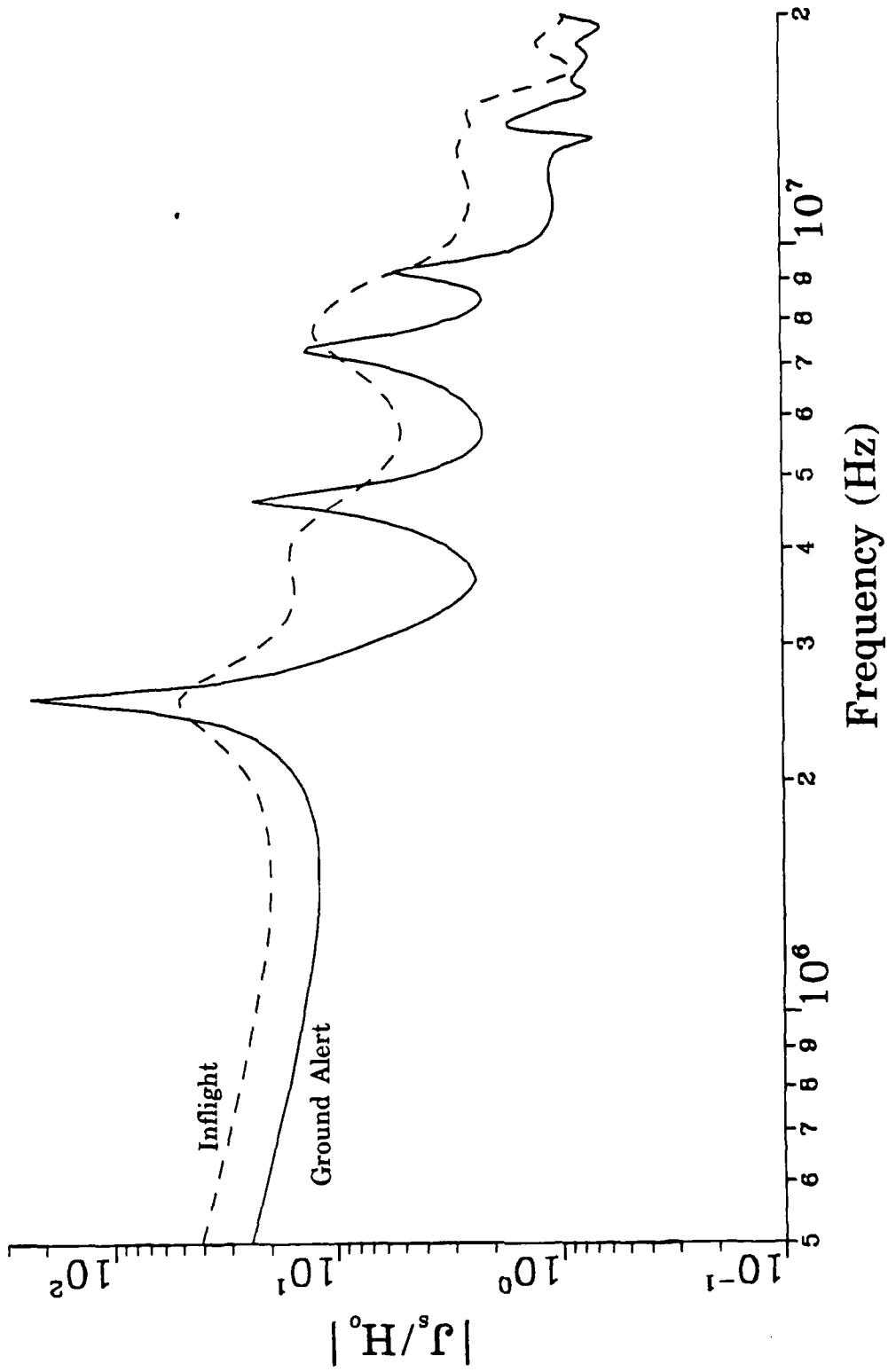


Figure 25. The EMPTAC normalized current density on the top of the port wing (11.7 m from the wing-fuselage junction) for fin-cap antenna excitation.

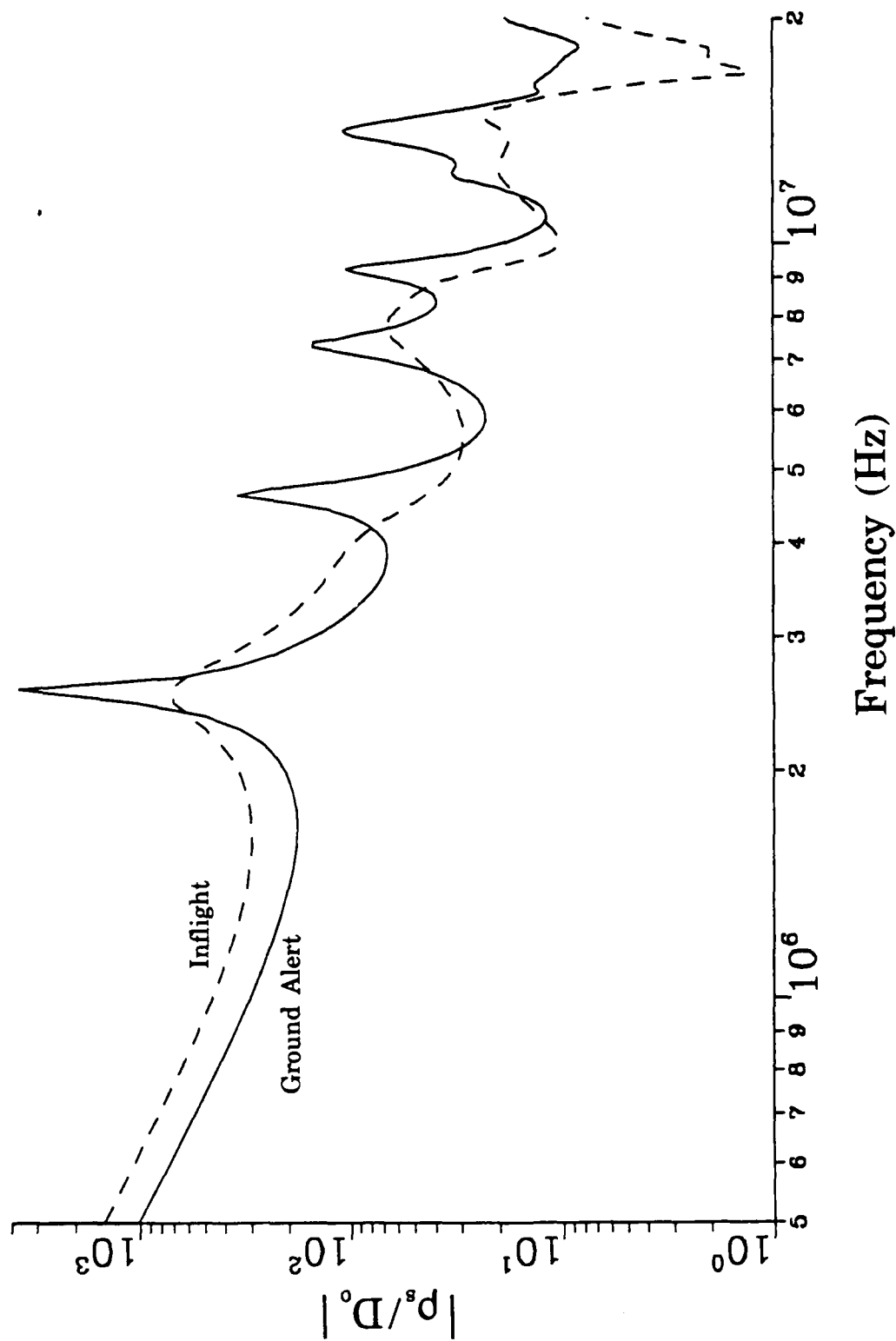


Figure 26. The EMPTAC normalized charge density on the tip of the nose for fin-cap antenna excitation.

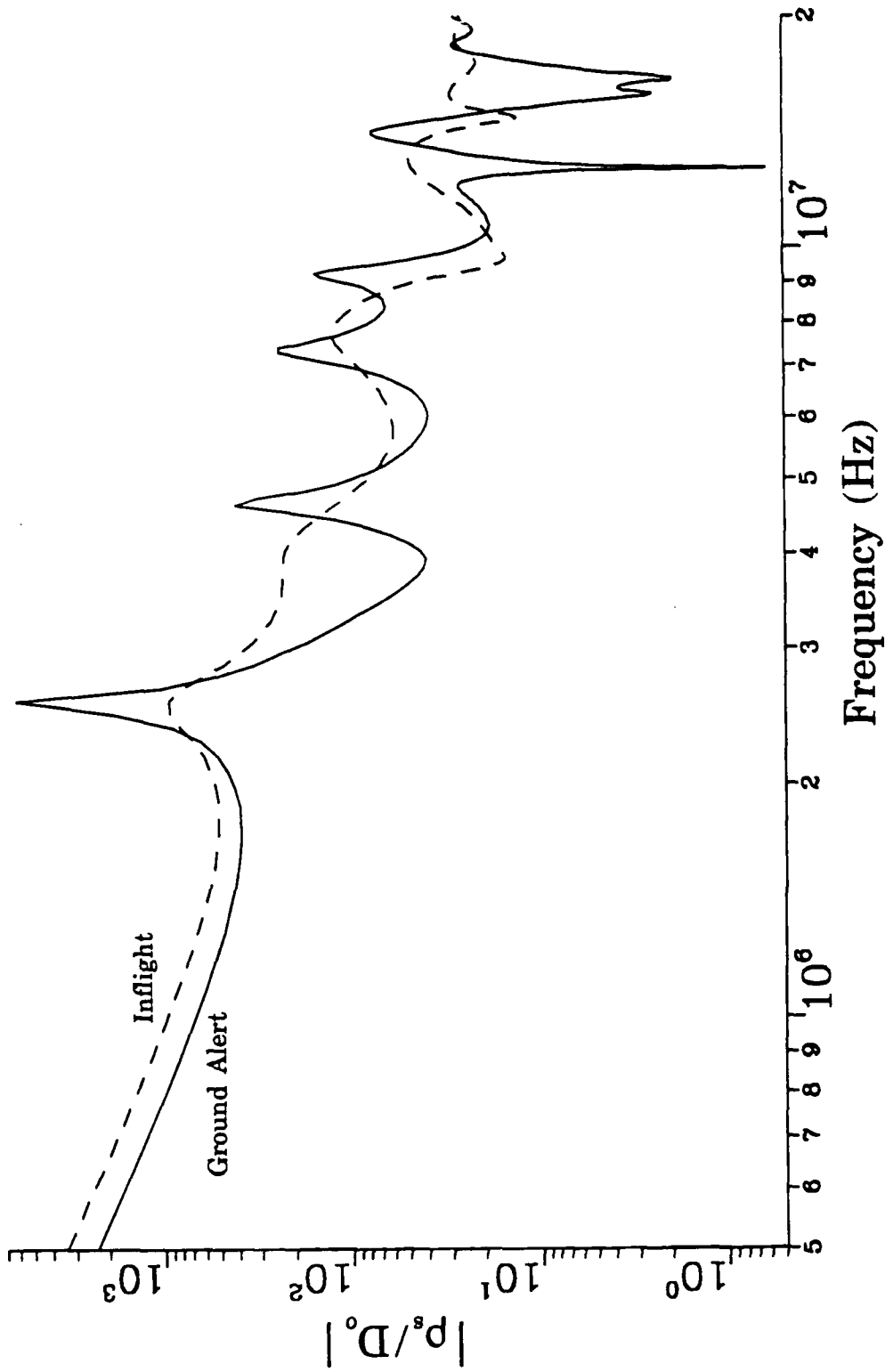


Figure 27. The EMPTAC normalized charge density on the tip of the port wing for fin-cap antenna excitation.

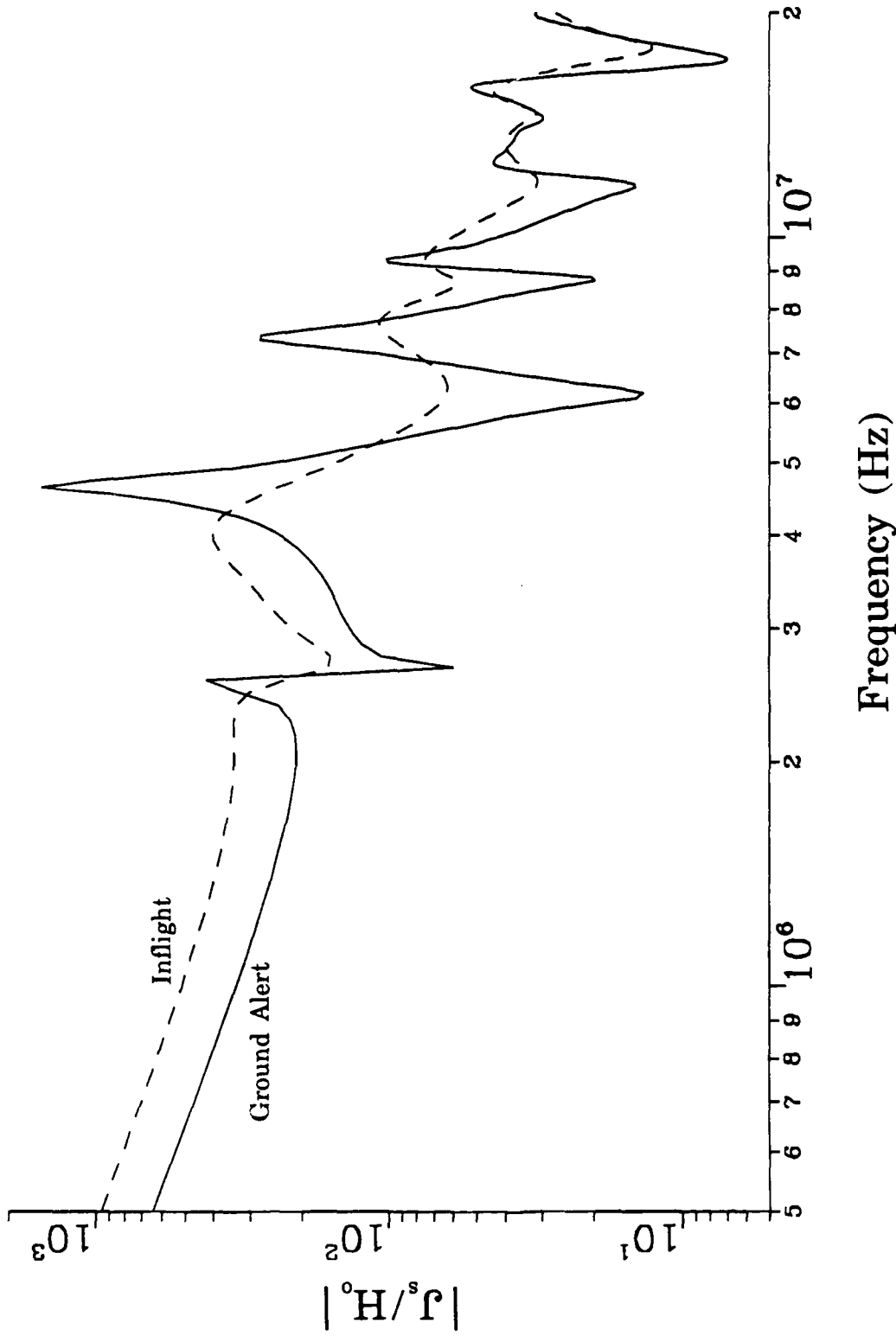


Figure 28. The EMPTAC normalized current density on the top of the front fuselage (10.29 m from the nose) for nose and fin-cap antenna excitation.

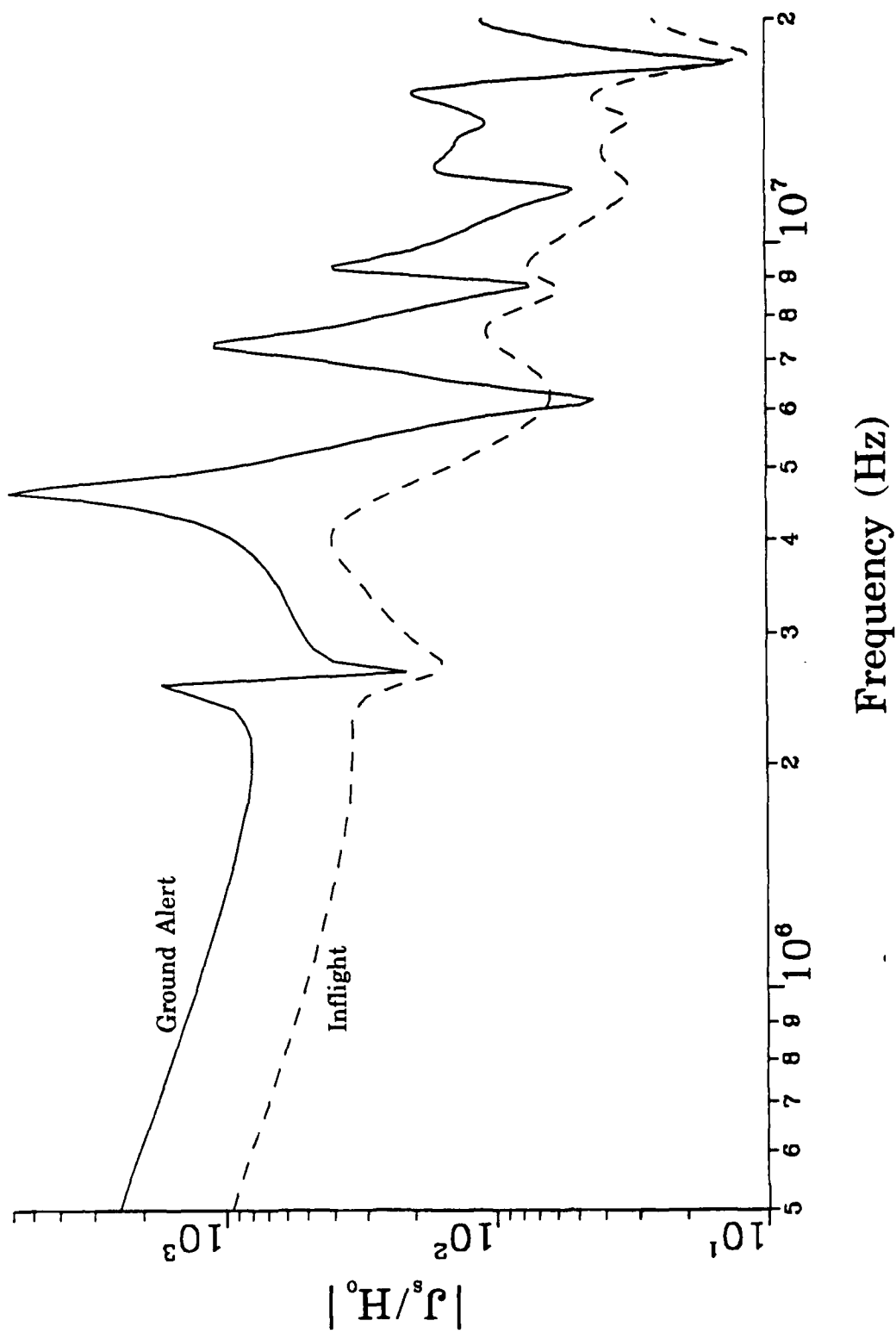


Figure 29. The EMPTAC normalized current density on the bottom of the front fuselage (10.29 m from the nose) for nose and fin-cap antenna excitation.

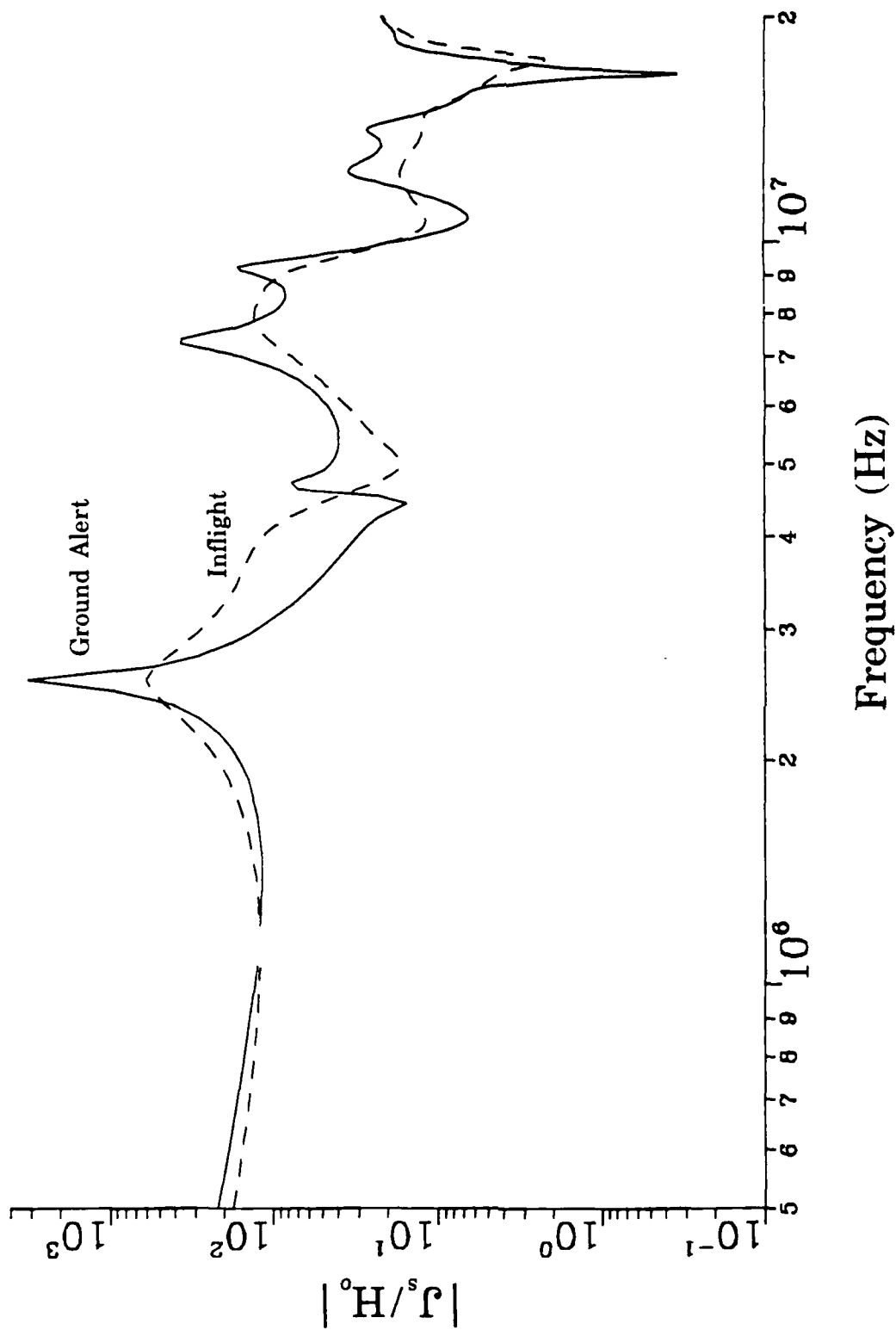


Figure 30. The EMPTAC normalized current density on the top of the mid fuselage (18.69 m from the wing-fuselage junction) for nose and fin-cap antenna excitation.

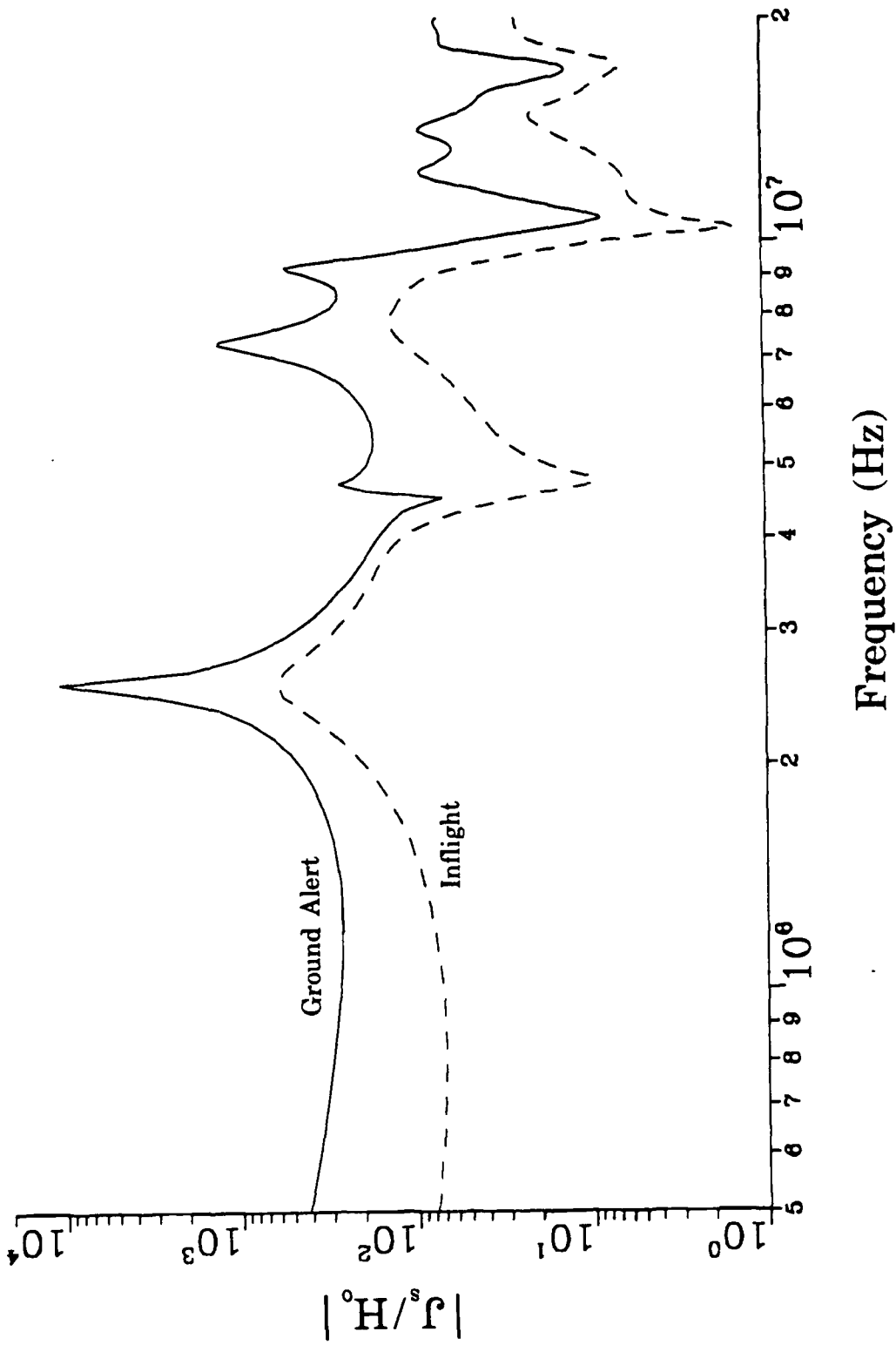


Figure 31. The EMPTAC normalized current density on the bottom of the mid fuselage (18.69 m from the wing-fuselage junction) for nose and fin-cap antenna excitation.

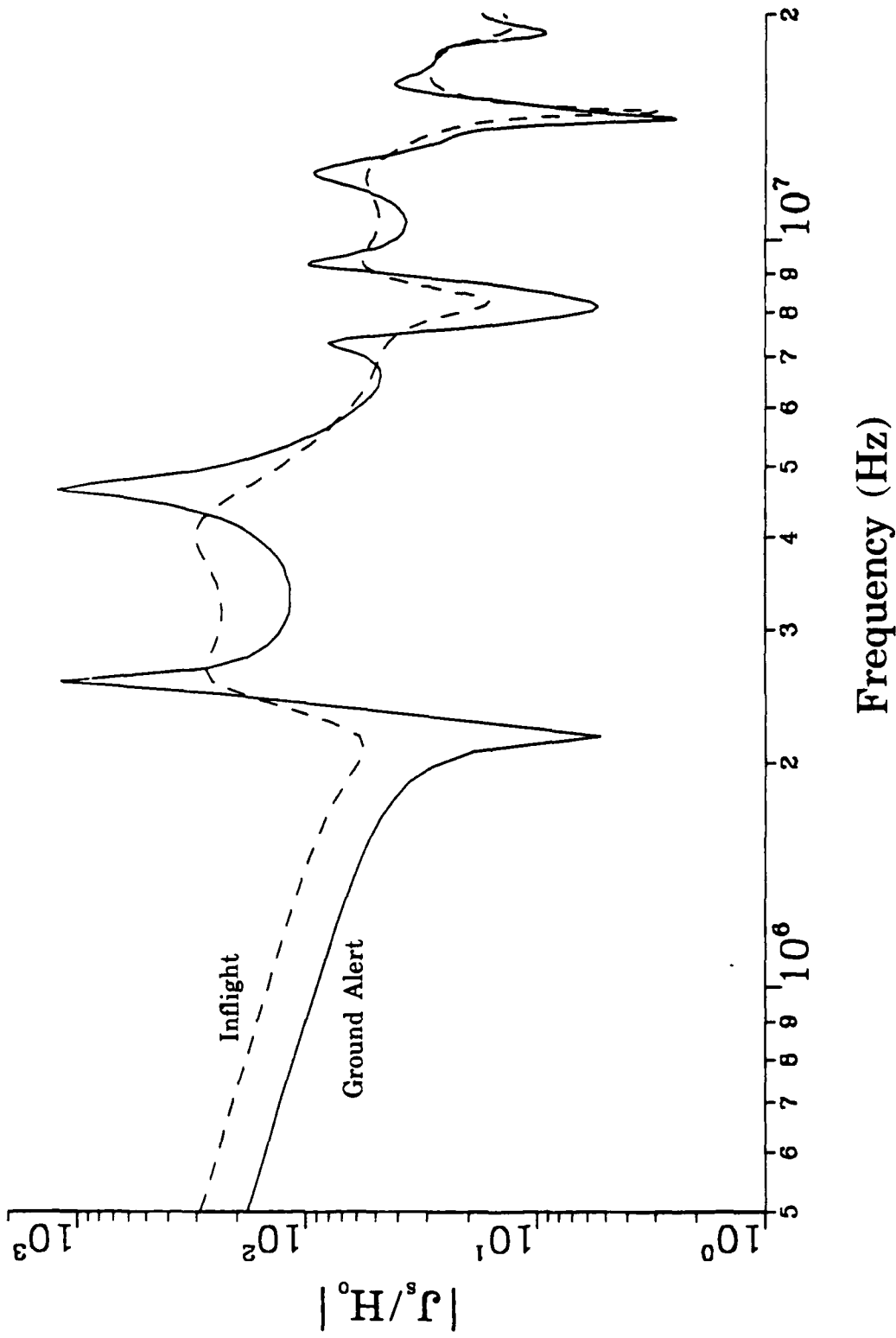


Figure 32. The EMPTAC normalized current density on the top of the port wing (3.9 m from the wing-fuselage junction) for nose and fin-cap antenna excitation.

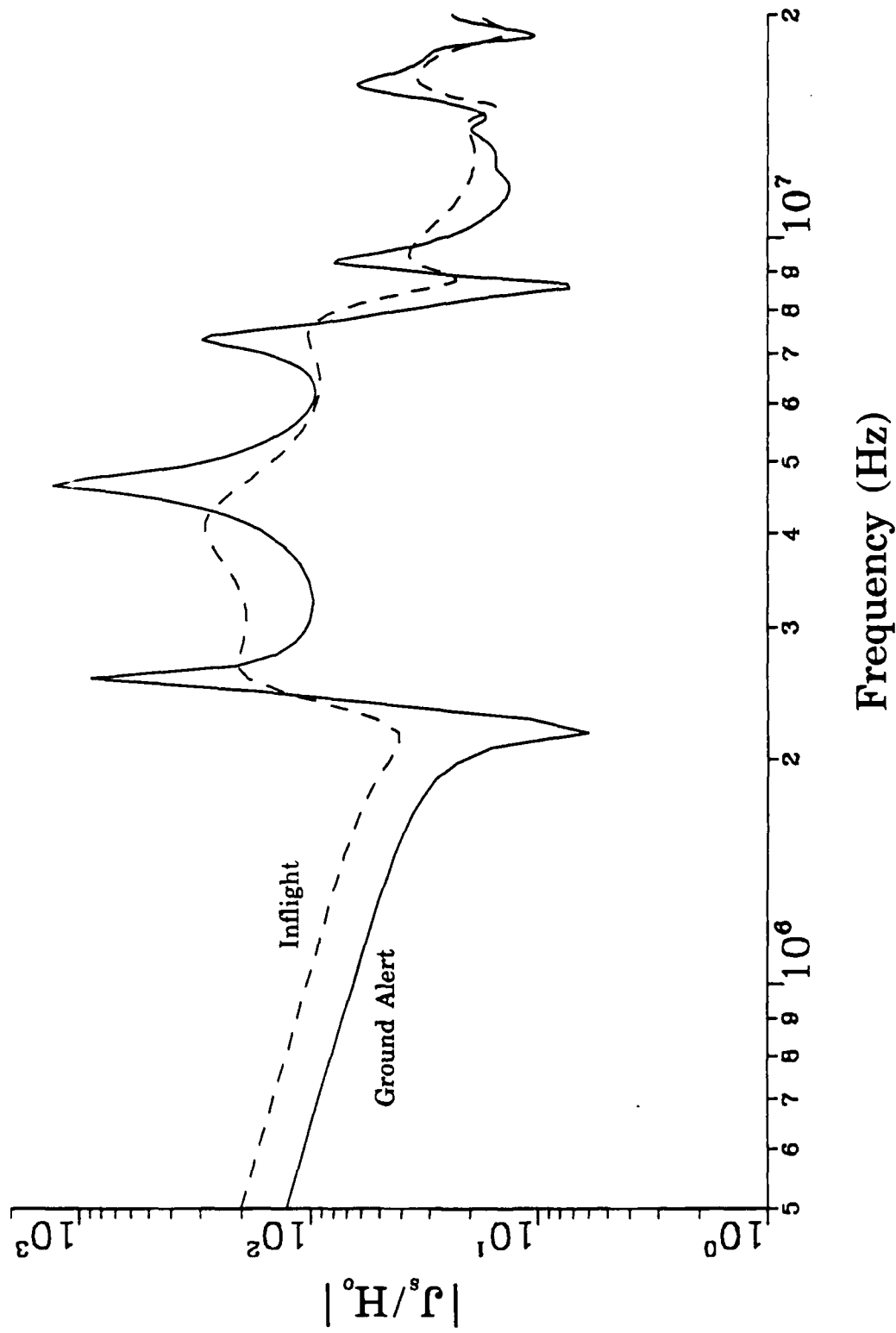


Figure 33. The EMPTAC normalized current density on the top of the port wing (11.7 m from the wing-fuselage junction) for nose and fin-cap antenna excitation.

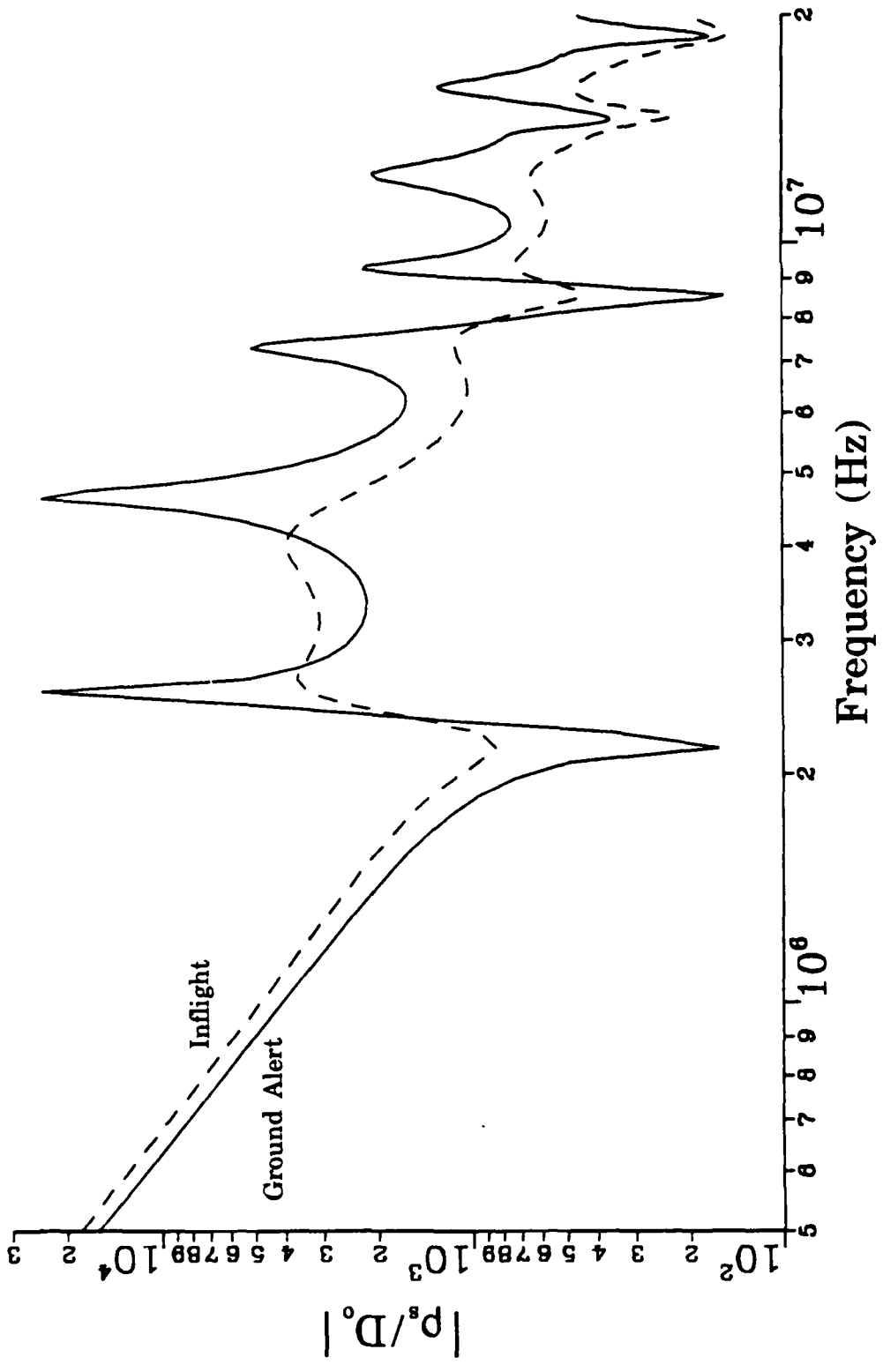


Figure 34. The EMPTAC normalized charge density on the tip of the port wing for nose and fin-cap antenna excitation.

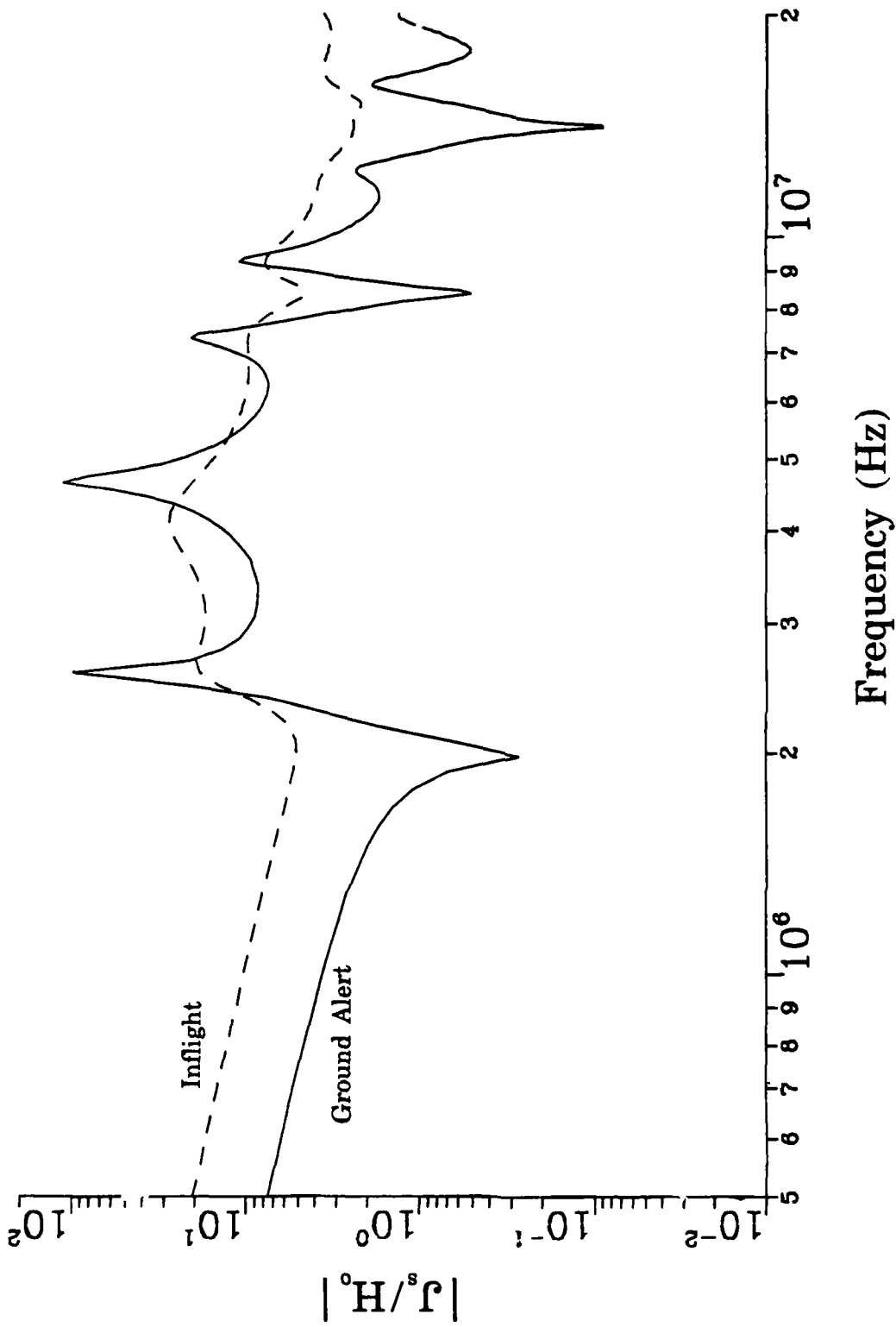


Figure 35. The EMPTAC normalized current density on the top of the front fuselage (10.29 m from the nose) for port wing antenna excitation.

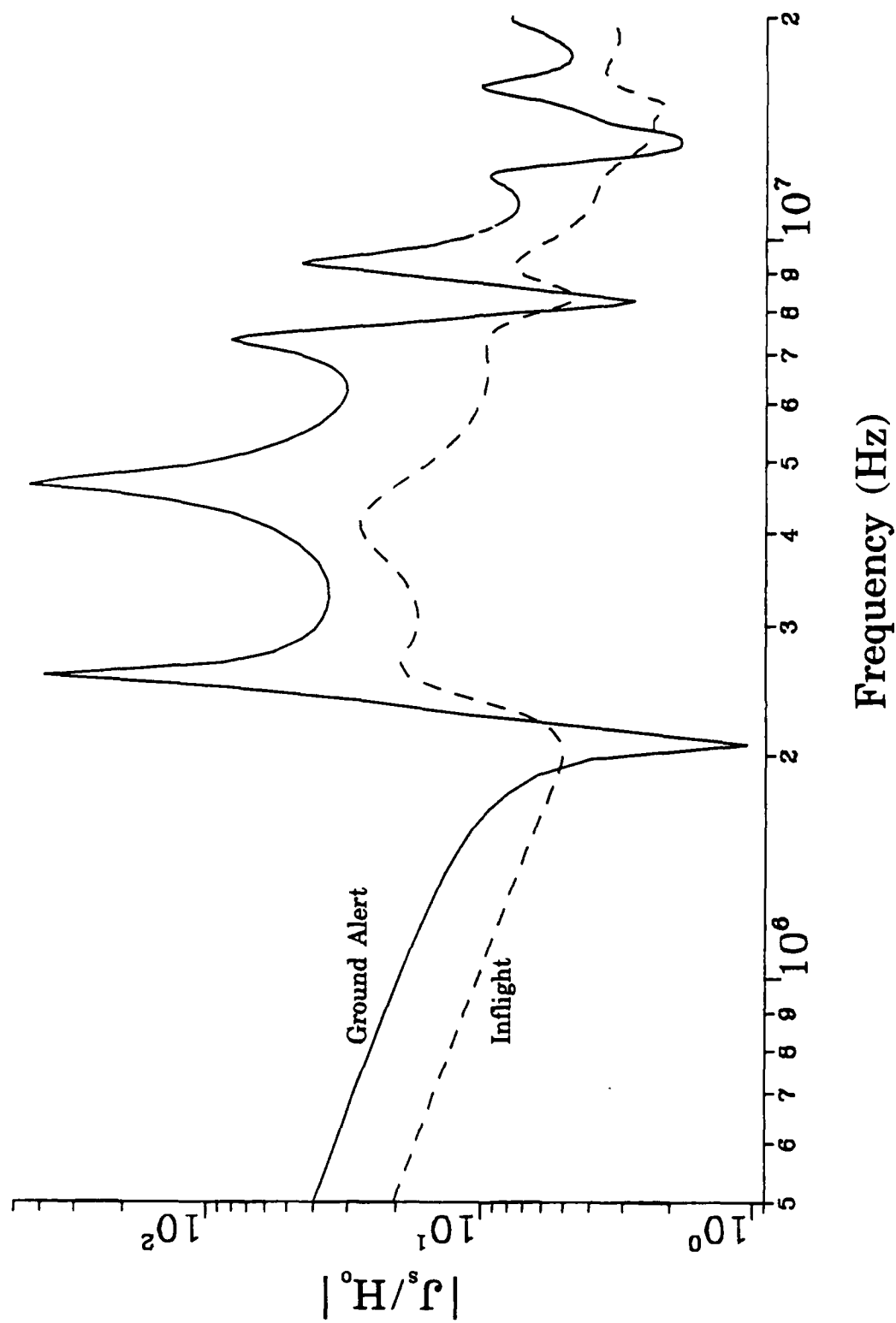


Figure 36. The EMPTAC normalized current density on the bottom of the front fuselage (10.29 m from the nose) for port wing antenna excitation.

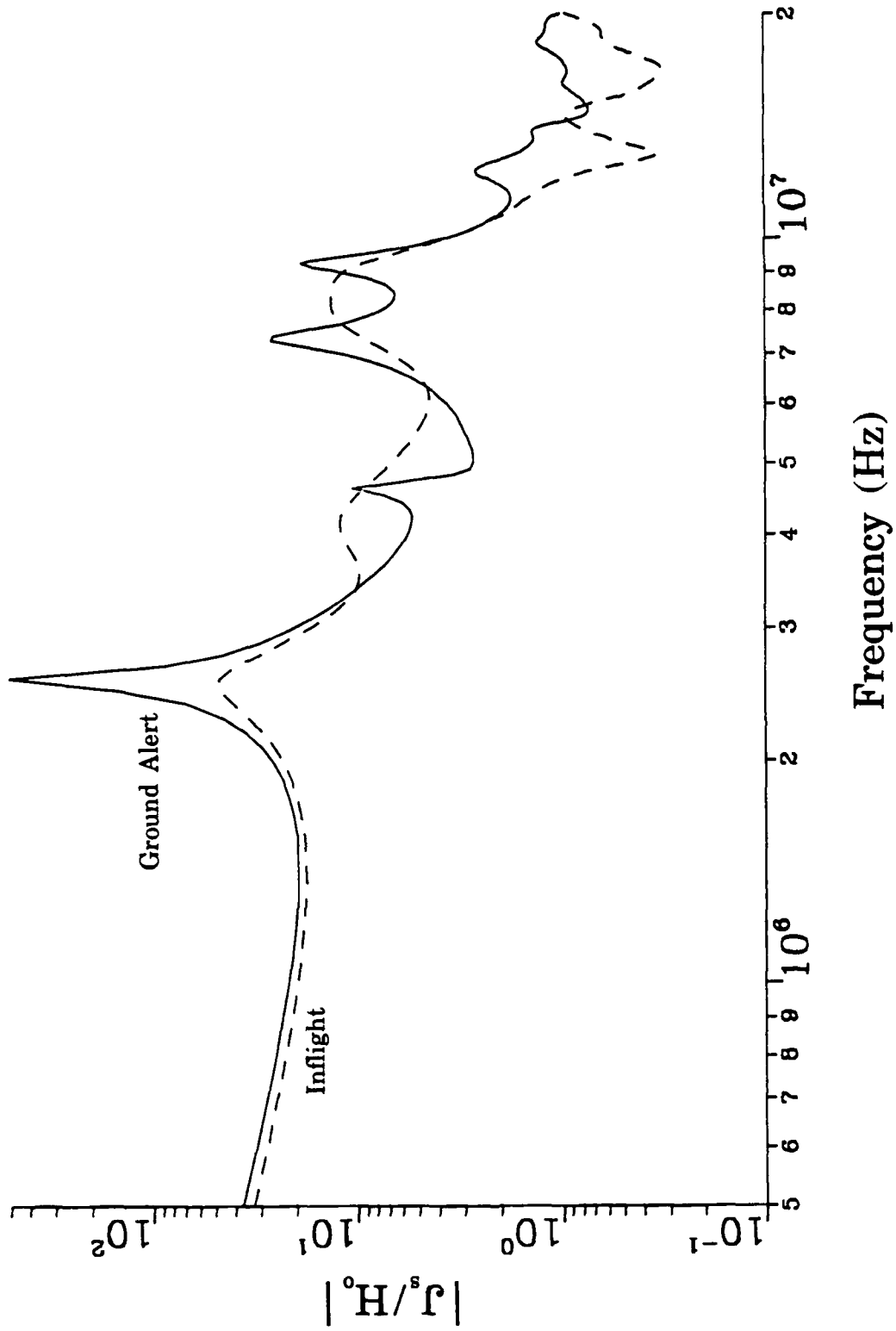


Figure 37. The EMPTAC normalized current density on the top of the mid fuselage (18.69 m from the wing-fuselage junction) for port wing antenna excitation.

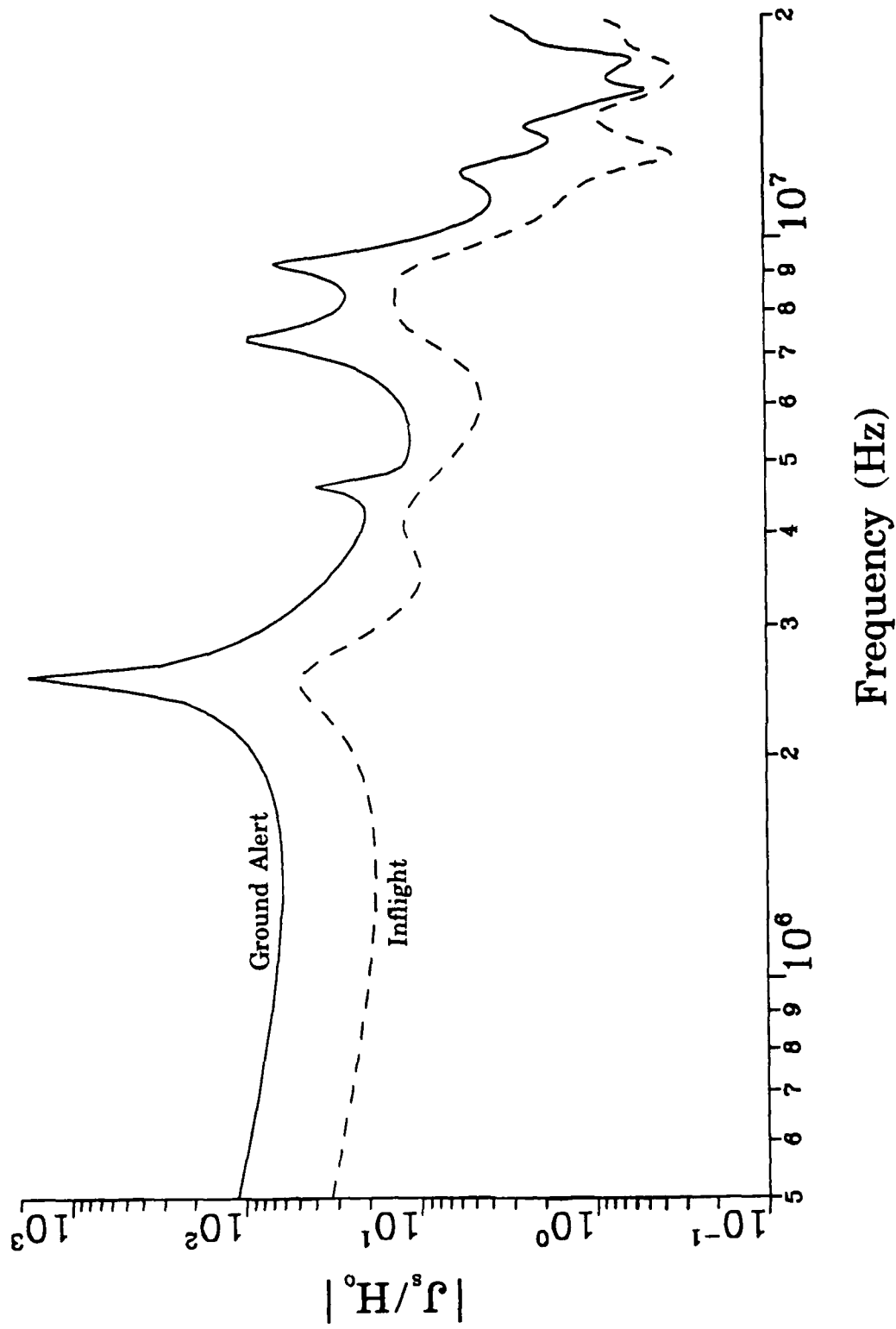


Figure 38. The EMPTAC normalized current density on the bottom of the mid fuselage (18.69 m from the wing-fuselage junction) for port wing antenna excitation.

current density on the top and bottom of the mid fuselage (test points #3 and #4, respectively). Figures 39 and 40 represent the normalized current density at points on the top of the port wing (test points #5 and #6, respectively). Figures 41 and 42 represent the normalized current density at points on the top of the starboard wing (test points #7 and #8, respectively). Figures 43 and 44 represent the normalized charge density on the nose and the tip of the vertical stabilizer (test points #9 and #10, respectively). Figure 45 represents the normalized charge density on the tip of the starboard wing (test point #12).

#### 3.2.4 Response of the EMPTAC to Excitation of the Port and Starboard Wing Antennas (0.5 to 20 MHz)

The normalized responses of the EMPTAC to simultaneous excitation of the port and starboard wing antennas are shown in Figures 46 through 53. Figures 46 and 47 represent the normalized current density on the top and bottom of the front fuselage (test points #1 and #2, respectively). Figures 48 and 49 represent the normalized current density on the top and bottom of the mid fuselage (test points #3 and #4, respectively). Figures 50 and 51 represent the normalized current density at points on the top of the port wing (test points #5 and #6, respectively). Figures 52 and 53 represent the normalized charge density on the nose and the tip of the vertical stabilizer (test points #9 and #10, respectively). The starboard wing responses (test points #7, #8 and #12) predicted by the method-of-moments solution are identical to the corresponding points on the port wing.

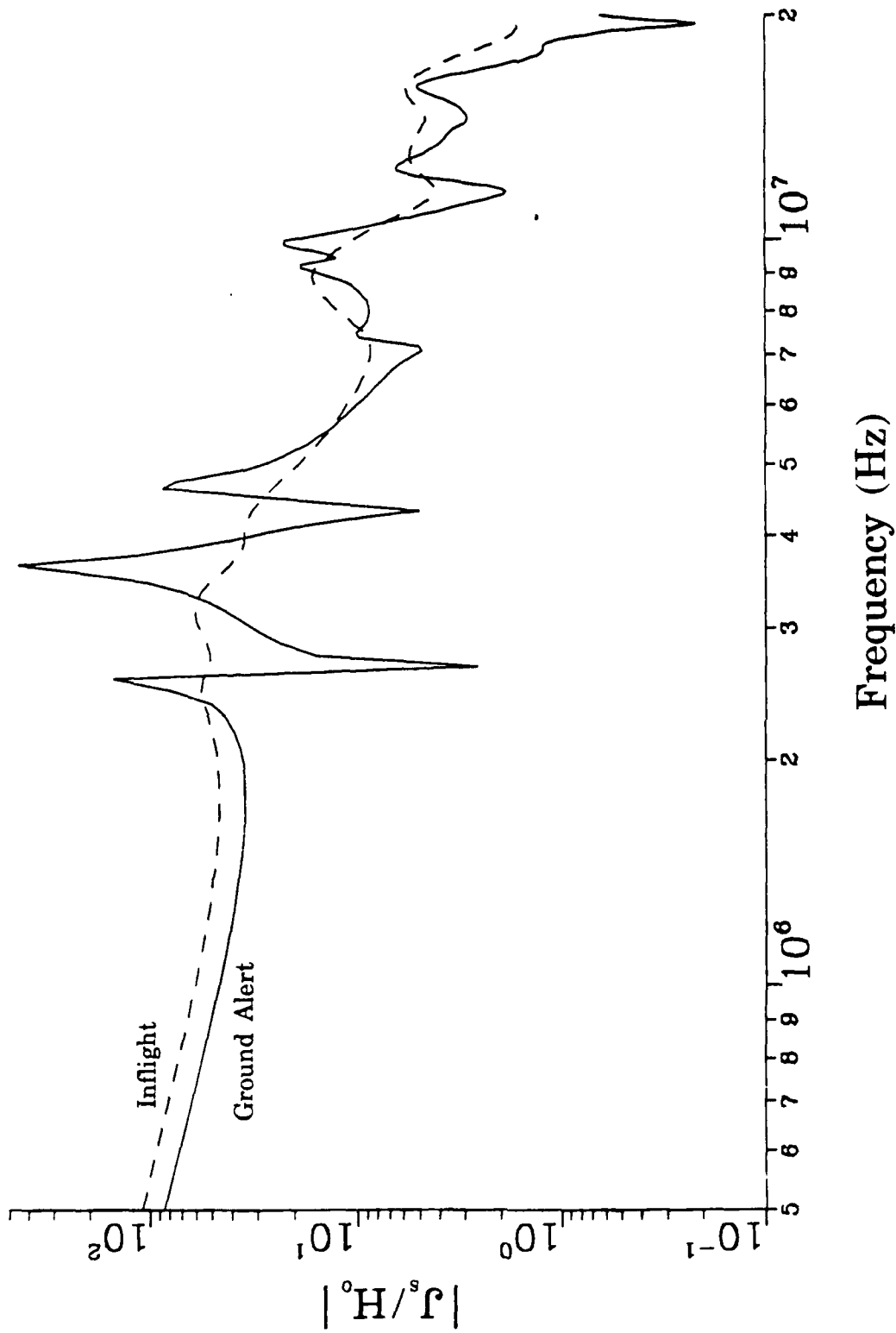


Figure 39. The EMPTAC normalized current density on the top of the port wing (3.9 m from the wing-fuselage junction) for port wing antenna excitation.

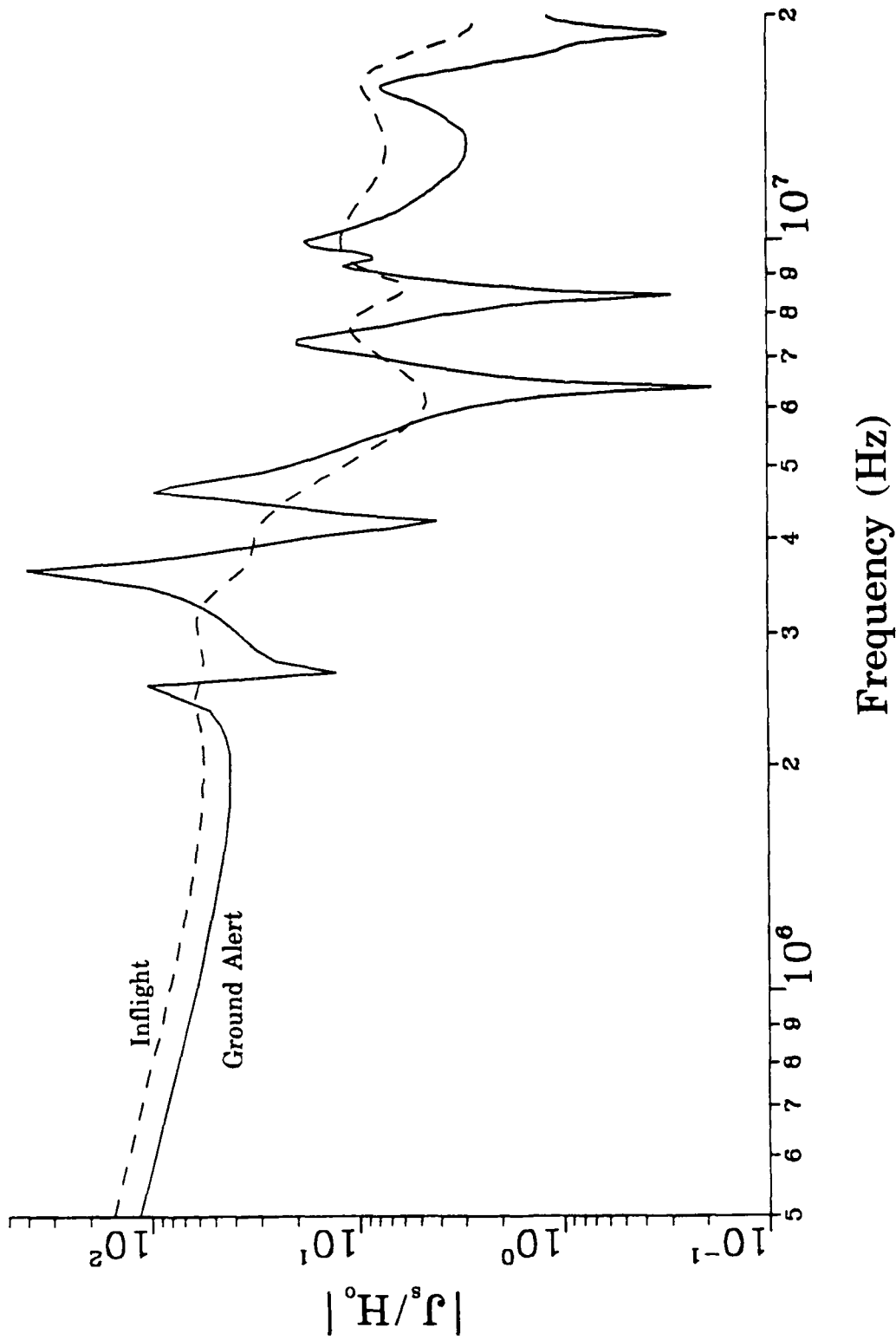


Figure 40. The EMPTAC normalized current density on the top of the port wing (11.7 m from the wing-fuselage junction) for port wing antenna excitation.

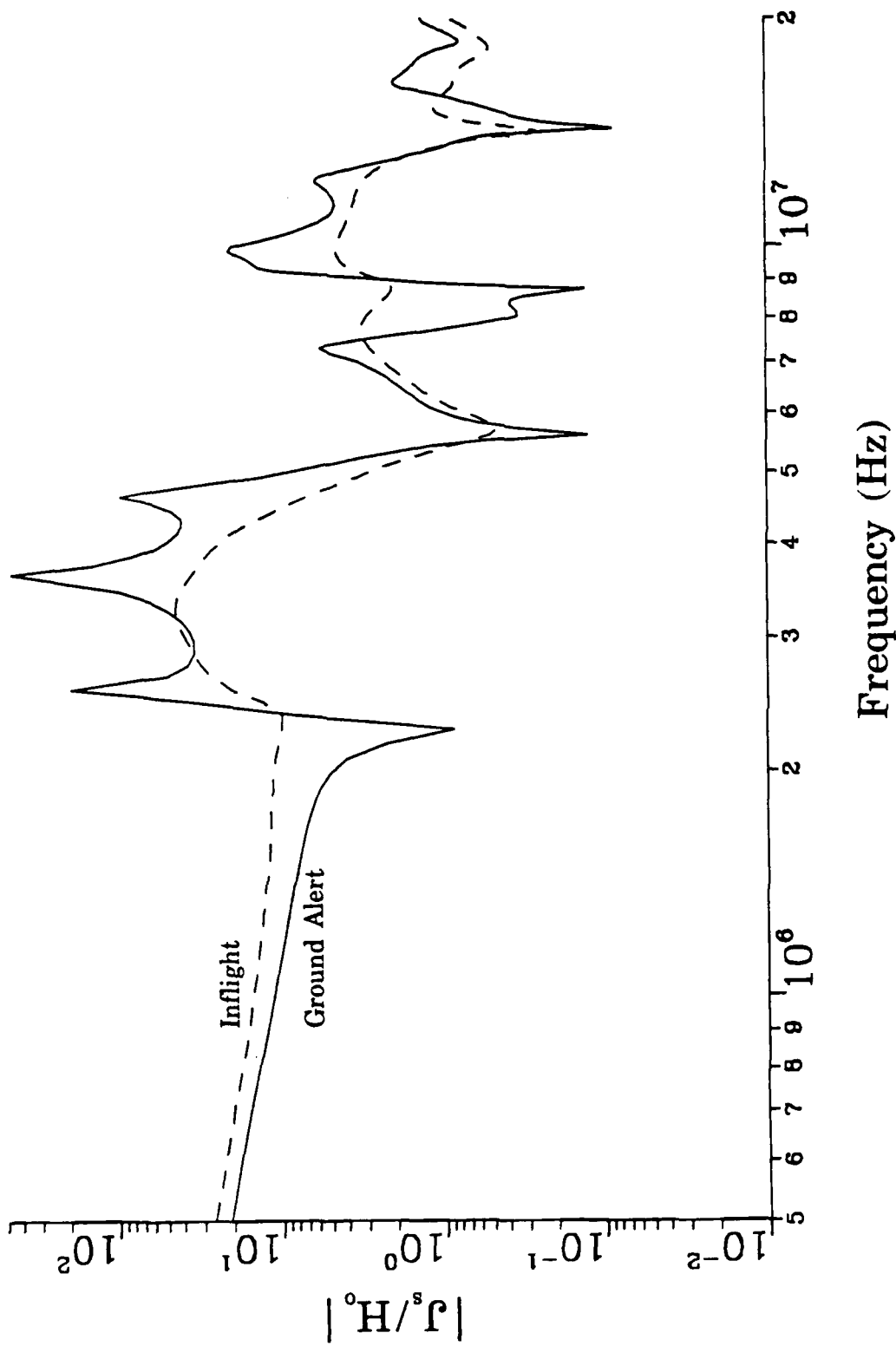


Figure 41. The EMPTAC normalized current density on the top of the starboard wing (3.9 m from the wing-fuselage junction) for port wing antenna excitation.

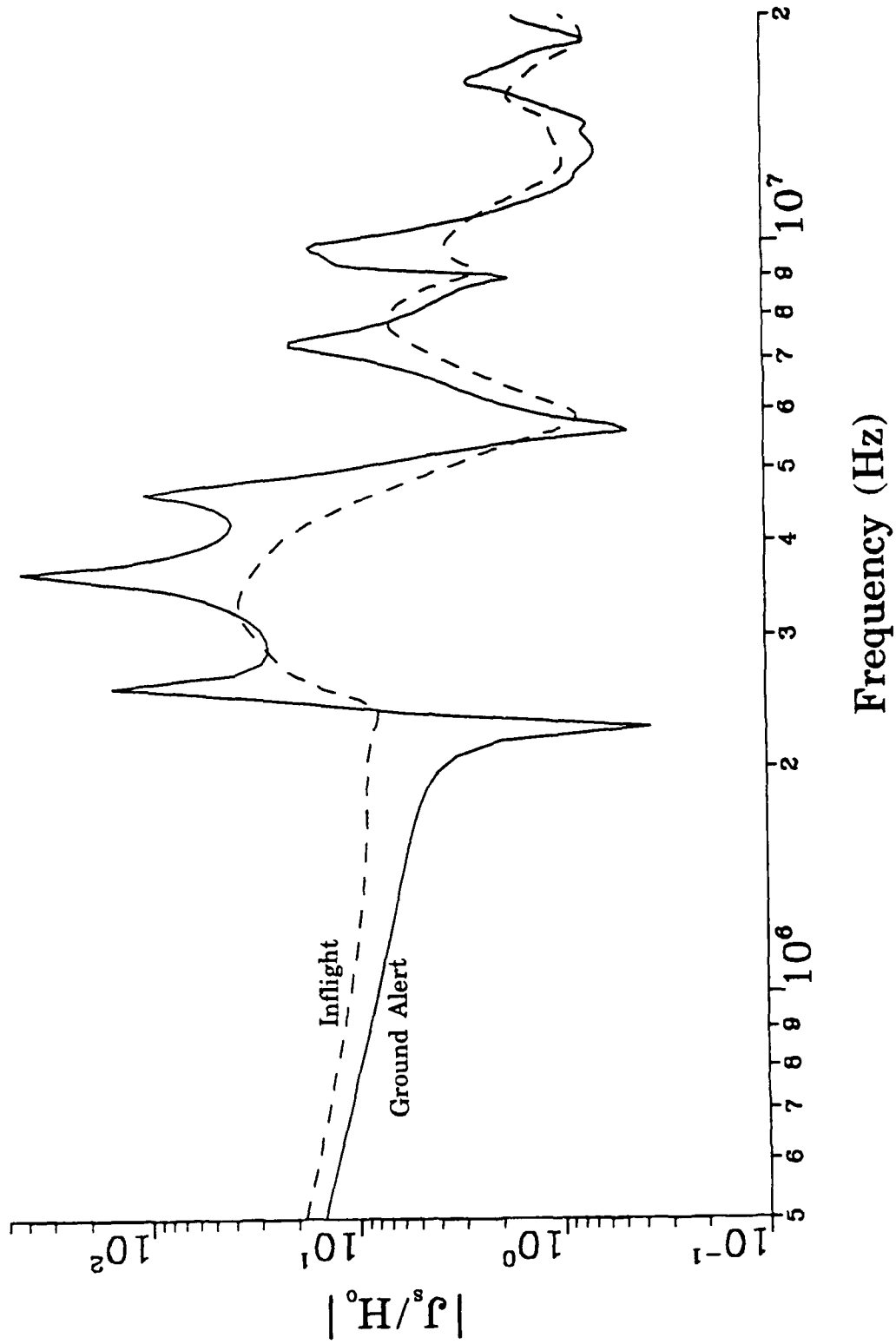


Figure 42. The EMPTAC normalized current density on the top of the starboard wing (11.7 m from the wing-fuselage junction) for port wing antenna excitation.

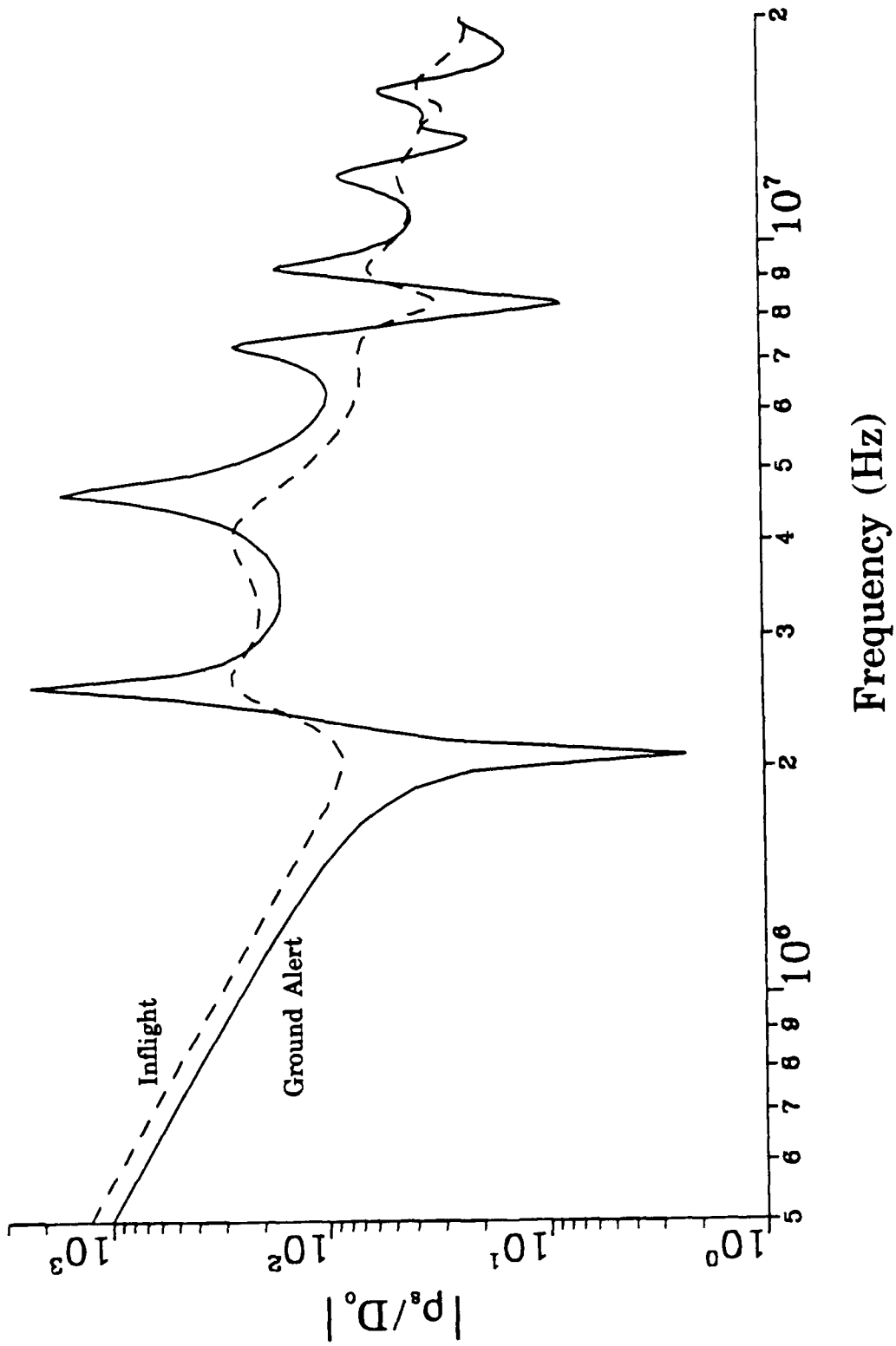


Figure 43. The EMPTAC normalized charge density on the tip of the nose for port wing antenna excitation.

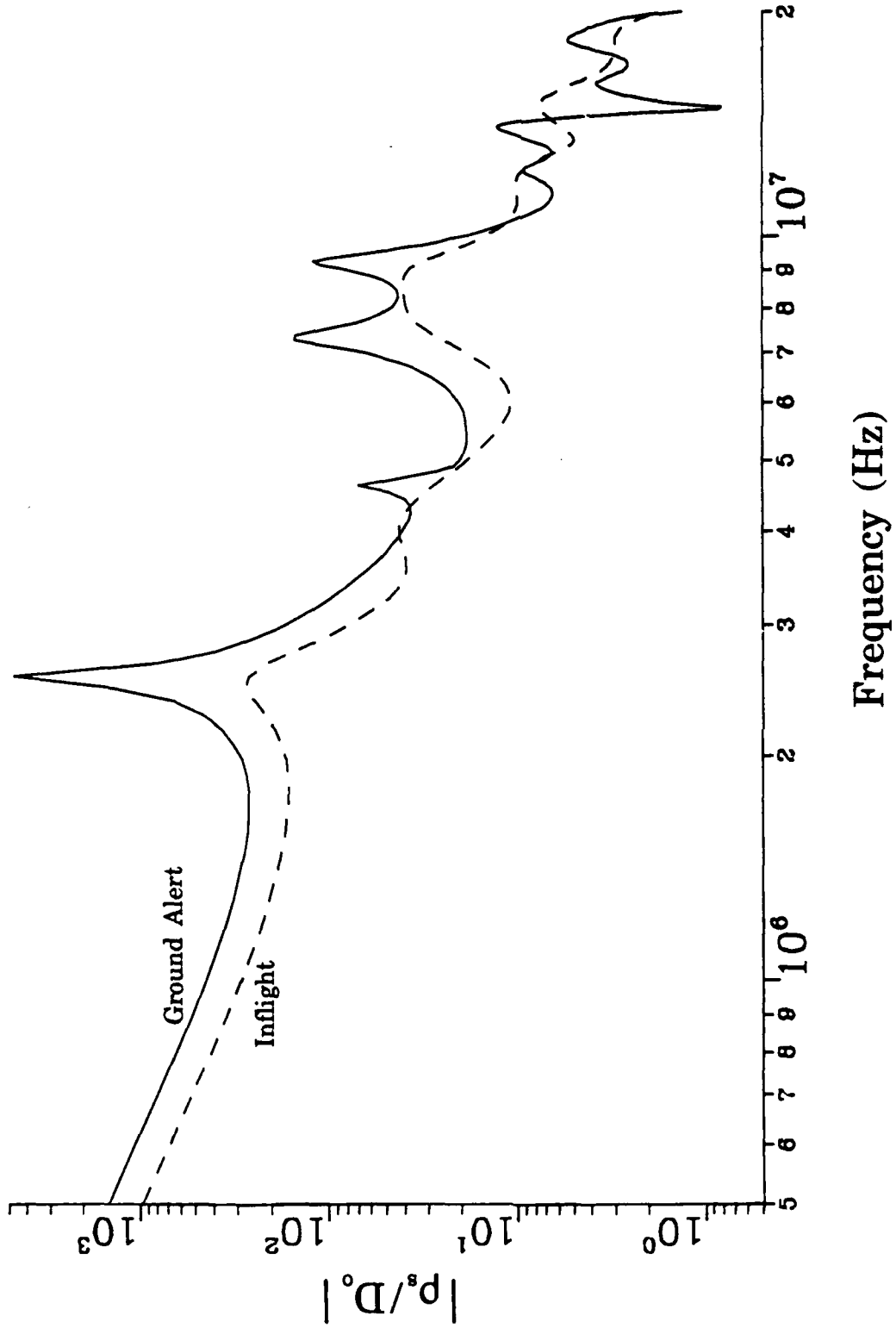


Figure 44. The EMPTAC normalized charge density on the tip of the vertical stabilizer for port wing antenna excitation.

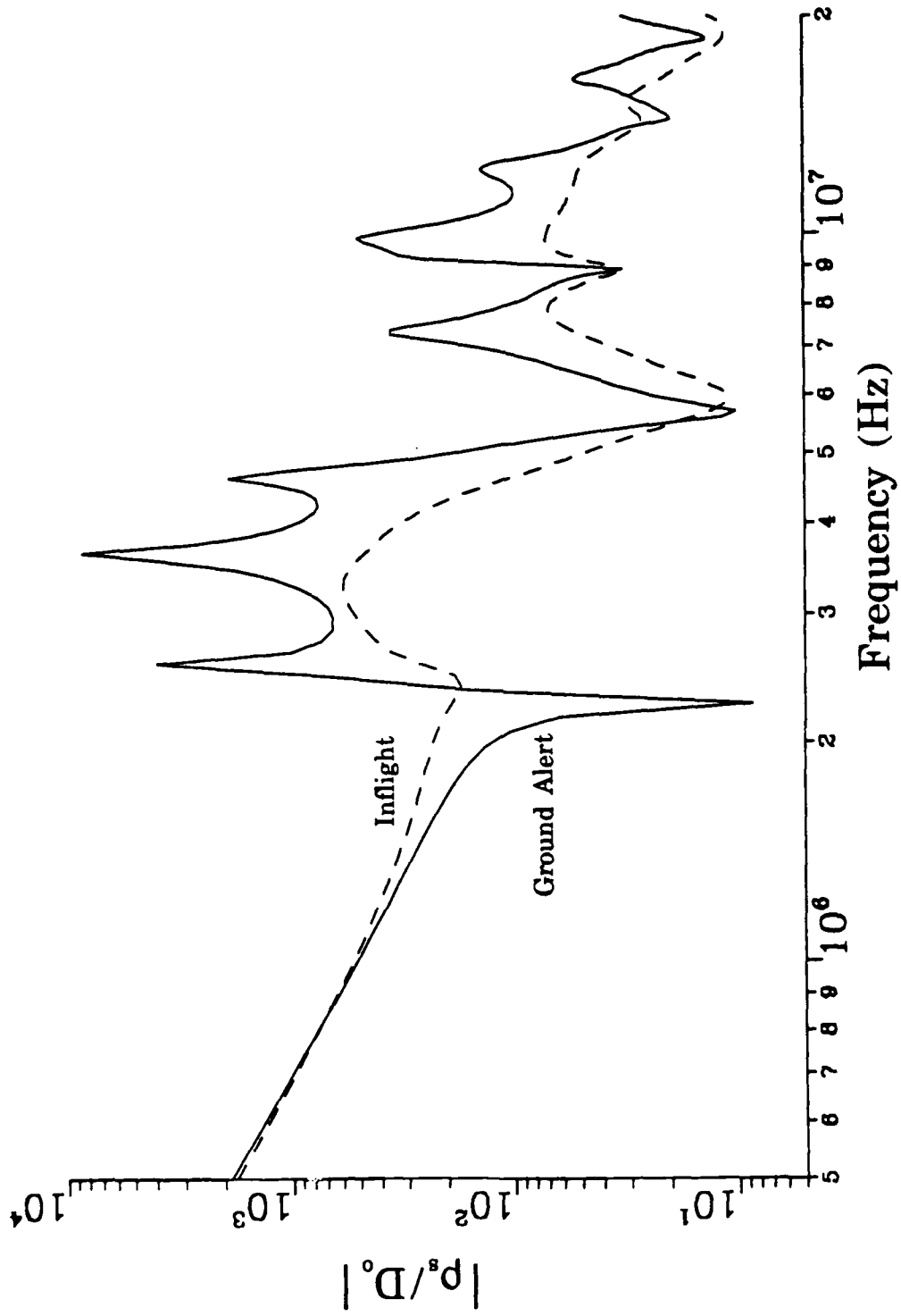


Figure 45. The EMPTAC normalized charge density on the tip of the starboard wing for port wing antenna excitation.

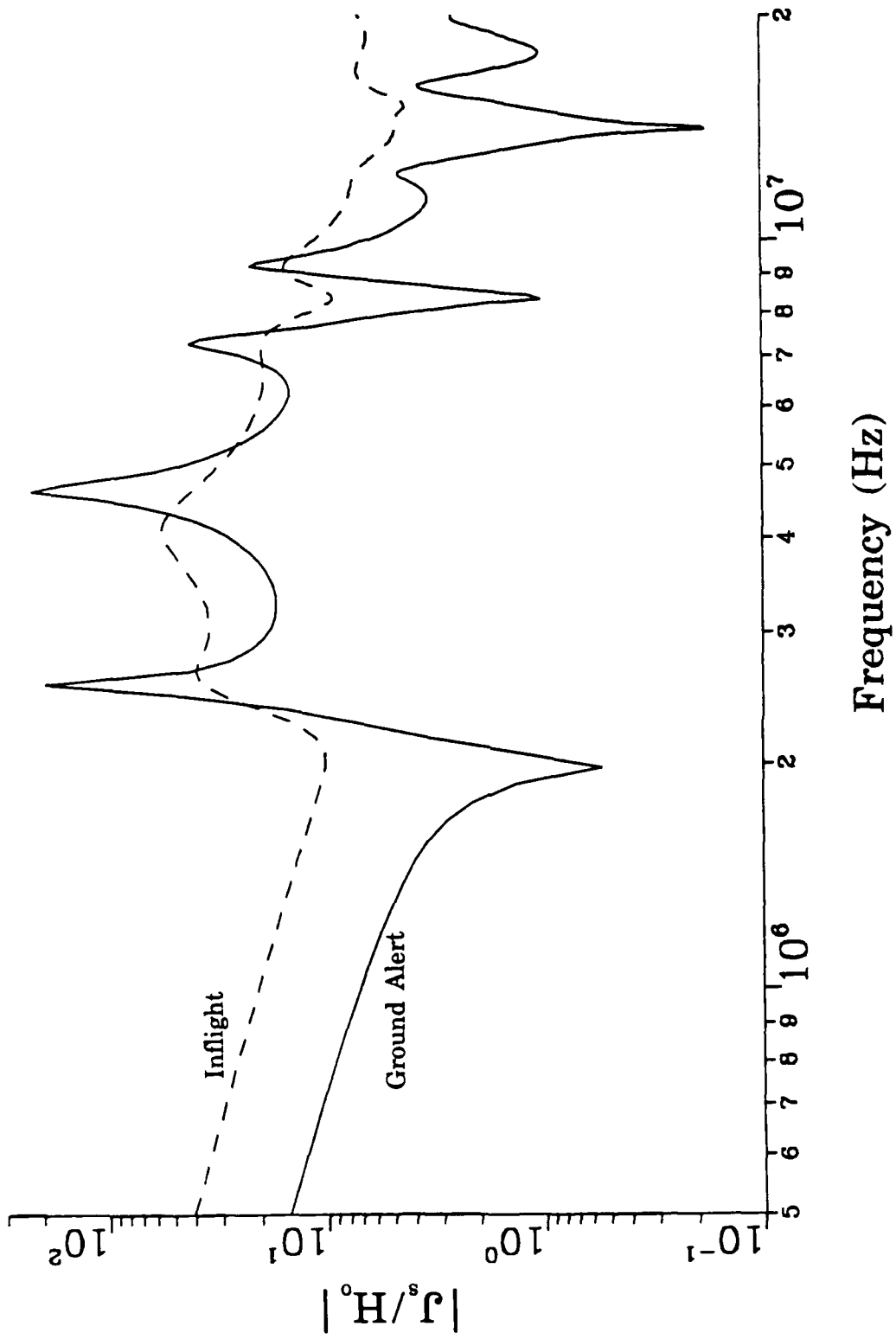


Figure 46. The EMPTAC normalized current density on the top of the front fuselage (10.29 m from the nose) for port and starboard wing antenna excitation.

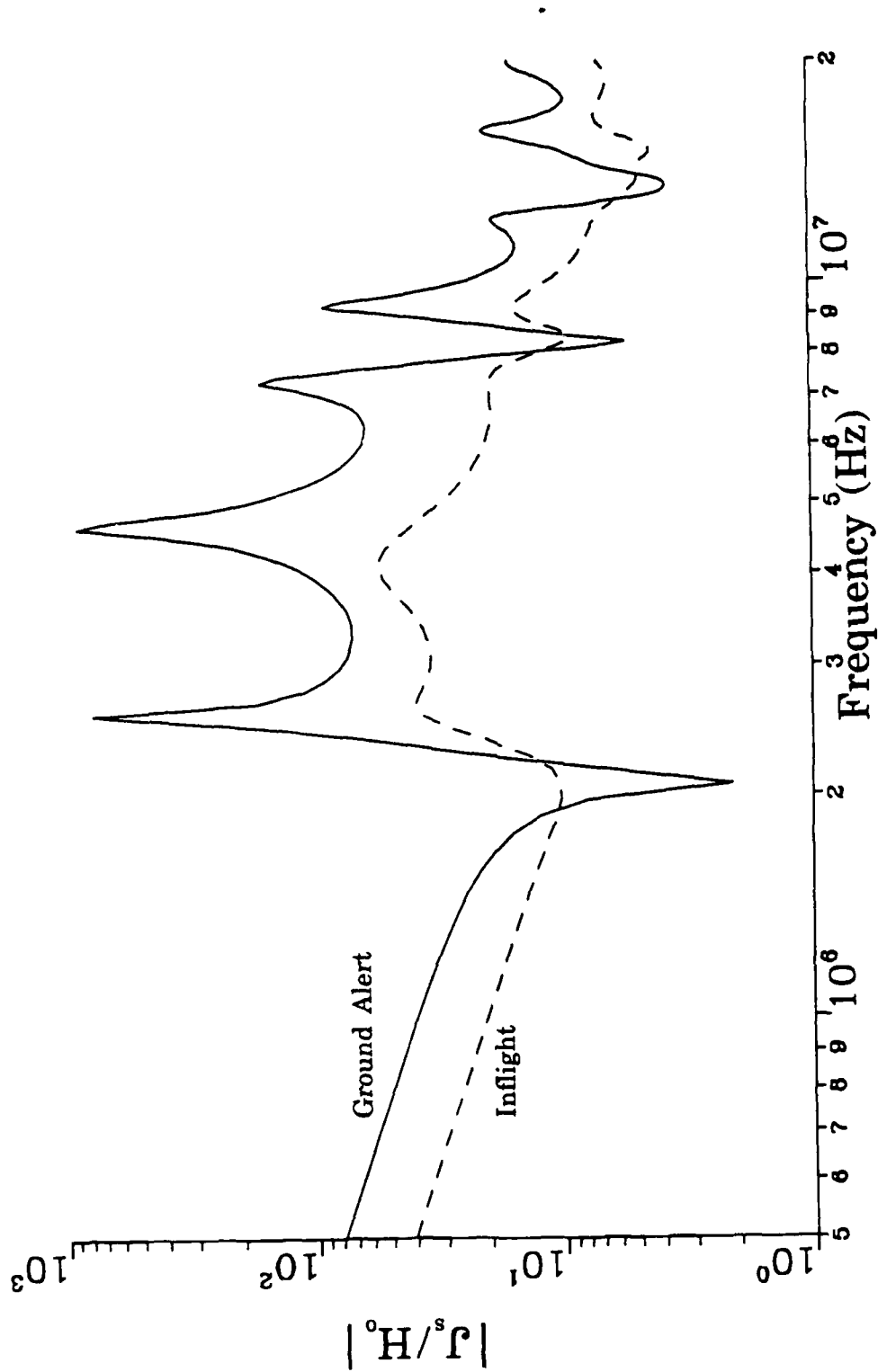


Figure 47. The EMPTAC normalized current density on the bottom of the front fuselage (10.29 m from the nose) for starboard and port wing antenna excitation.

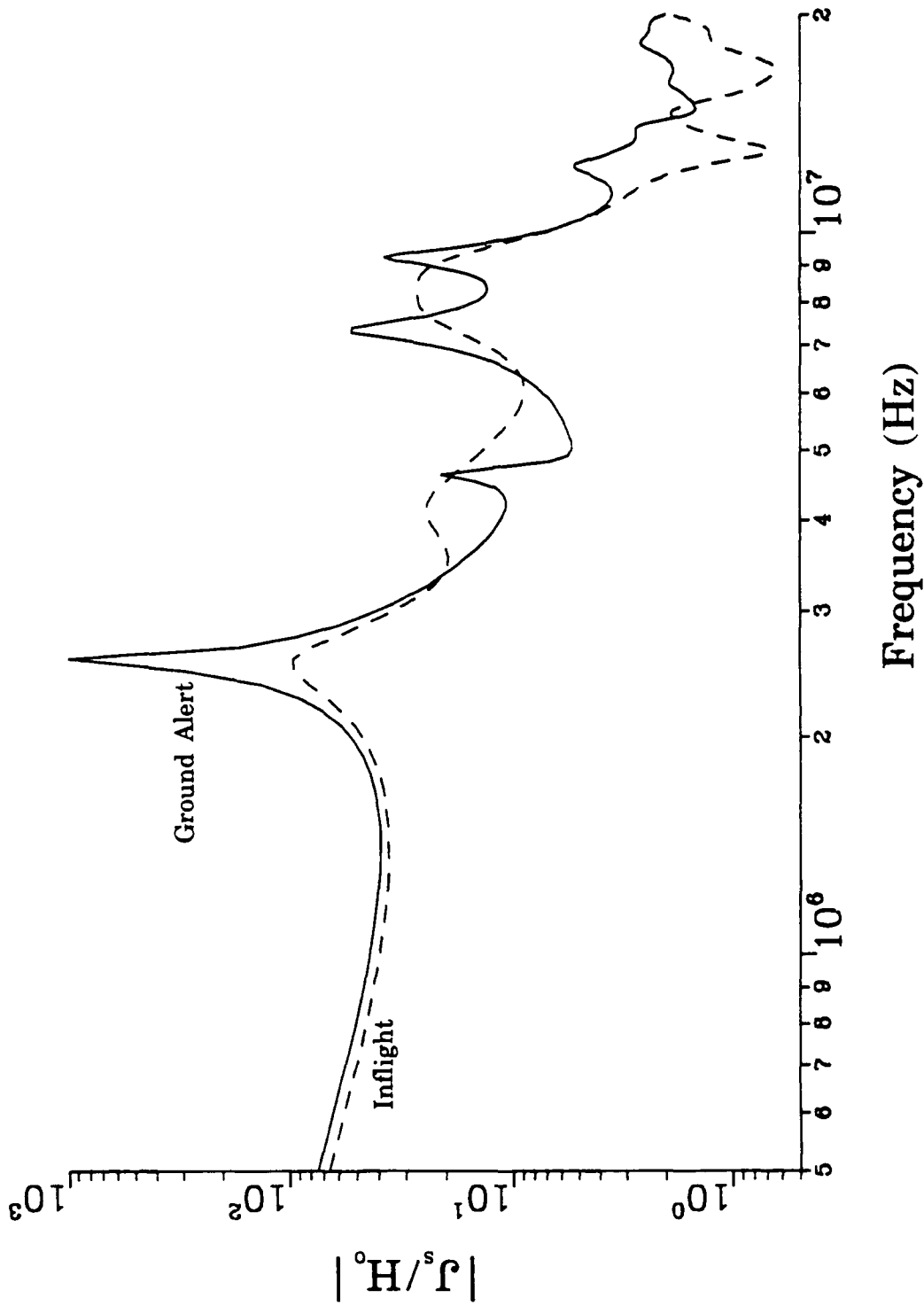


Figure 48. The EMPTAC normalized current density on the top of the mid fuselage (18.69 m from the wing-fuselage junction) for port and starboard wing antenna excitation.

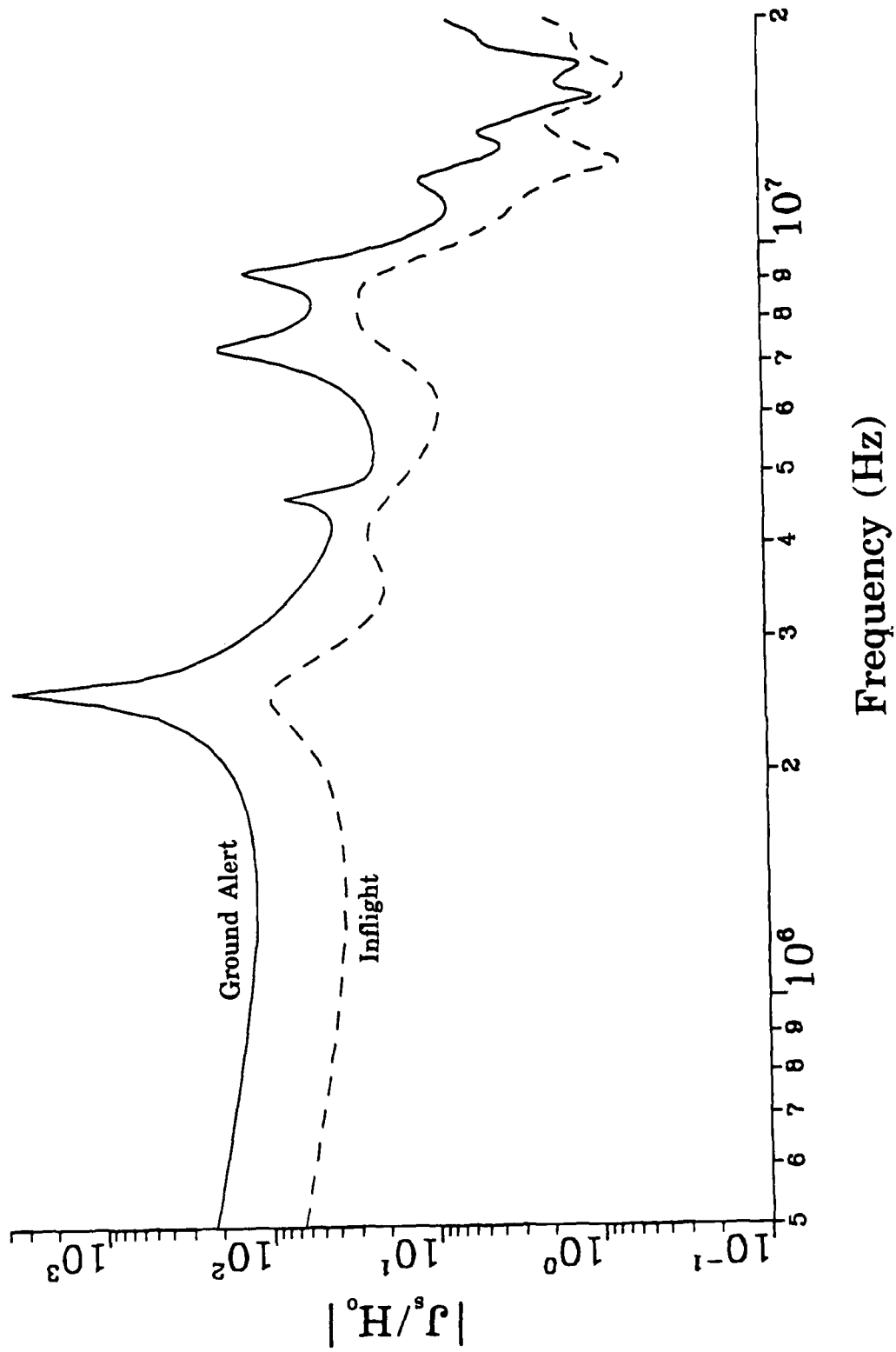


Figure 49. The EMPTAC normalized current density on the bottom of the mid fuselage (18.69 m from the wing-fuselage junction) for port and starboard wing antenna excitation.

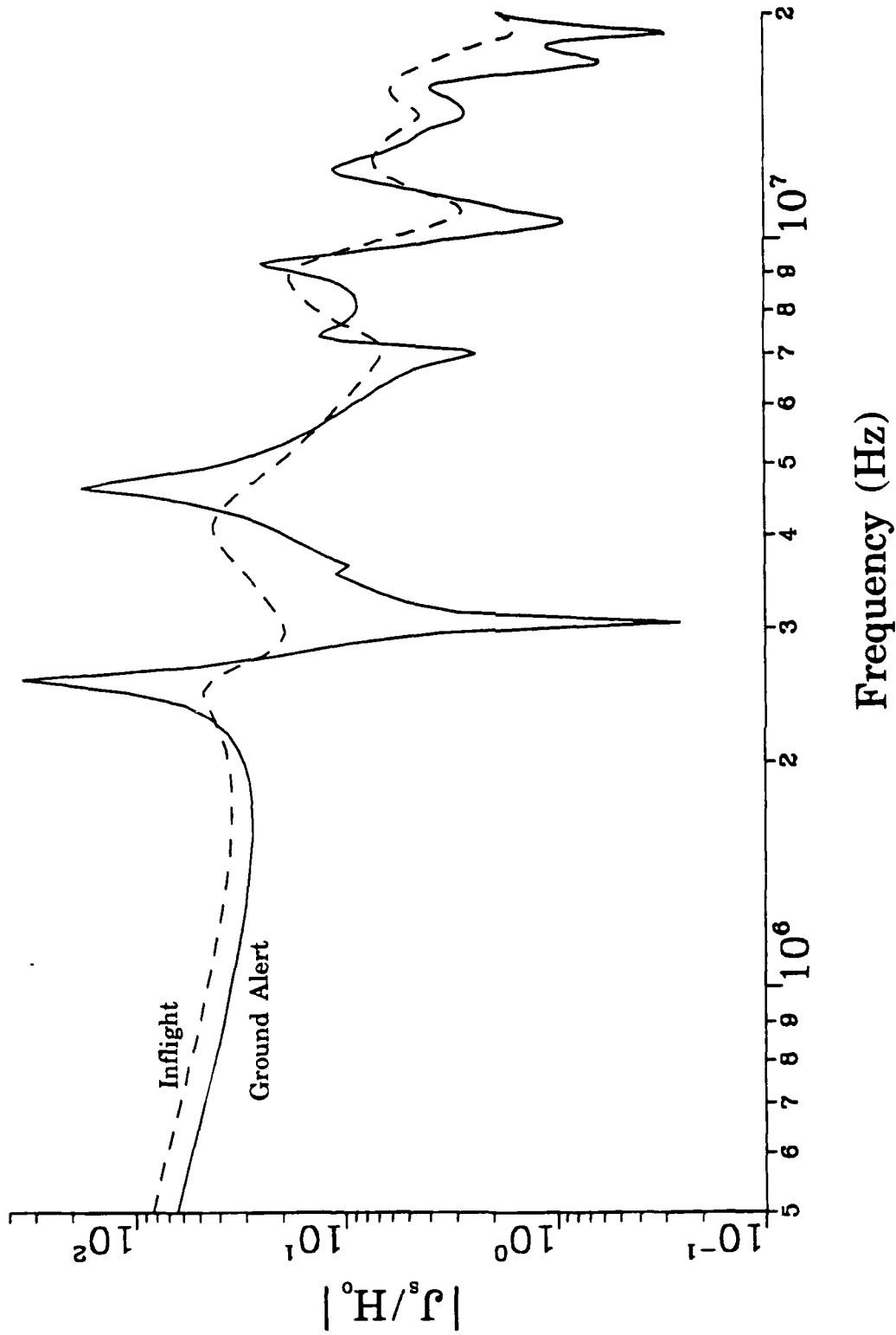


Figure 50. The EMPTAC normalized current density on the top of the port wing (3.9 m from the wing-fuselage junction) for port and starboard wing antenna excitation.

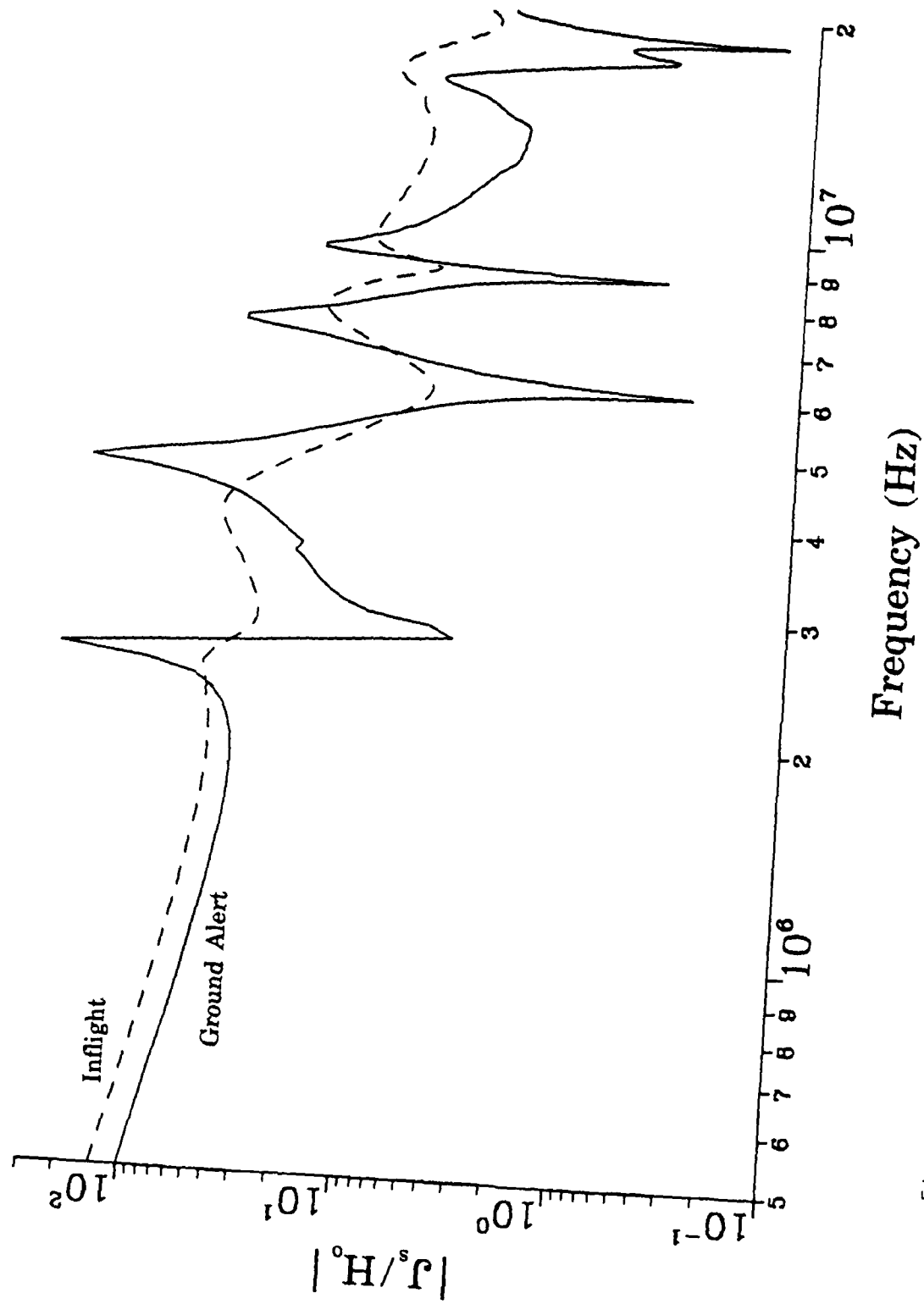


Figure 51. The EMPTAC normalized current density on the top of the port wing (11.7 m from the wing-fuselage junction) for port and starboard wing antenna excitation.

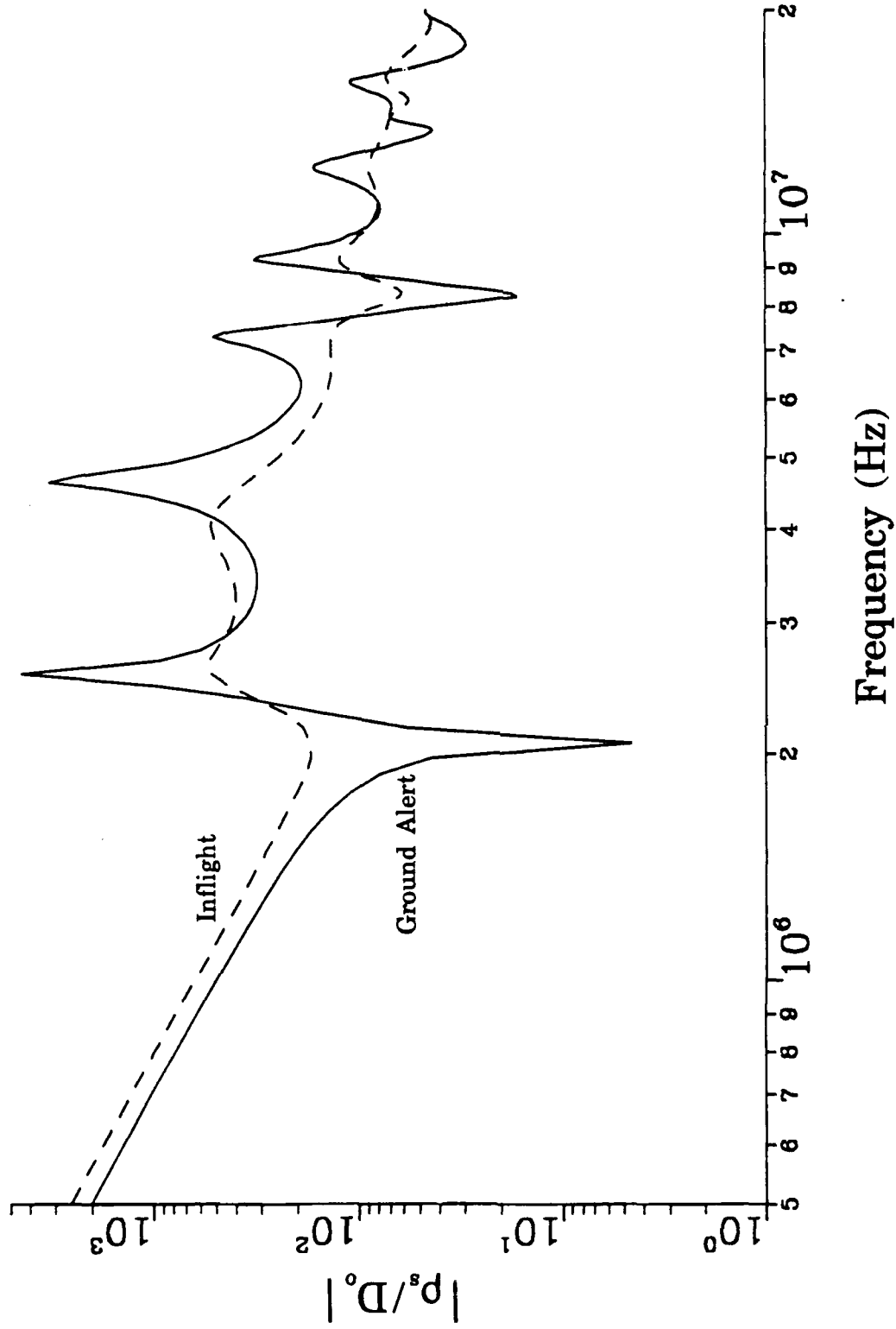


Figure 52. The EMPTAC normalized charge density on the tip of the nose for port and starboard wing antenna excitation.

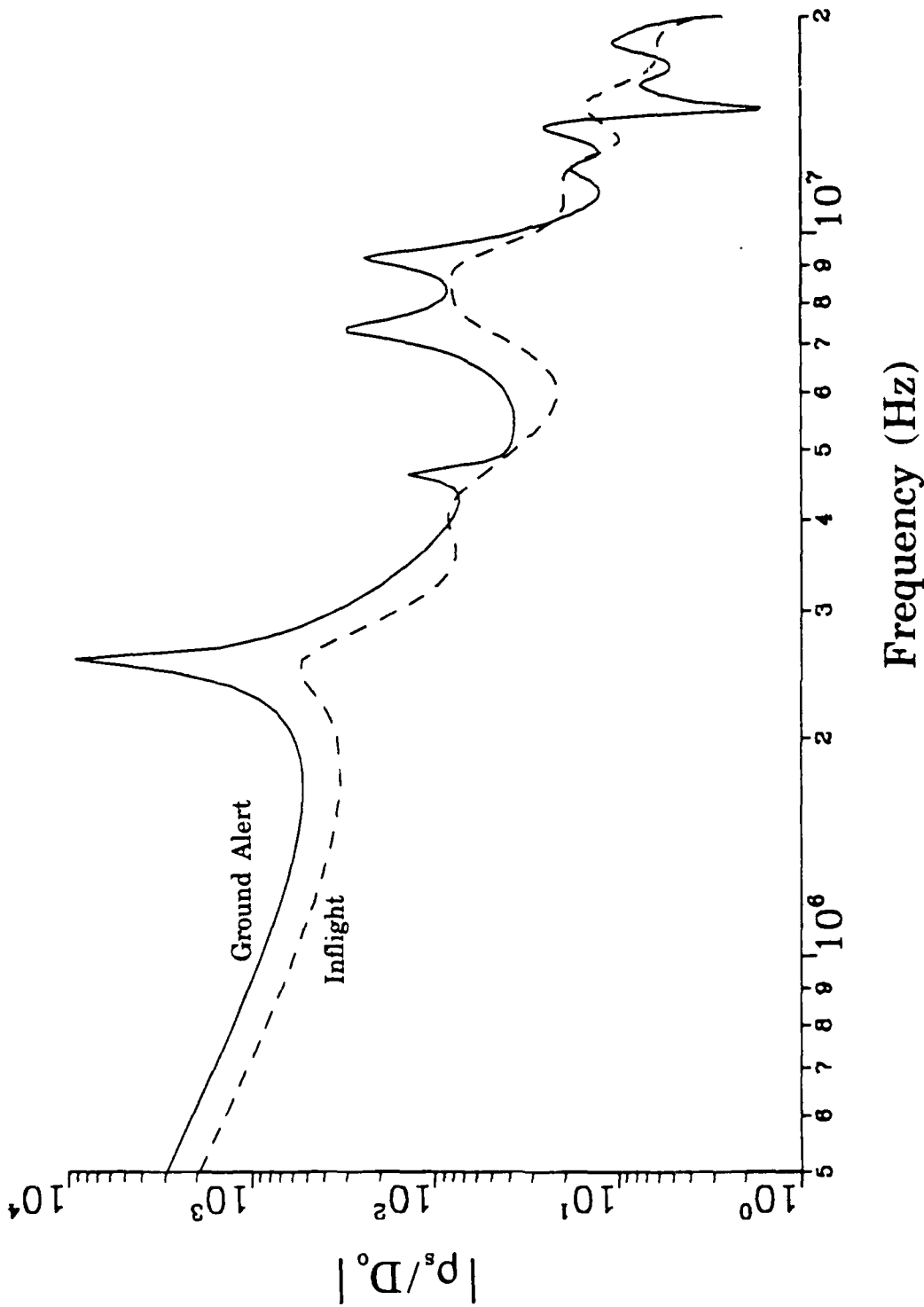


Figure 53. The EMPTAC normalized charge density on the tip of the vertical stabilizer for port and starboard wing antenna excitation.

#### 4.0 EMPTAC RESPONSE USING THE PHYSICAL OPTICS APPROXIMATION

The external responses of the EMPTAC due to plane wave excitation and the excitation via onboard HF antennas are considered in this section for frequencies between 20 and 100 MHz. The surface responses presented are obtained using the physical optics approximation (Ref. 4). Using the physical optics approximation, the surface current density in the inflight mode is given by

$$J_s(s, \phi) \approx 2\hat{\phi} \bar{H}^{in} \quad (17)$$

where  $\hat{\phi}$  represents a unit vector defined in the right hand sense with respect to the direction of positive axial current. In the ground alert mode, the physical optics approximation for the surface current density is given by

$$J_s(s, \phi) \approx 2\hat{\phi} \left[ (\bar{H}^{in} + \bar{H}^{ref}) \right] \quad (18)$$

A comparison of Equation 17 with Equation 5 and Equation 18 with Equation 7 shows that the physical optics approximation is equivalent to neglecting the axial current contribution in the original approximations for the current density.

##### 4.1 RESPONSE OF THE EMPTAC TO PLANE WAVE EXCITATION

The external response of the EMPTAC to the two overhead plane wave polarizations defined in paragraph 3.1 is presented for both the inflight and ground alert modes. Using the physical optics approximations given in Equations 17 and 18, the normalized surface responses between 20 and 100 MHz are simple constants. The normalized EMPTAC surface currents for the two polarizations of the incident plane wave are given in Tables 4 and 5.

Table 4. Normalized EMPTAC surface current densities (20-100 MHz) for plane wave excitation (E || to the fuselage) as predicted by the physical optics approximation.

Test Point #	$J_s/H_o$ Inflight	$J_s/H_o$ Ground Alert
1	2.000	4.000
2	2.000	4.000
3	2.000	4.000
4	2.000	4.000
5	1.089	2.178
6	1.089	2.178
7	1.089	2.178
8	1.089	2.178

Table 5. Normalized EMPTAC surface current densities (20 to 100 MHz) for plane wave excitation ( $E \perp$  to the fuselage) as predicted by the physical optics approximation.

Test Point #	$J_s/H_o$ Inflight	$J_s/H_o$ Ground Alert
1	0.000	0.000
2	0.000	0.000
3	0.000	0.000
4	0.000	0.000
5	1.677	3.355
6	1.677	3.355
7	1.677	3.355
8	1.677	3.355

#### 4.2 RESPONSE OF THE EMPTAC TO VARIOUS DRIVE CONFIGURATIONS OF THE ONBOARD HF ANTENNAS

The responses of the EMPTAC to the four HF antenna drive configurations discussed in paragraph 3.2 are presented. The physical optics approximation is used to determine results for both the inflight and ground alert modes from 20 to 100 MHz. The average power radiated by each active antenna ( $P_{rad}$ ) is again assumed to be a constant 10 W over the frequency range of interest.

##### 4.2.1 Response of the EMPTAC to Excitation of The Fin-Cap Antenna (20 to 100 MHz)

The normalized responses of the EMPTAC to excitation of the fin-cap antenna are shown in Figures 54 through 59. Figures 54 and 55 represent the normalized current density on the top and bottom of the front fuselage (test points #1 and #2, respectively). Figures 56 and 57 represent the normalized current density on the top and bottom of the mid fuselage (test points #3 and #4, respectively). Figures 58 and 59 represent the normalized current density at points on the top of the port wing (test points #5 and #6, respectively). The starboard wing responses (test points #7 and #8) predicted by the method-of-moments solution are identical to those of the port wing.

##### 4.2.2 Response of the EMPTAC to Excitation of the Nose and Fin-Cap Antennas (20 to 100 MHz)

The normalized responses of the EMPTAC to simultaneous excitation of the nose and fin-cap antennas are shown in Figures 60 and 61. Figures 60 and 61 represent the normalized current density on the top and bottom of the front fuselage (test points #1 and #2, respectively). Figures 62 and 63 represent the normalized current density on the top and bottom of the mid fuselage (test points #3 and #4, respectively). Figures 64 and 65 represent the normalized current density at points on the top of the port wing (test points #5 and #6, respectively). The starboard wing responses (test points #7 and #8) predicted by the method-of-moments solution are identical to those of the port wing.

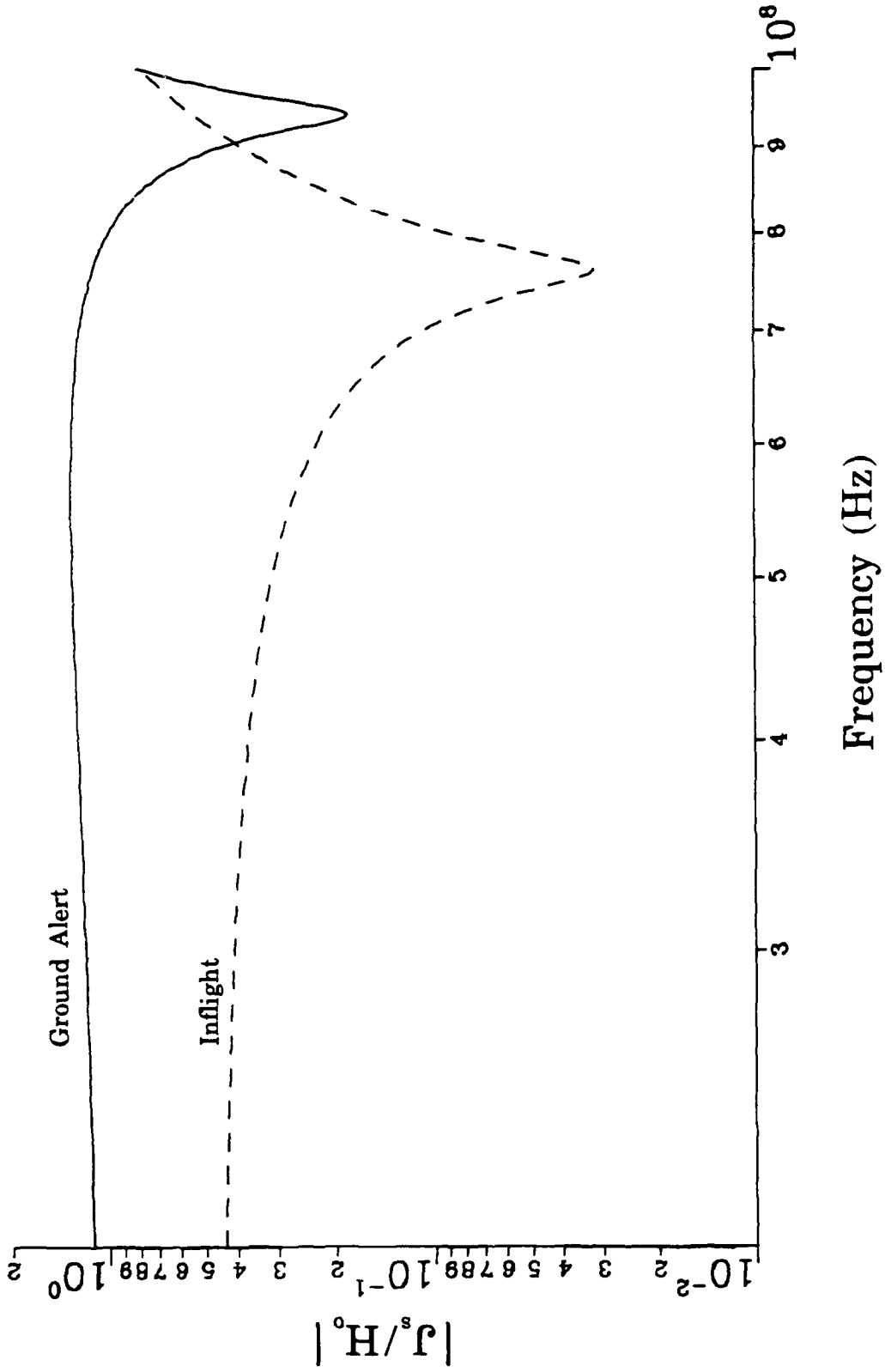


Figure 54. The EMPTAC normalized current density on the top of the front fuselage (10.29 m from the nose) for fin-cap antenna excitation (physical optics approximation).

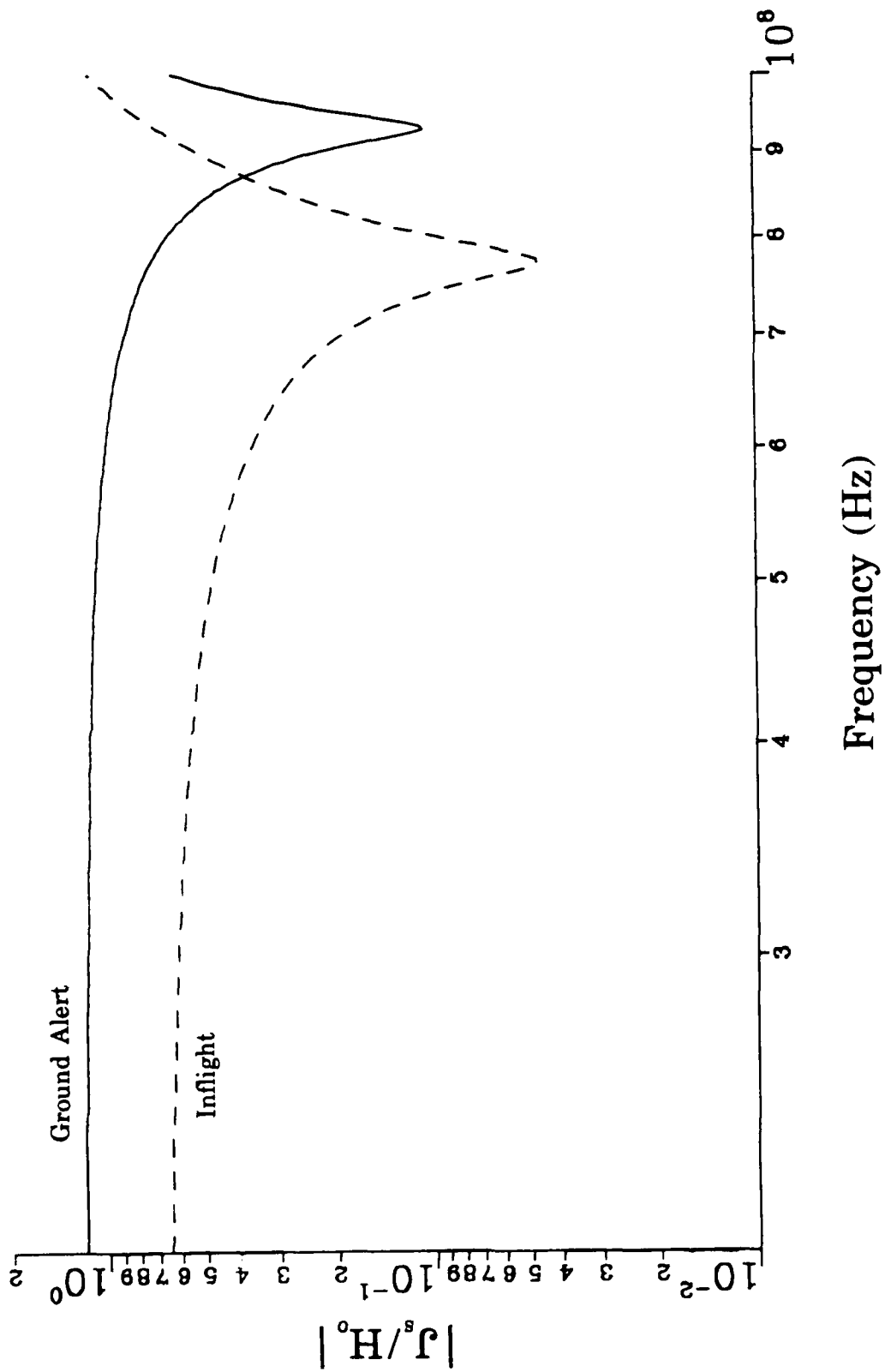


Figure 55. The EMPTAC normalized current density on the bottom of the front fuselage (10.29 m from the nose) for fin-cap antenna excitation (physical optics approximation).

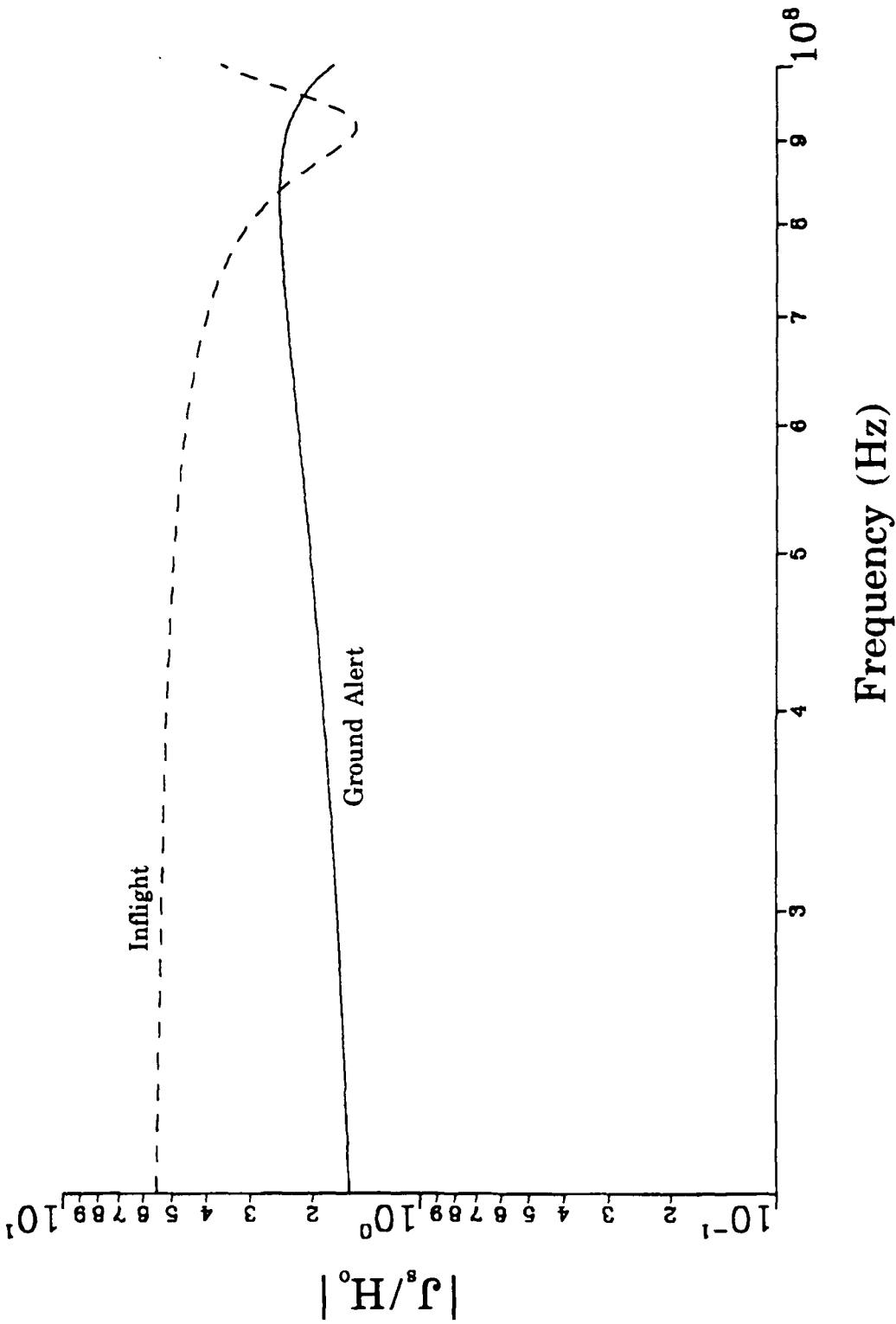


Figure 56. The EMPTAC normalized current density on the top of the mid fuselage (18.69 m from the wing-fuselage junction) for fin-cap antenna excitation (physical optics approximation).

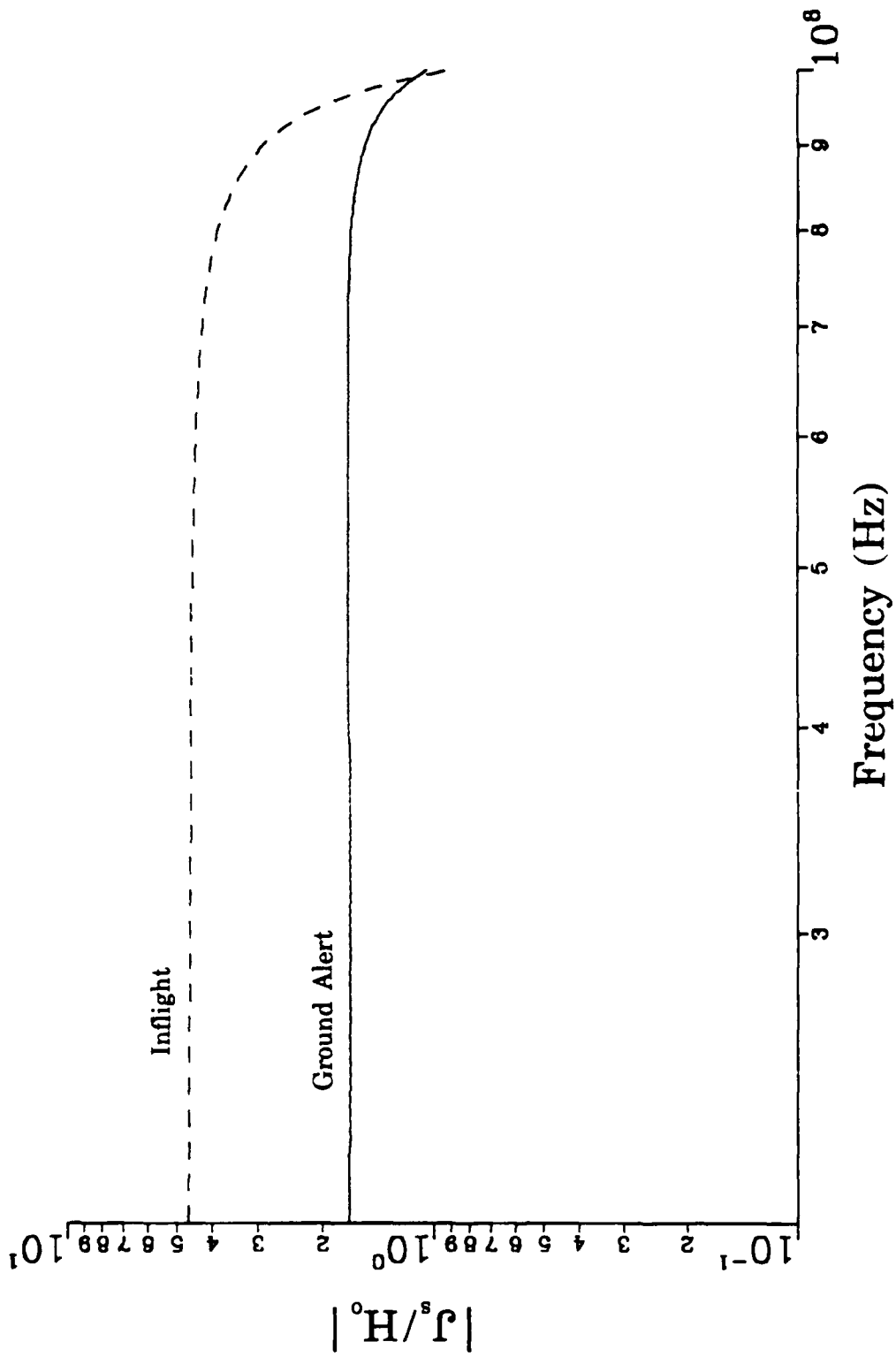


Figure 57. The EMPTAC normalized current density on the bottom of the mid fuselage (18.69 m from the wing-fuselage junction) for fin-cap antenna excitation (physical optics approximation).

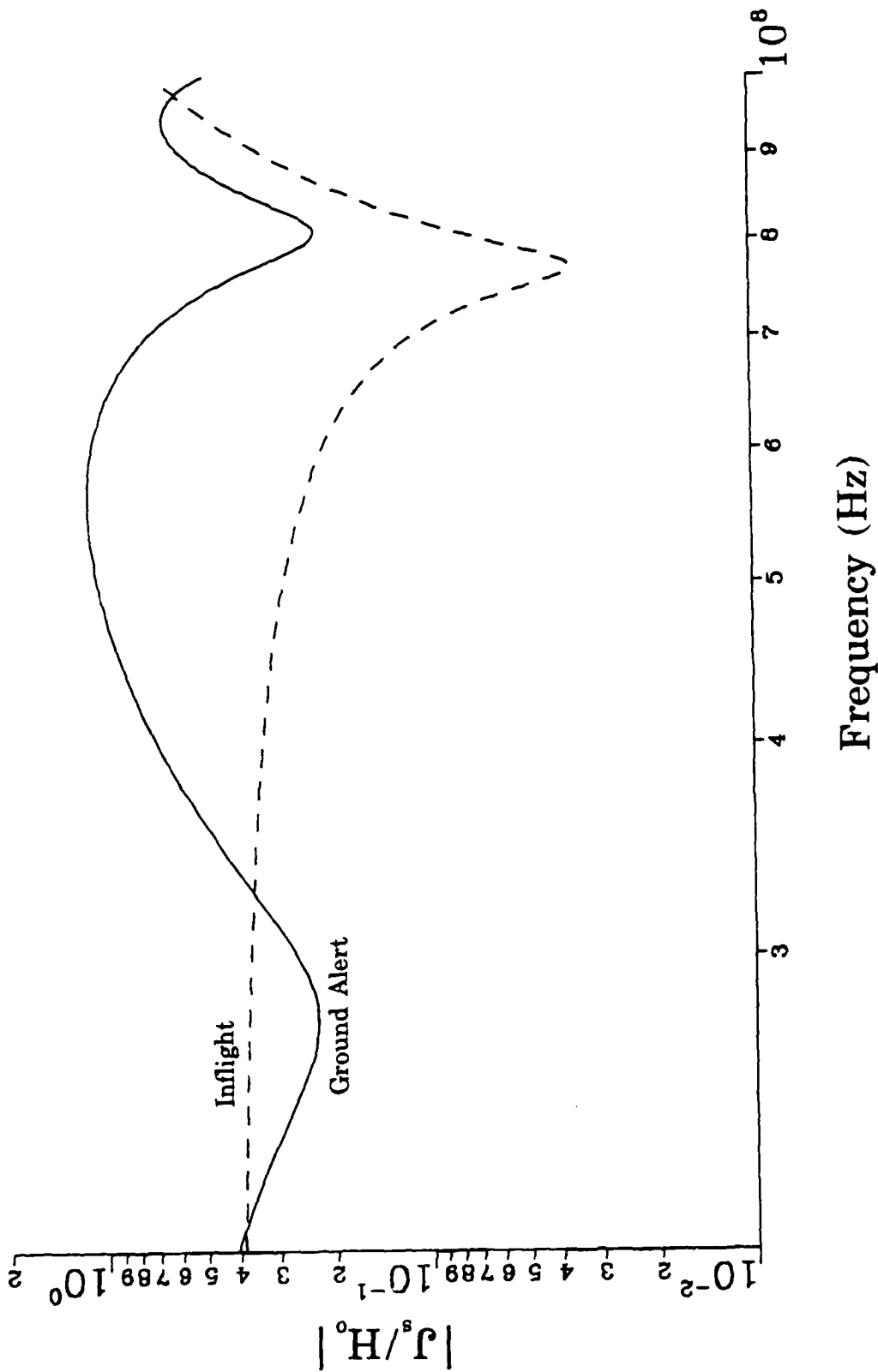


Figure 58. The EMPTAC normalized current density on the top of the port wing (3.9 m from the wing-fuselage junction) for fin-cap antenna excitation (physical optics approximation).

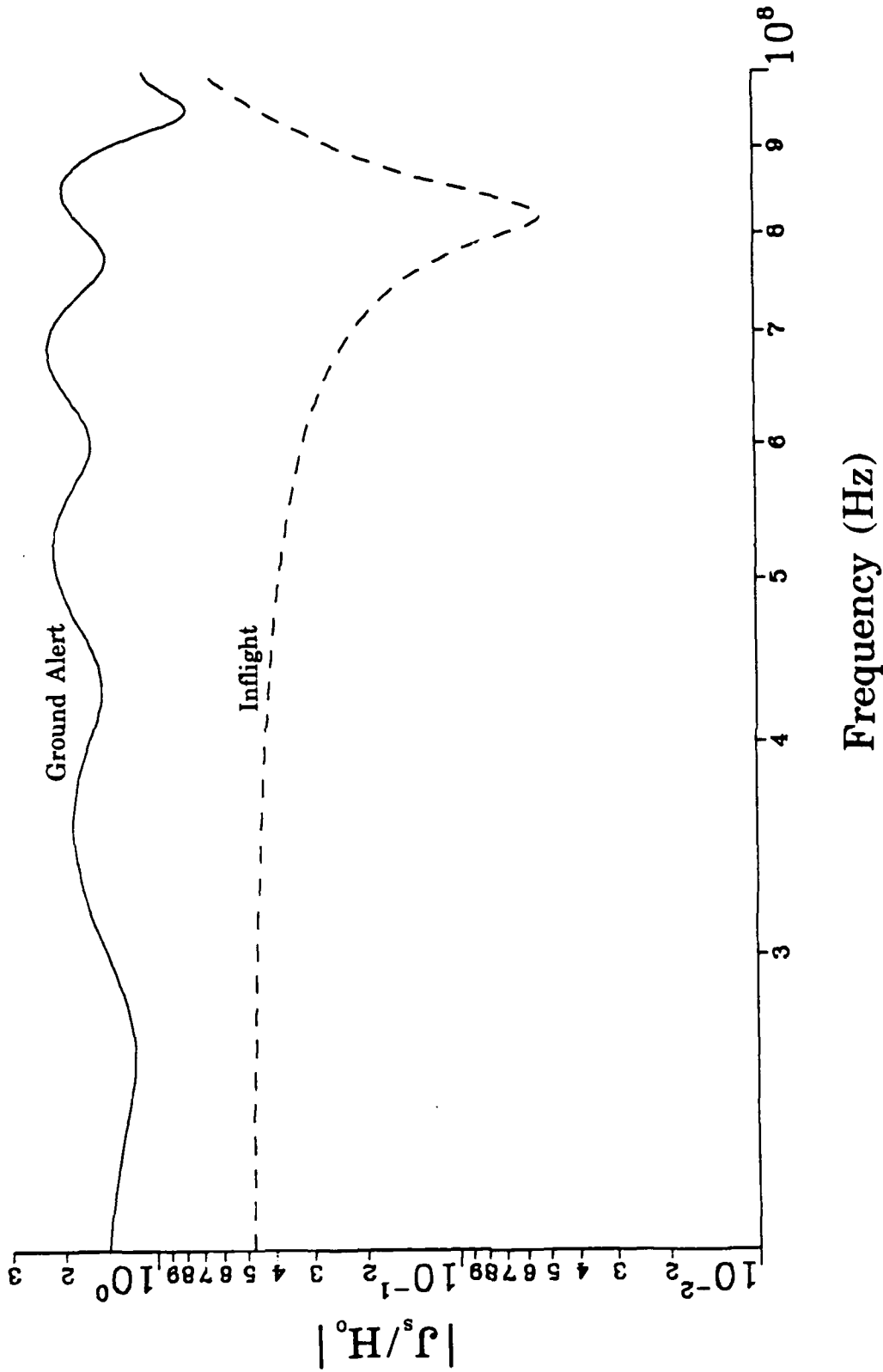


Figure 59. The EMPTAC normalized current density on the top of the port wing (11.7 m from the wing-fuselage junction) for fin-cap antenna excitation (physical optics approximation).

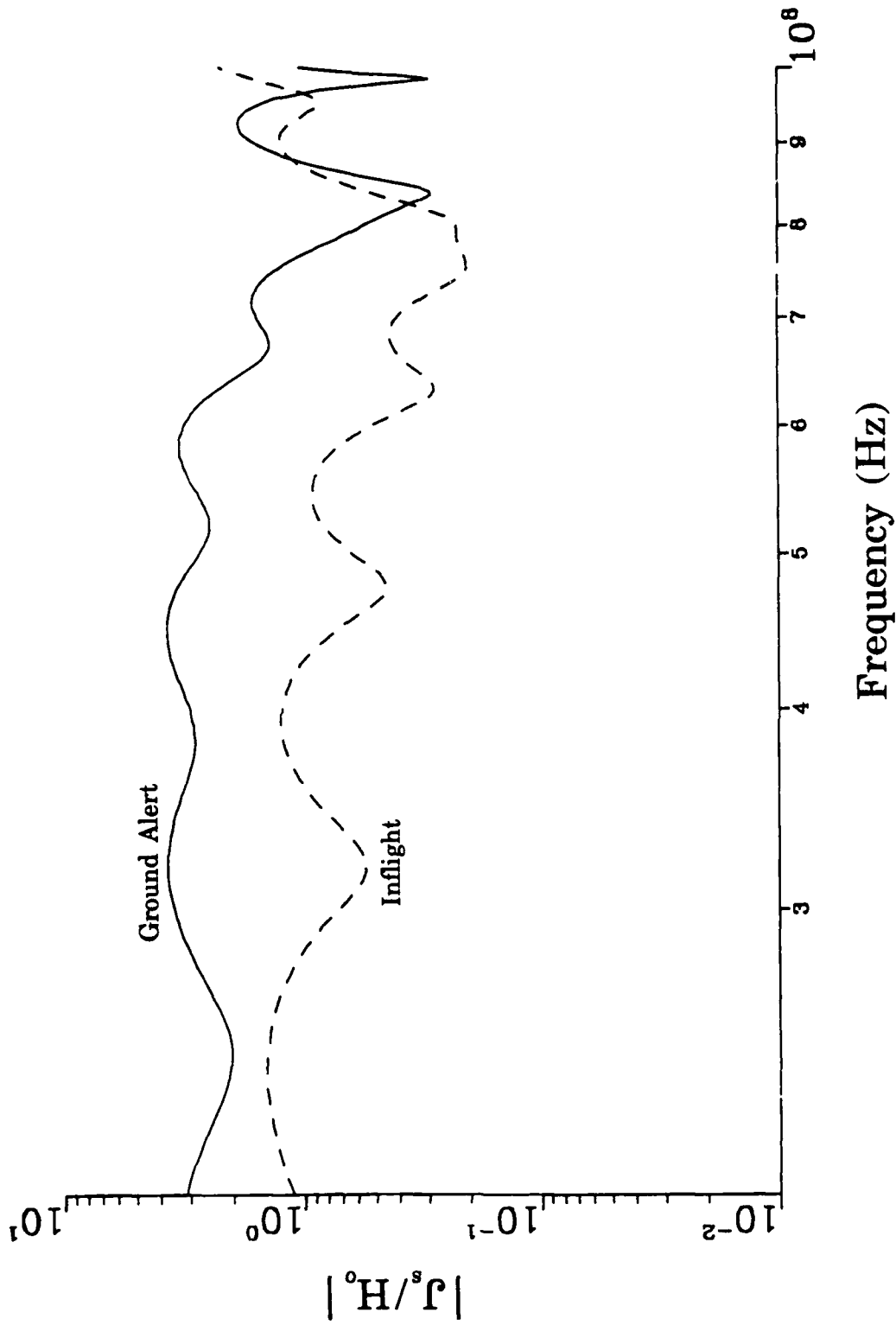


Figure 60. The EMPTAC normalized current density on the top of the front fuselage (10.29 m from the nose) for nose and fin-cap antenna excitation (physical optics approximation).

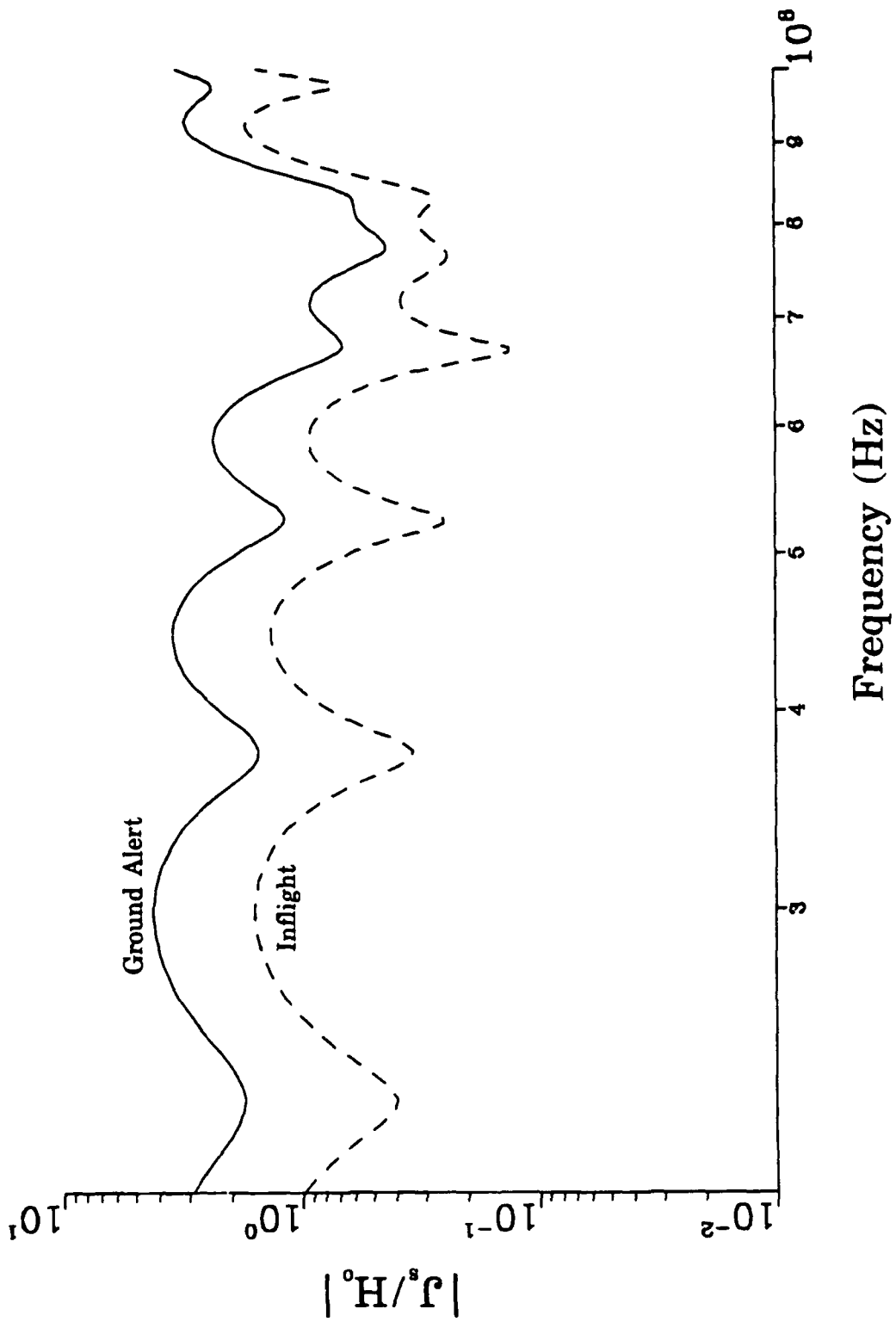


Figure 61. The EMPTAC normalized current density on the bottom of the front fuselage (10.29 m from the nose) for nose and fin-cap antenna excitation (physical optics approximation).

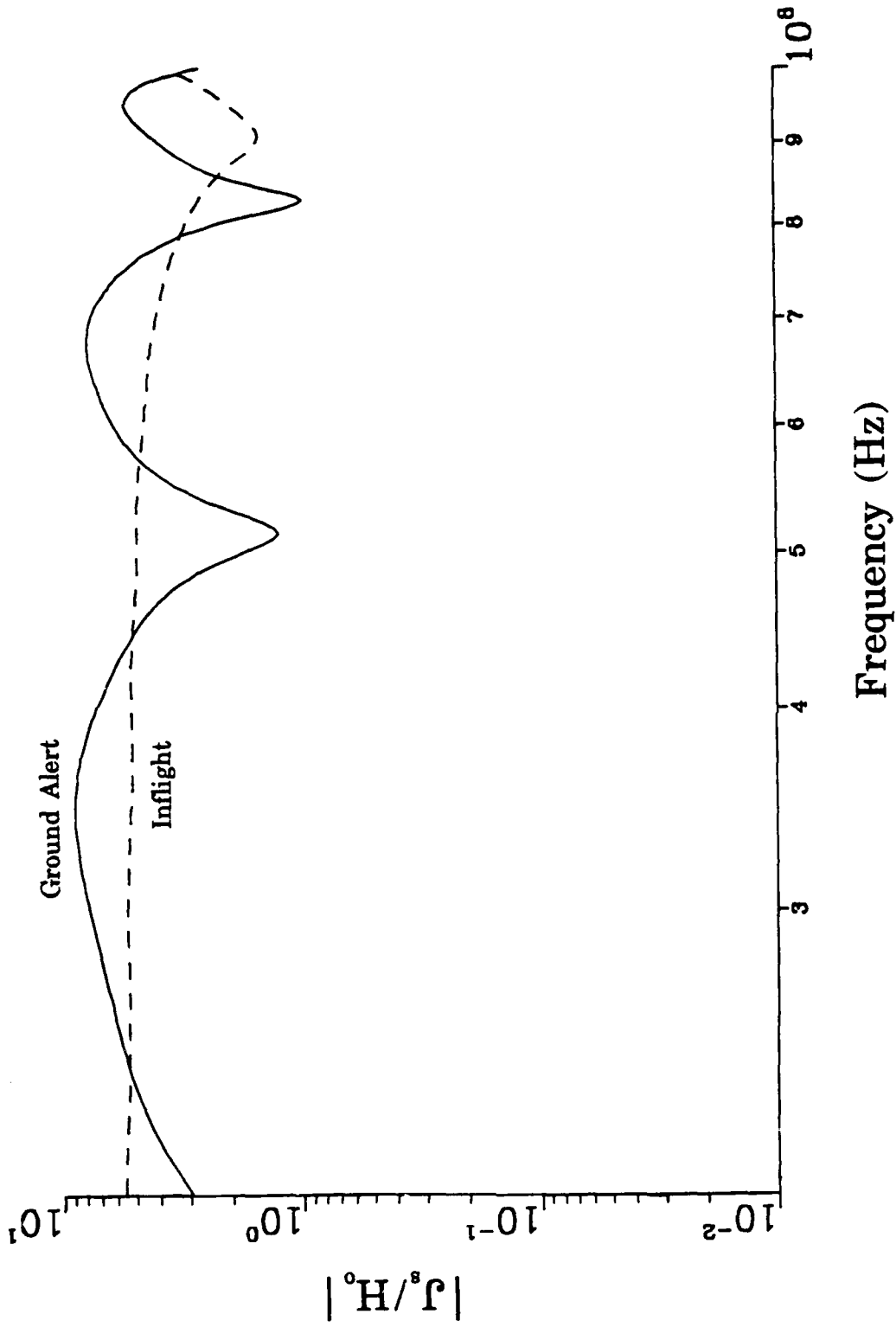


Figure 62. The EMP-AC normalized current density on the top of the mid fuselage (18.69 m from the wing-fuselage junction) for nose and fin-cap antenna excitation (physical optics approximation).

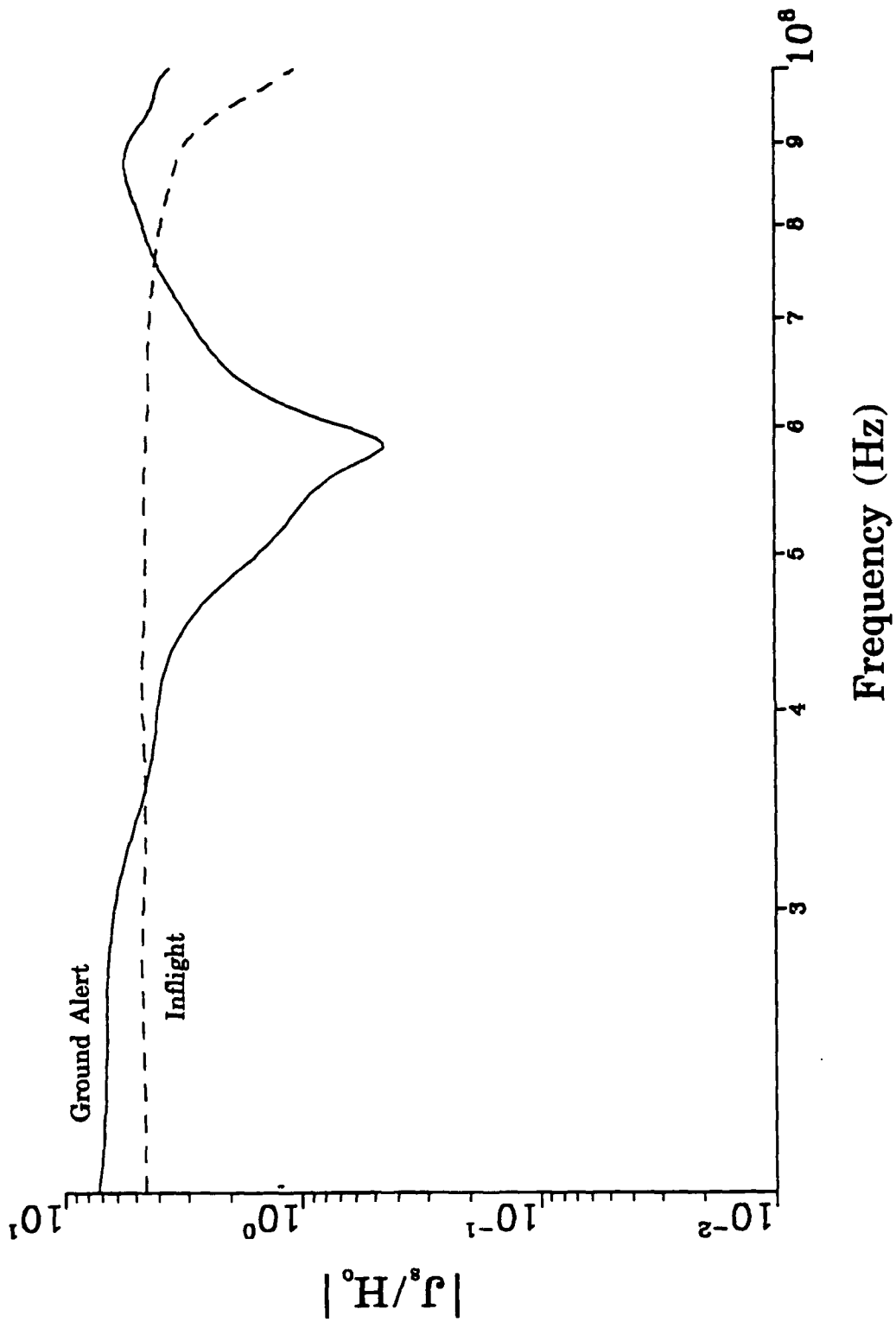


Figure 63. The EMPTAC normalized current density on the bottom of the mid fuselage (18.69 m from the wing-fuselage junction) for nose and fin-cap antenna excitation (physical optics approximation).

4.2.3 Response of the EMPTAC to Excitation of the Port Wing Antenna (20 to 100 MHz)

The normalized responses of the EMPTAC to excitation of the port wing antenna are shown in Figures 66 through 73. Figures 66 and 67 represent the normalized current density on the top and bottom of the front fuselage (test points #1 and #2, respectively). Figures 68 and 69 represent the normalized current density on the top and bottom of the mid fuselage (test points #3 and #4, respectively). Figures 70 and 71 represent the normalized current density at points on the top of the port wing (test points #5 and #6, respectively). Figures 72 and 73 represent the normalized current density at points on the top of the starboard wing (test points #7 and #8, respectively).

4.2.4 Response of the EMPTAC to Excitation of the Port and Starboard Wing Antennas (20 to 100 MHz)

The normalized responses of the EMPTAC to simultaneous excitation of the port and starboard wing antennas are shown in Figures 74 through 79. Figures 74 and 75 represent the normalized current density on the top and bottom of the front fuselage (test points #1 and #2, respectively). Figures 76 and 77 represent the normalized current density on the top and bottom of the mid fuselage (test points #3 and #4, respectively). Figures 78 and 79 represent the normalized current density at points on the top of the port wing (test points #5 and #6, respectively). The starboard wing responses (test points #7, #8 and #12) predicted by the method-of-moments solution are identical to the corresponding points on the port wing.

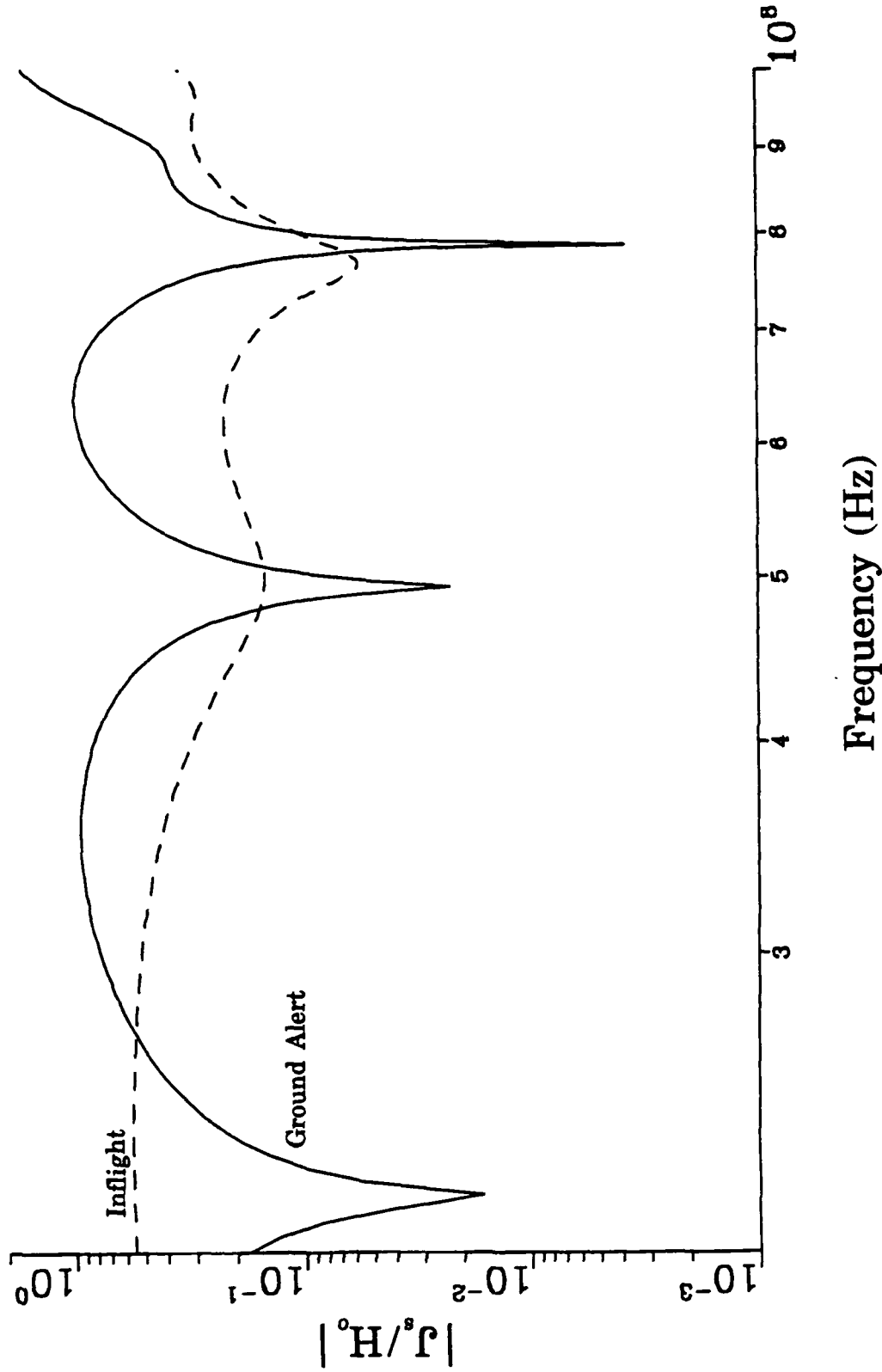


Figure 64. The EMPTAC normalized current density on the top of the port wing (3.9 m from the wing-fuselage junction) for nose and fin-cap antenna excitation (physical optics approximation).

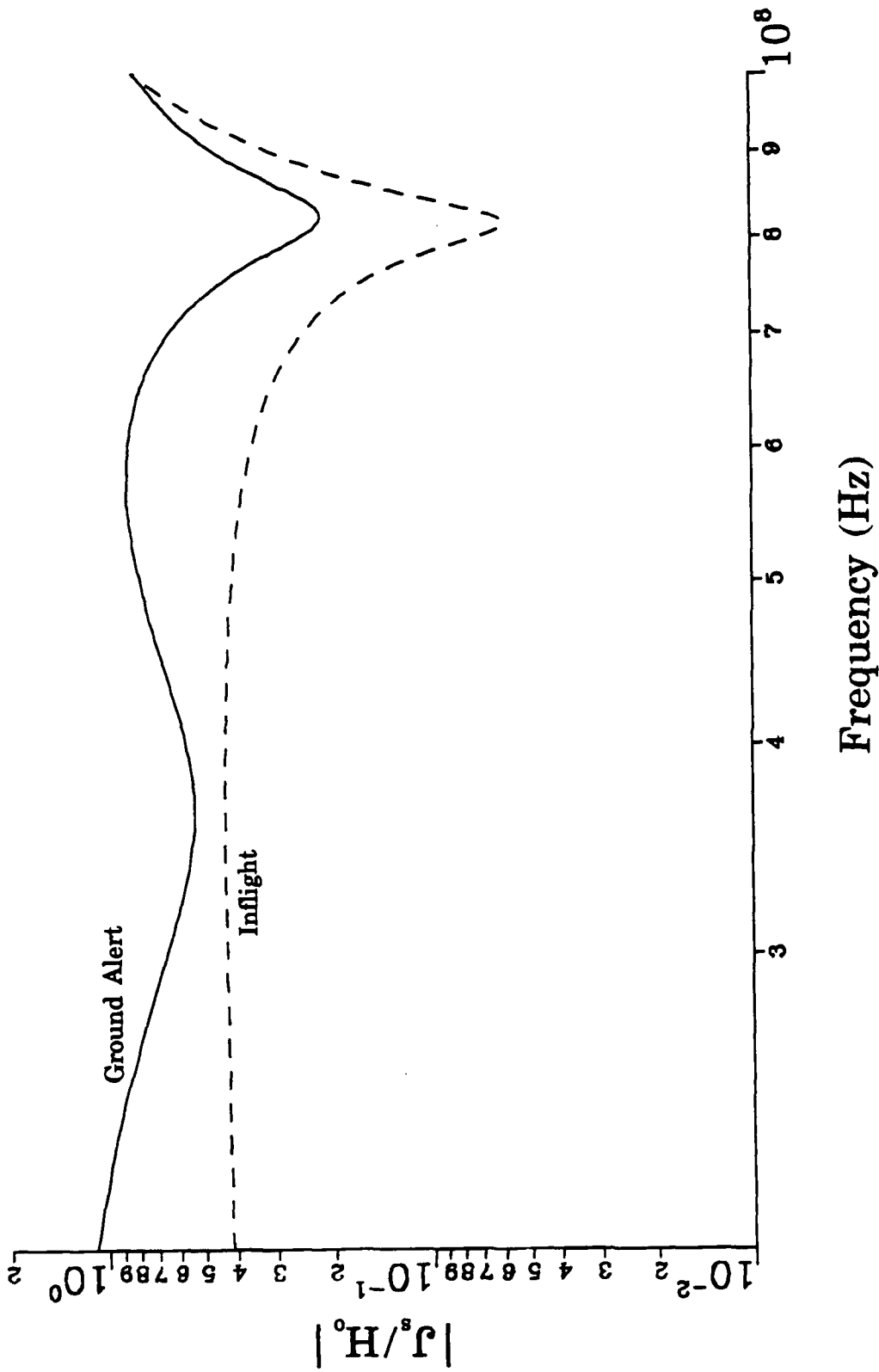


Figure 65. The EMPTAC normalized current density on the top of the port wing (11.7 m from the wing-fuselage junction) for nose and fin-cap antenna excitation (physical optics approximation).

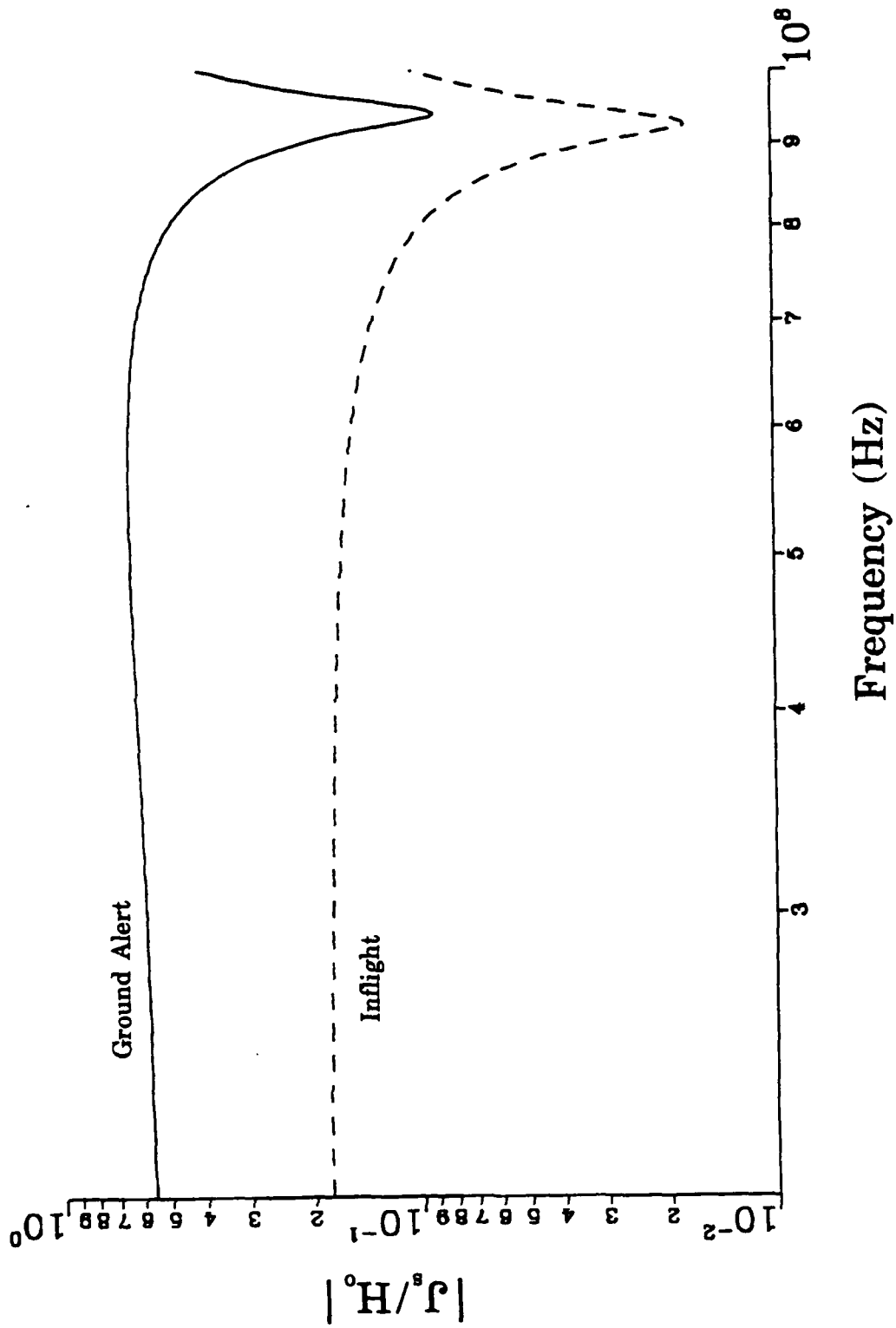


Figure 66. The EMPTAC normalized current density on the top of the front fuselage (10.29 m from the nose) for port wing antenna excitation (physical optics approximation).

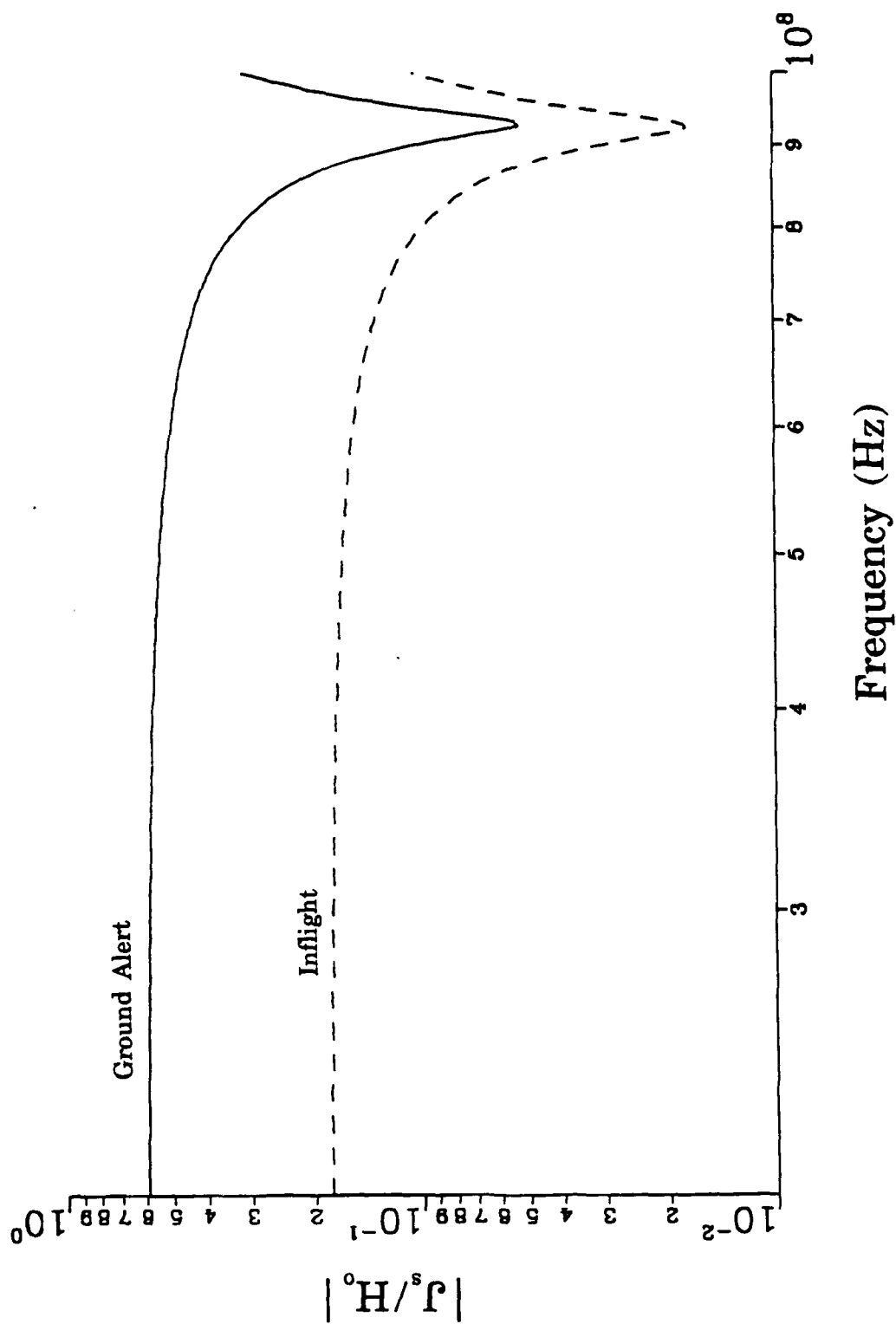


Figure 67. The EMPTAC normalized current density on the bottom of the front fuselage (10.29 m from the nose) for port wing antenna excitation (physical optics approximation).

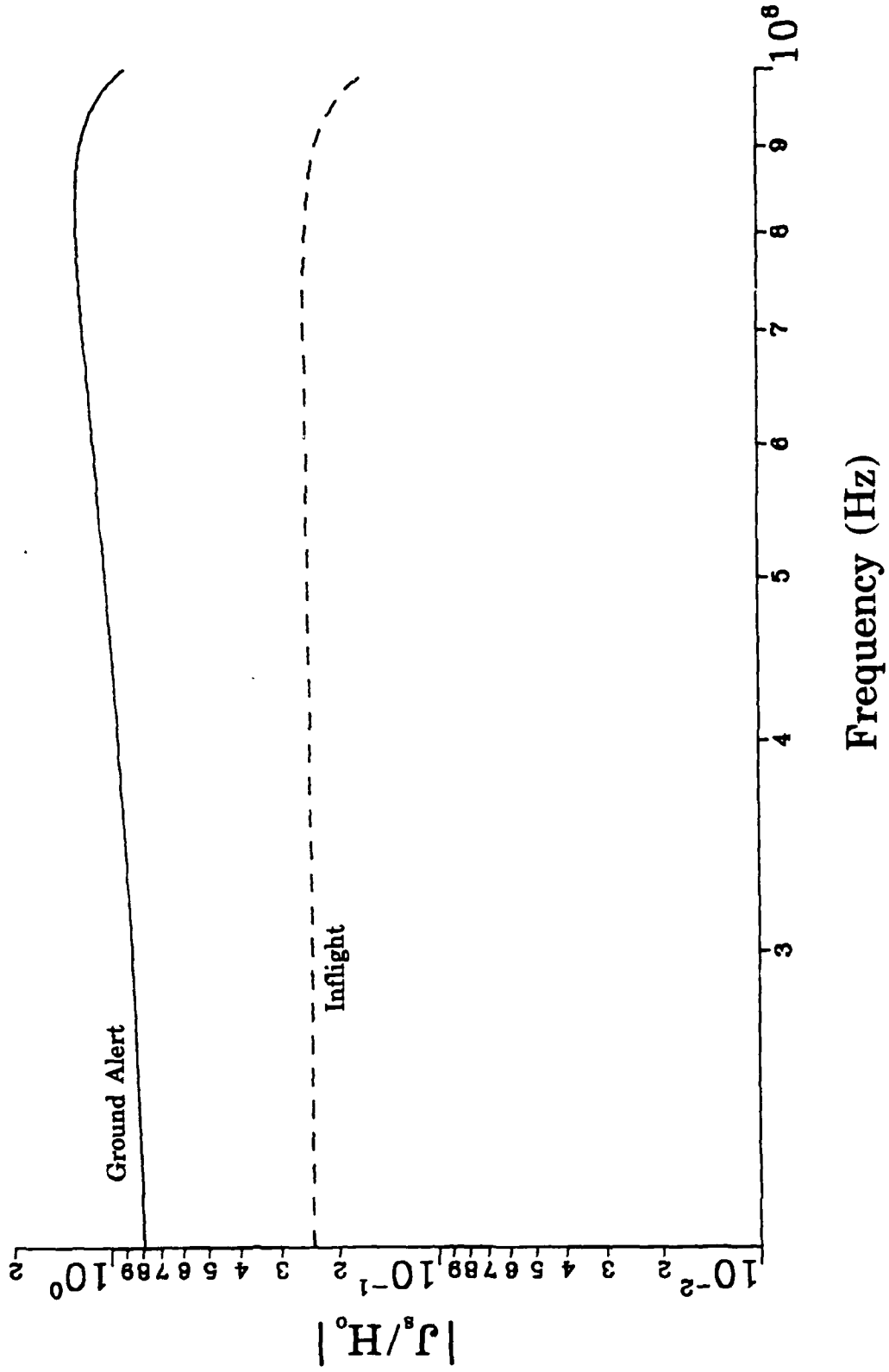


Figure 68. The EMPTAC normalized current density on the top of the mid fuselage (18.69 m from the wing-fuselage junction) for port wing antenna excitation (physical optics approximation).

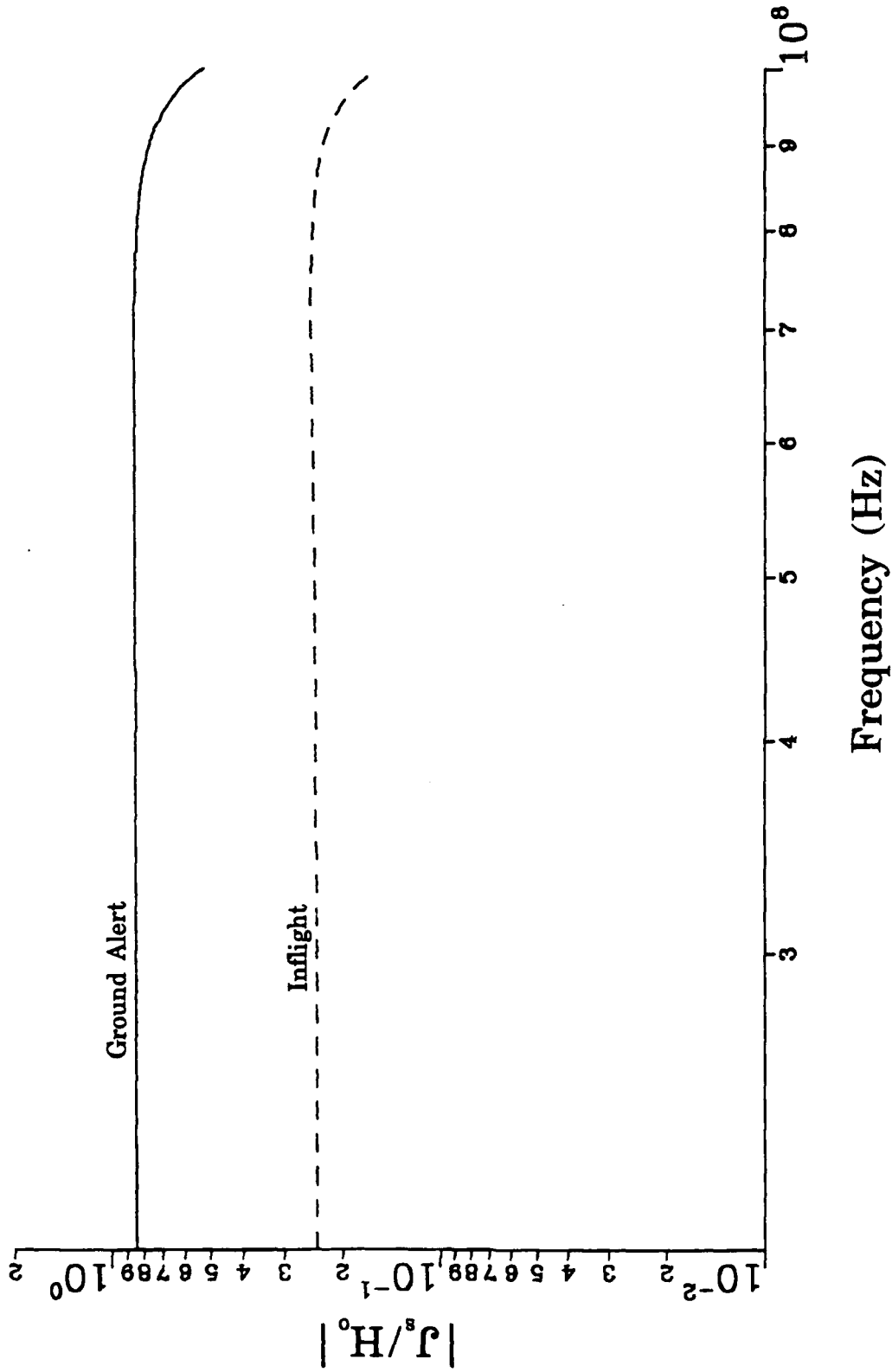


Figure 69. The EMPTAC normalized current density on the bottom of the mid fuselage (18.69 m from the wing-fuselage junction) for port wing antenna excitation (physical optics approximation).

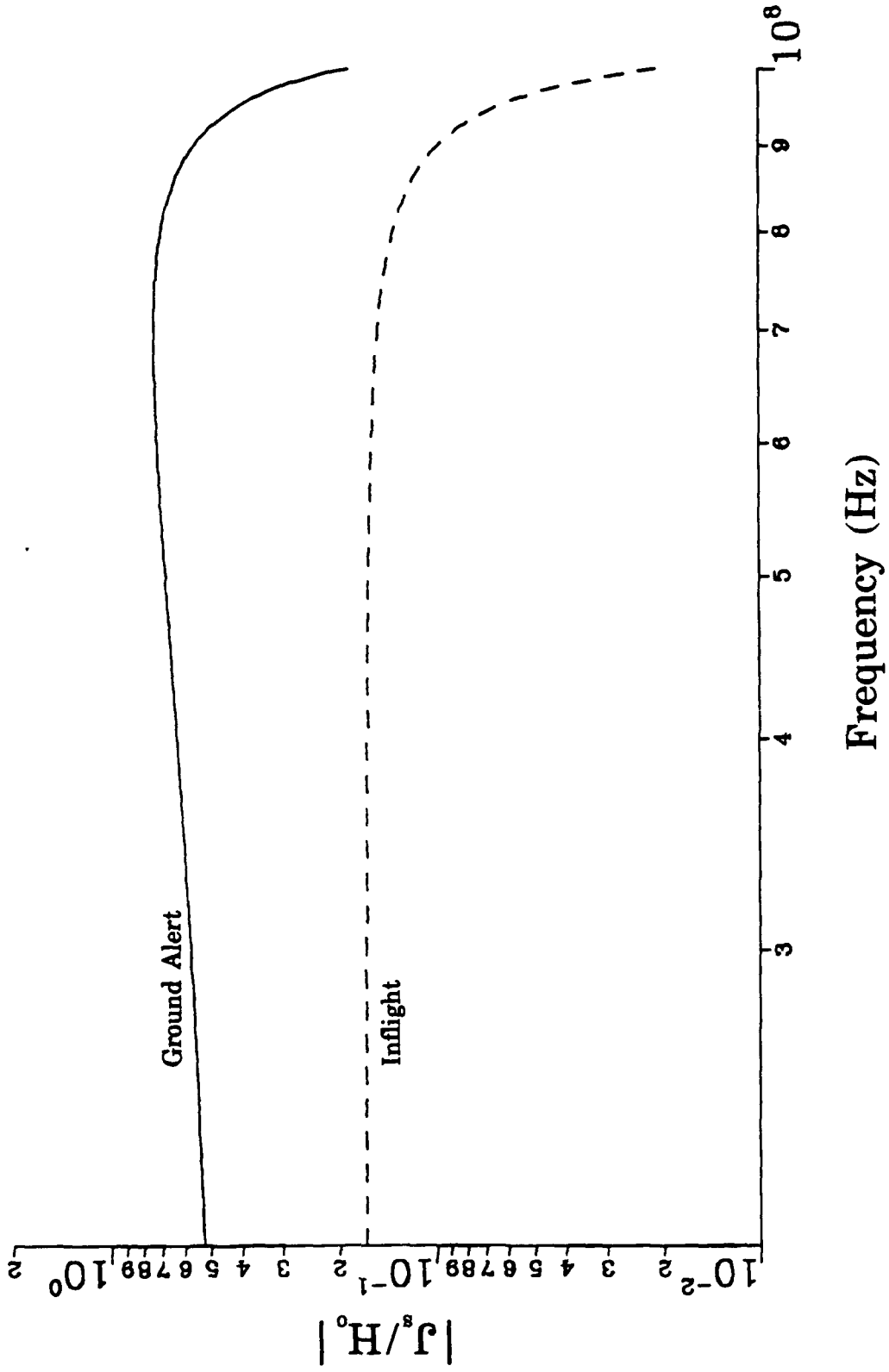


Figure 70. The EMPTAC normalized current density on the top of the port wing (3.9 m from the wing-fuselage junction) for port wing antenna excitation (physical optics approximation).

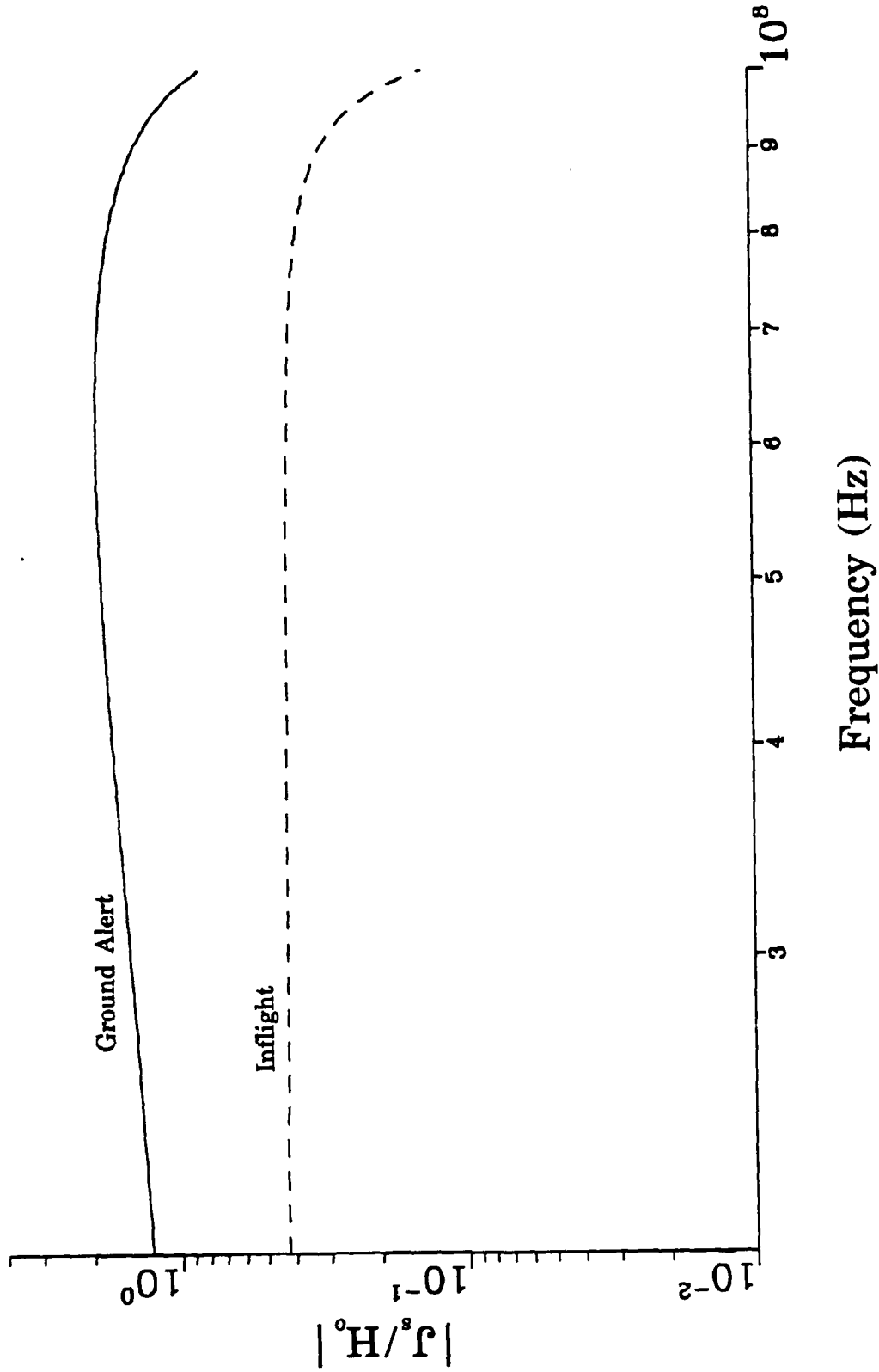


Figure 71. The EMPTAC normalized current density on the top of the port wing (11.7 m from the wing-fuselage junction) for port wing antenna excitation (physical optics approximation).

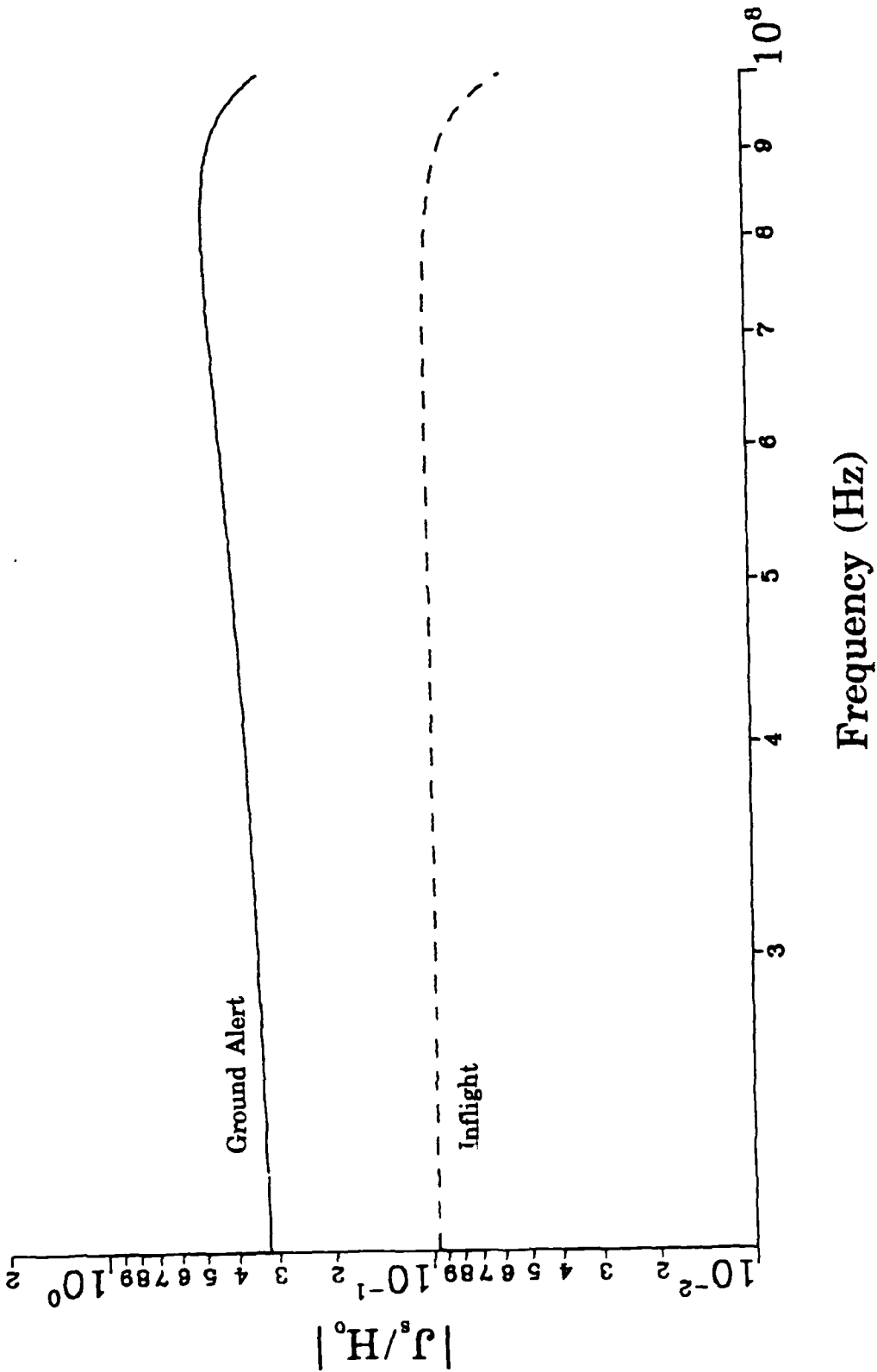


Figure 72. The EMPTAC normalized current density on the top of the starboard wing (3.9 m from the wing-fuselage junction) for port wing antenna excitation (physical optics approximation).

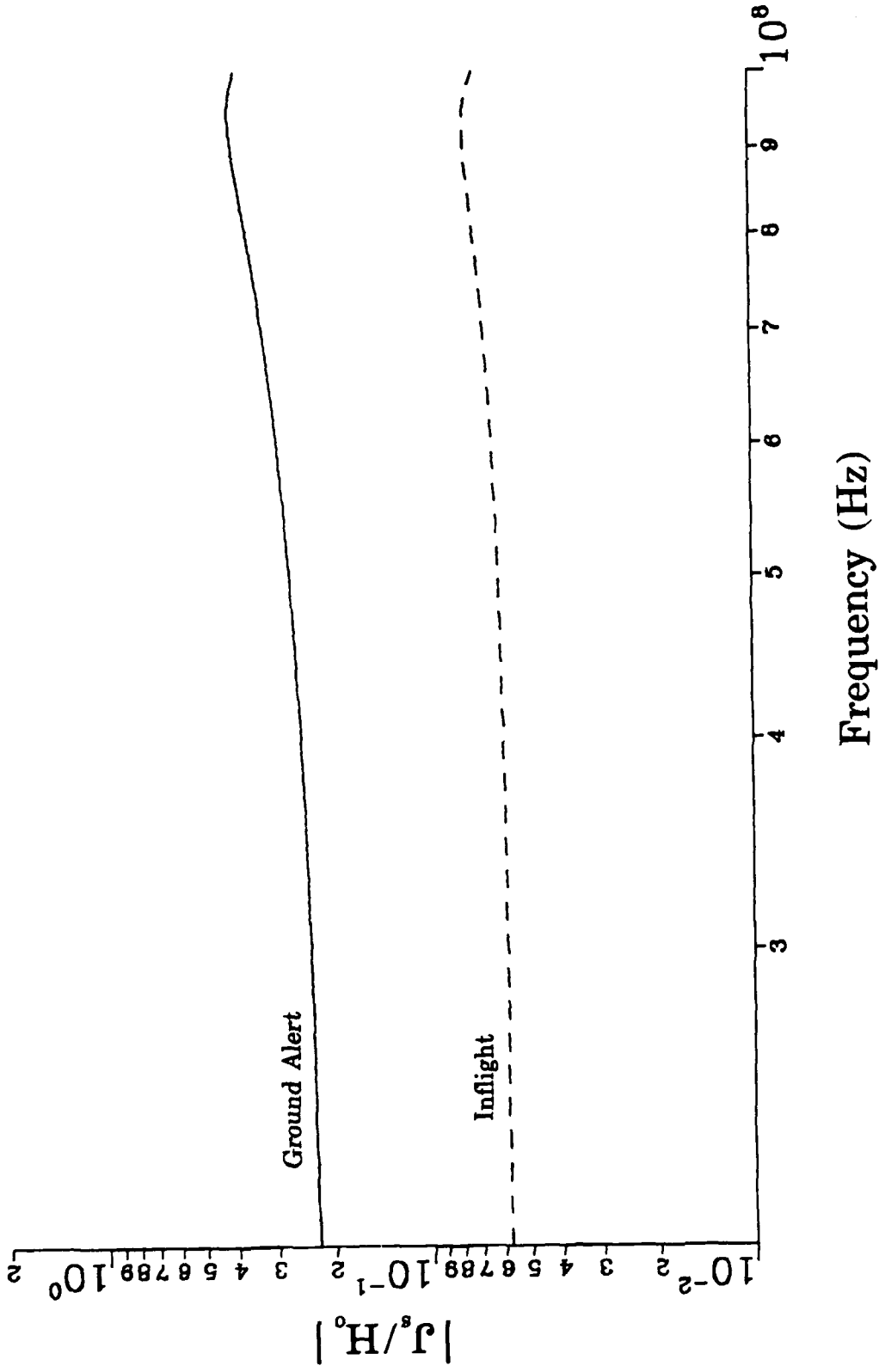


Figure 73. The EMPTAC normalized current density on the top of the starboard wing (11.7 m from the wing-fuselage junction) for port wing antenna excitation (physical optics approximation).

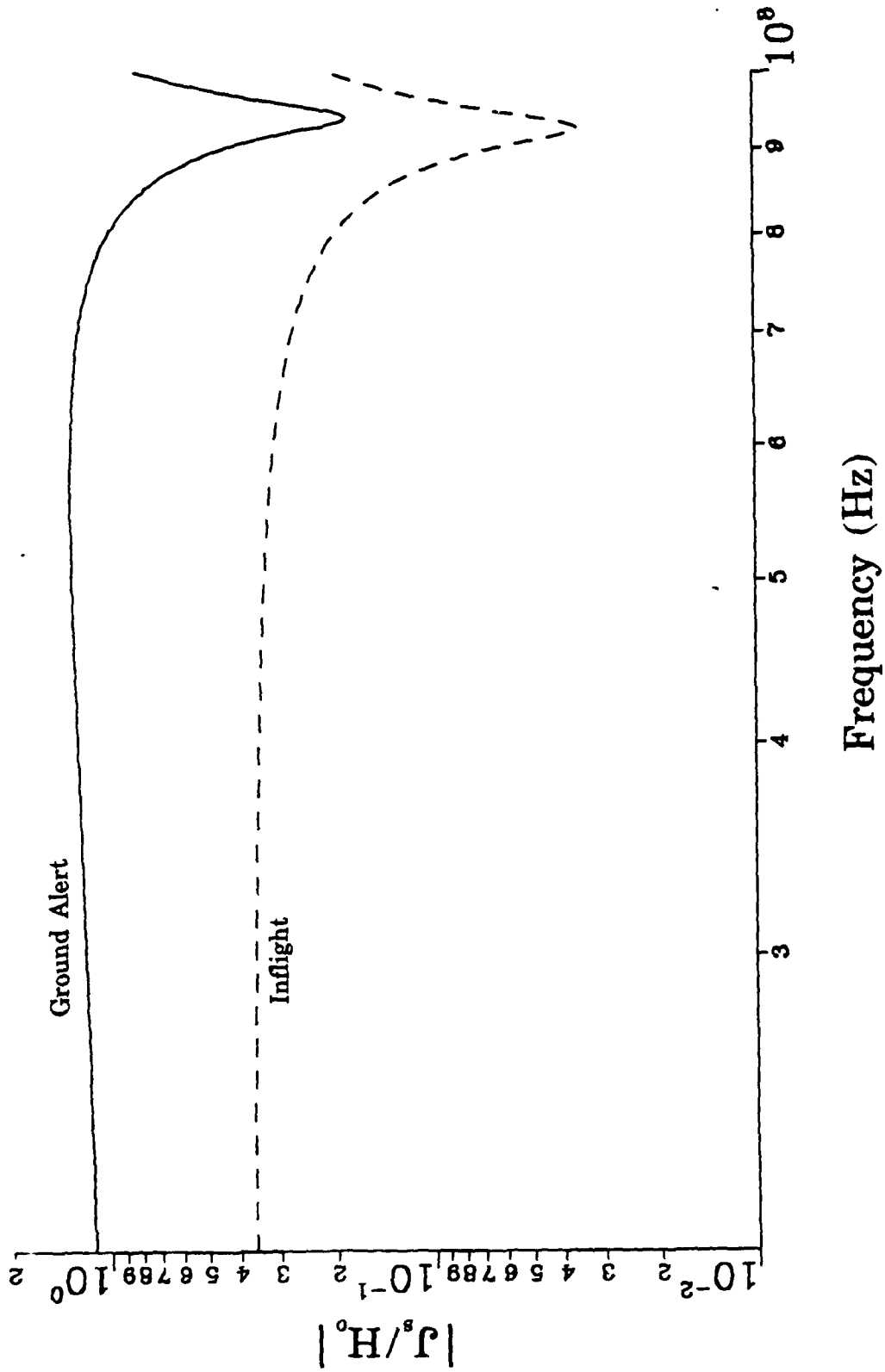


Figure 74. The EMPTAC normalized current density on the top of the front fuselage (10.29 m from the nose) for port and starboard wing antenna excitation (physical optics approximation).

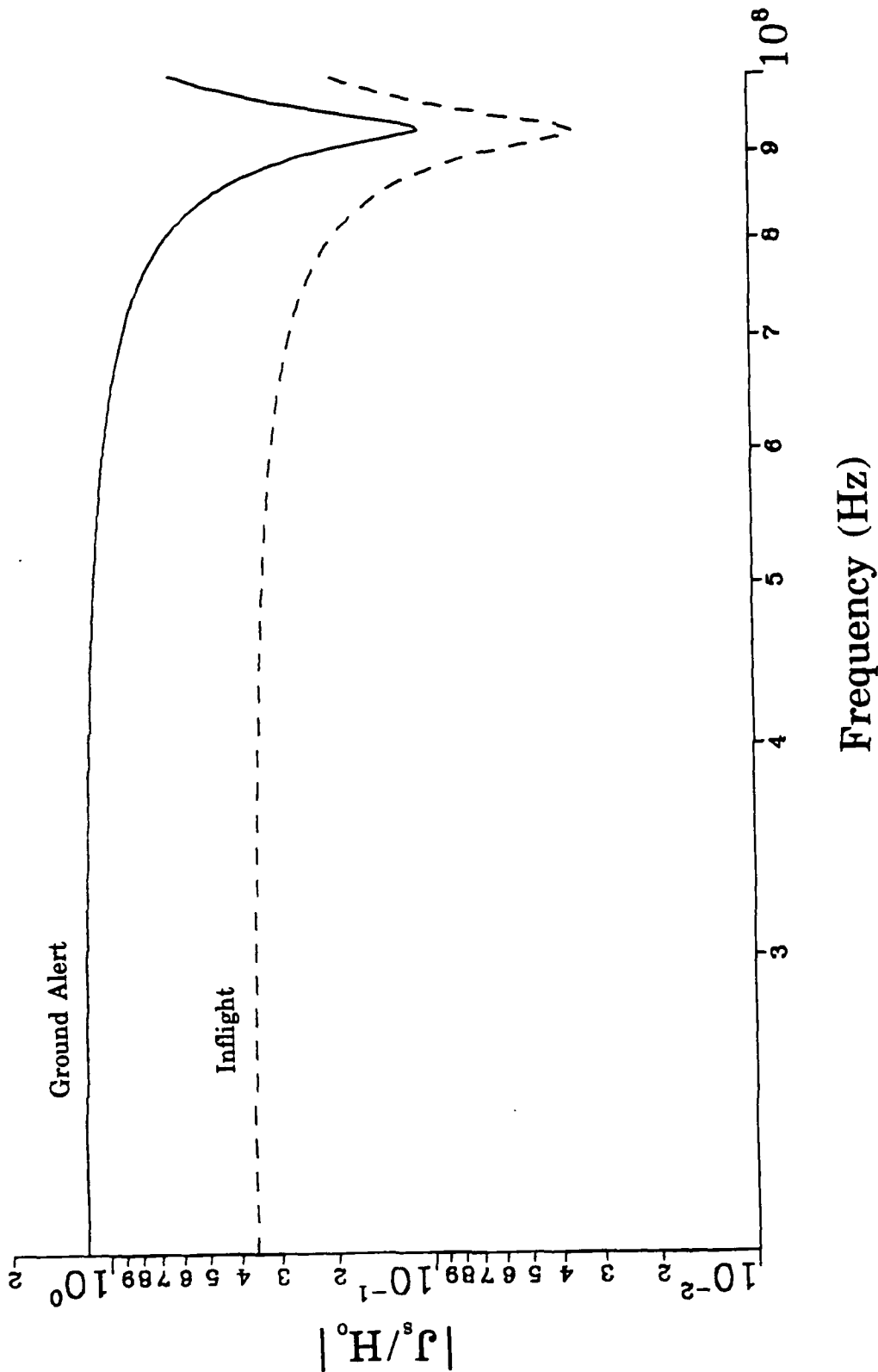


Figure 75. The EMPTAC normalized current density on the bottom of the front fuselage (10.29 m from the nose) for starboard and port wing antenna excitation (physical optics approximation).

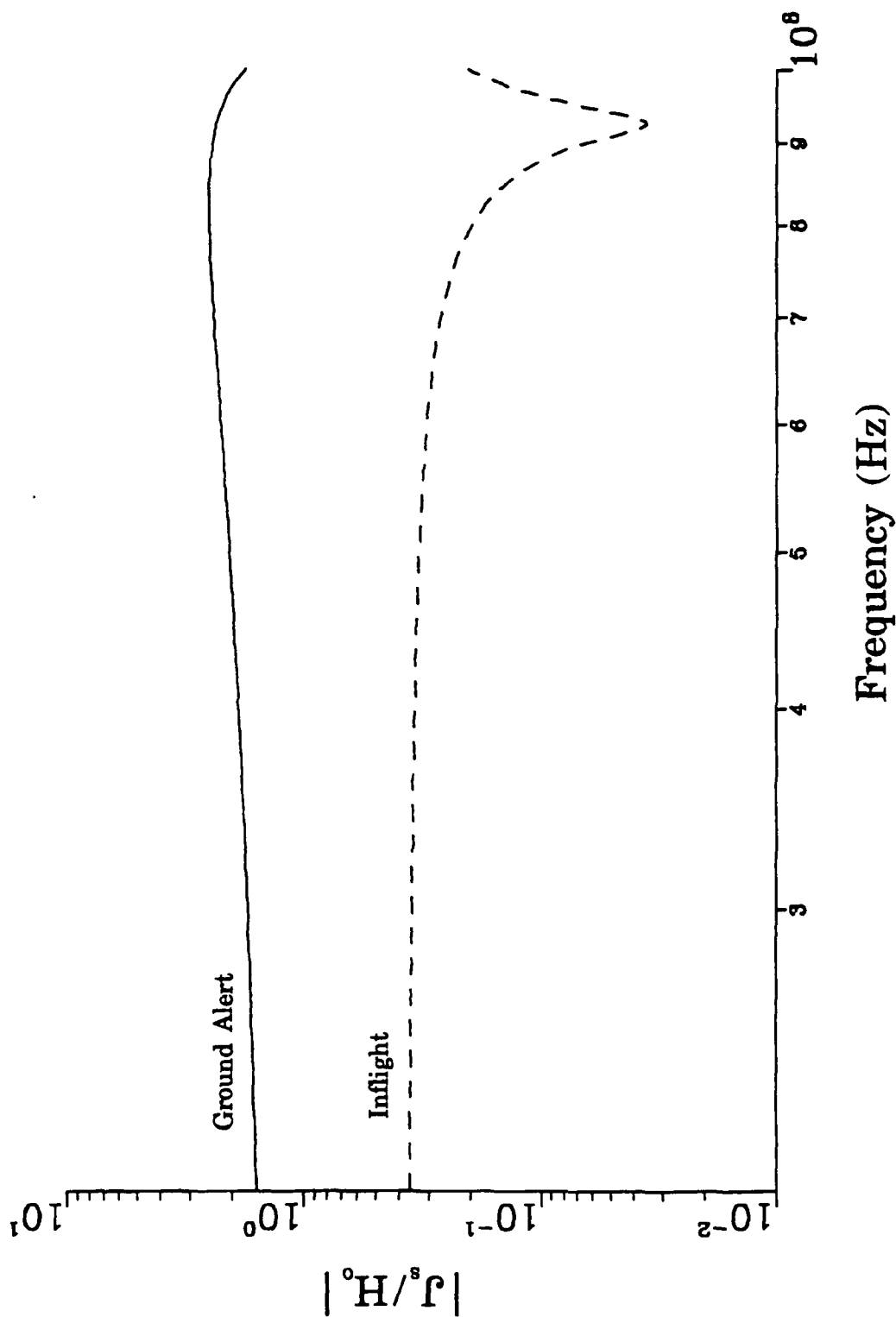


Figure 76. The EMPTAC normalized current density on the top of the mid fuselage (18.69 m from the wing-fuselage junction) for port and starboard wing antenna excitation (physical optics approximation).

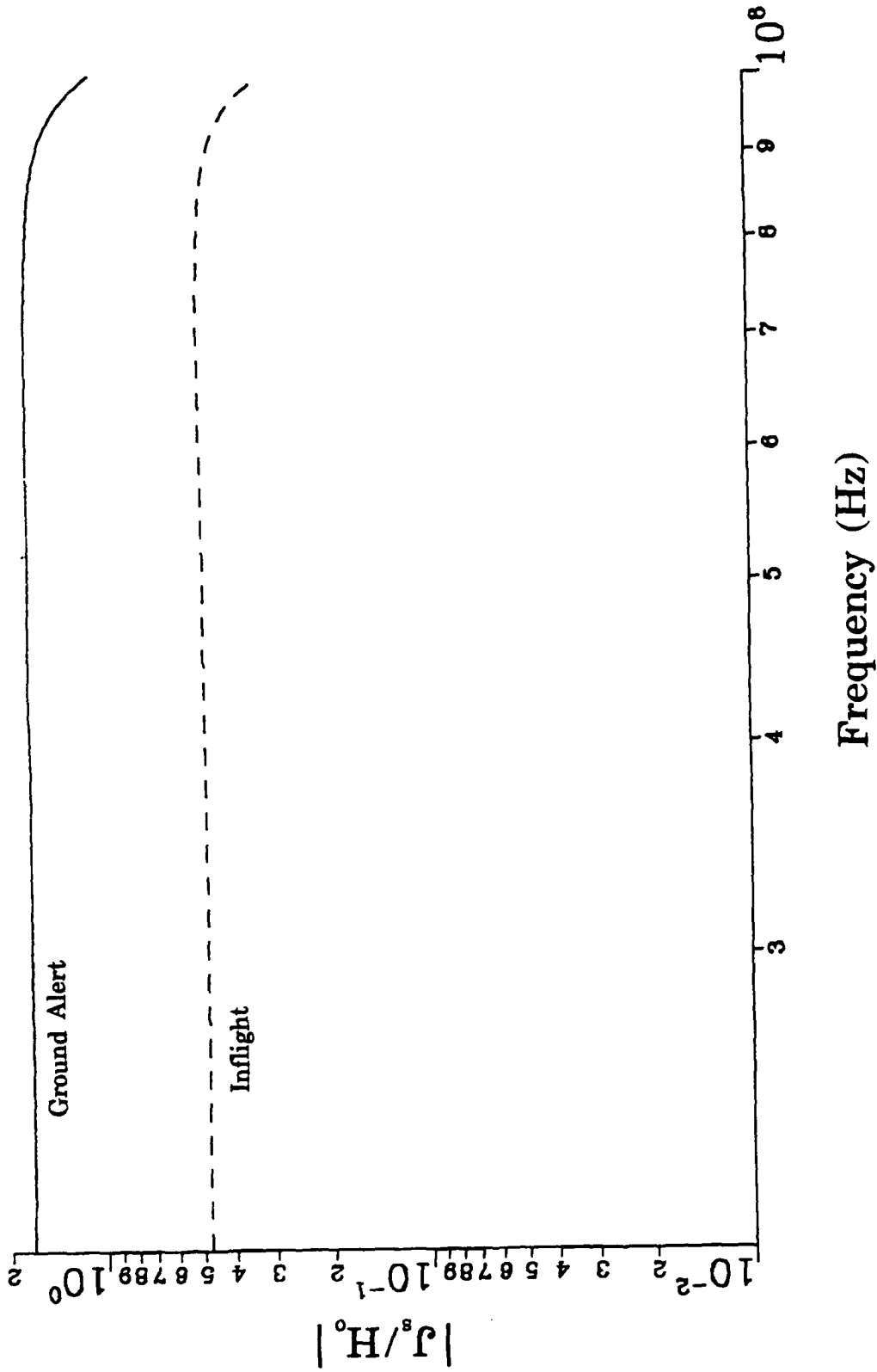


Figure 77. The EMPTAC normalized current density on the bottom of the mid fuselage (18.69 m from the wing-fuselage junction) for port and starboard wing antenna excitation (physical optics approximation).

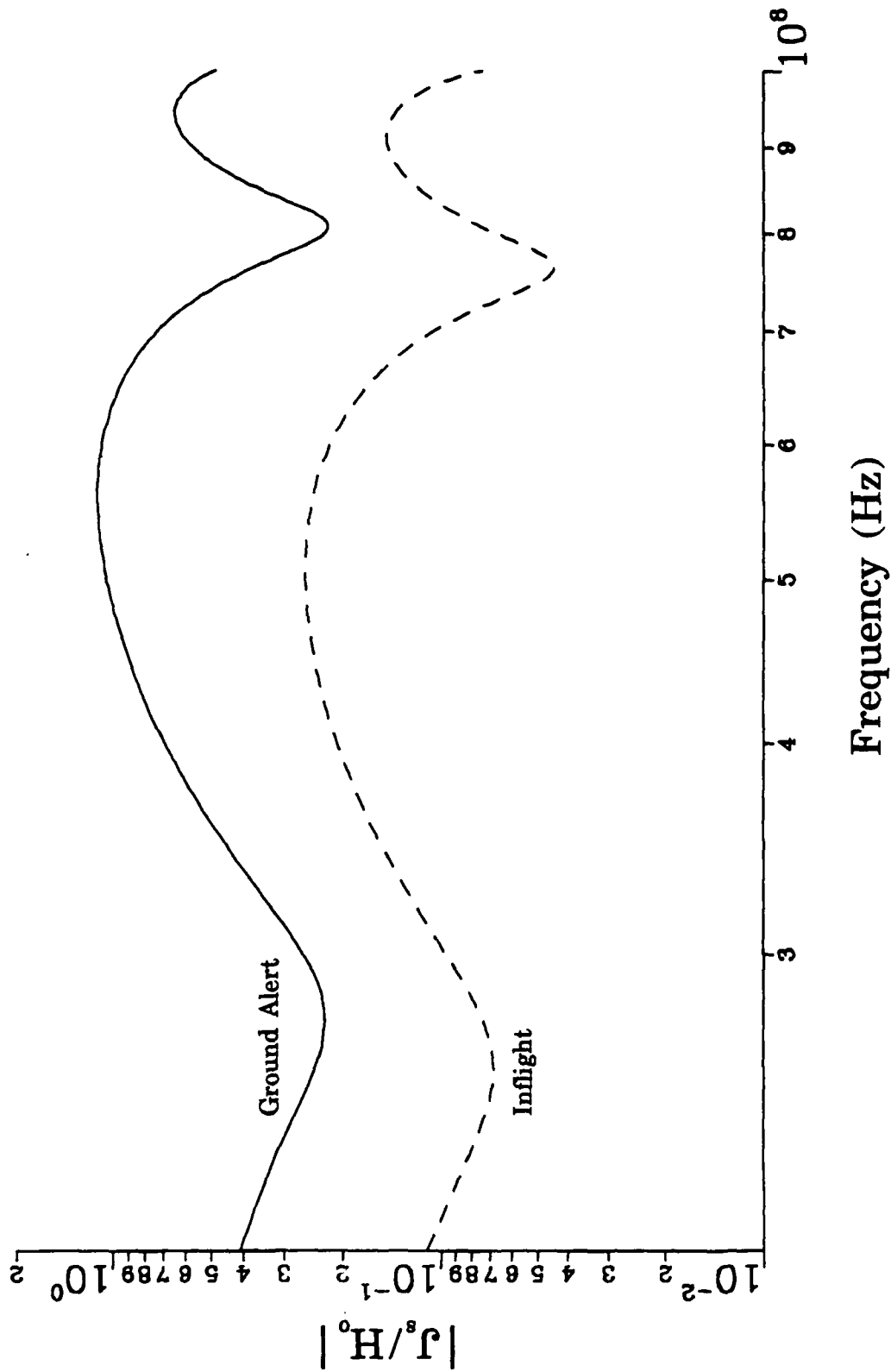


Figure 78. The EMPTAC normalized current density on the top of the port wing (3.9 m from the wing-fuselage junction) for port and starboard wing antenna excitation (physical optics approximation).

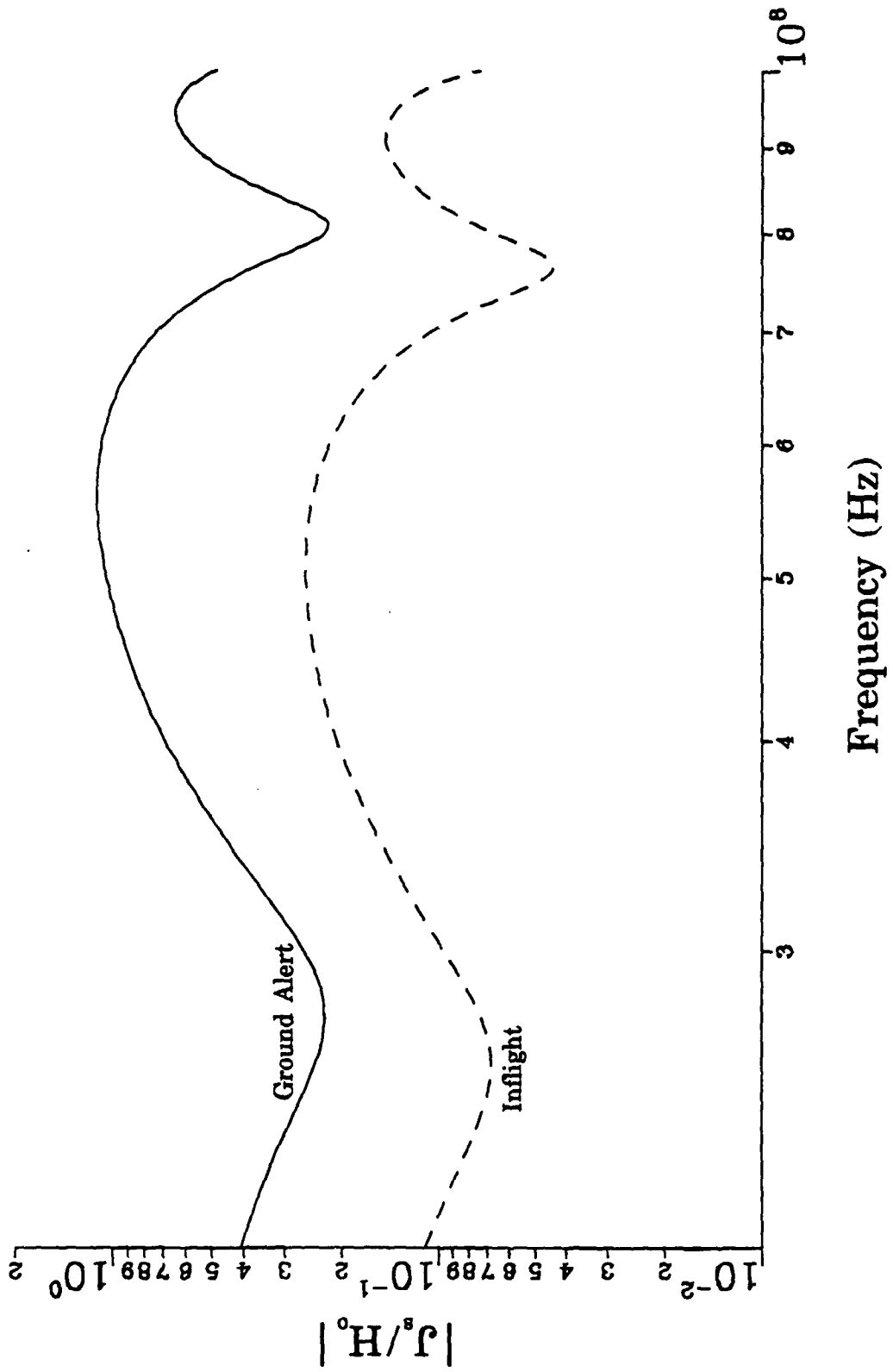


Figure 79. The EMP/TAC normalized current density on the top of the port wing (11.7 m from the wing-fuselage junction) for port and starboard wing antenna excitation (physical optics approximation).

## 5.0 EMPTAC RESPONSE DATA FROM THE HPD PULSER

The plane wave and HF antenna responses of the EMPTAC obtained numerically in Sections 3.0 and 4.0 are now compared with test data. The external response data presented in this section were generated using the HPD EMP simulator. The EMPTAC test points (matchpoints) defined for the numerical responses of Sections 3.0 and 4.0 were chosen as close to the HPD experimental test point locations as physically possible. Thus, the experimental test points are defined in the same manner as given in Section 2.0 (test points #1 through #12).

The particular external response data presented here were obtained at the HPD simulator during the EMPTAC 4 test in February 1989. Some of the data may be in error as much as 6 dB. The probable cause of this error is the attenuation of the analytic power dividers which were utilized in the measurements.

Figures 80 through 83 represent the EMPTAC surface current density measured on the top and bottom of the forward and mid fuselage (test points #1 through #4) when the fuselage is oriented parallel to the axis of the pulser which yields an electric field polarized parallel to the fuselage. Figures 84 through 86 represent the current density on the top of the port and starboard wings (test points #5, #7 and #8) with the fuselage oriented perpendicular to the pulser axis. The experimental data for test point #6 were unavailable. Figures 87 and 88 represent the surface charge densities on the nose and on the tip of the vertical stabilizer (test points #9 and #10, respectively) given the parallel orientation. Figures 89 and 90 represent the surface charge densities on the tips of the port and starboard wings (test points #11 and #12, respectively).

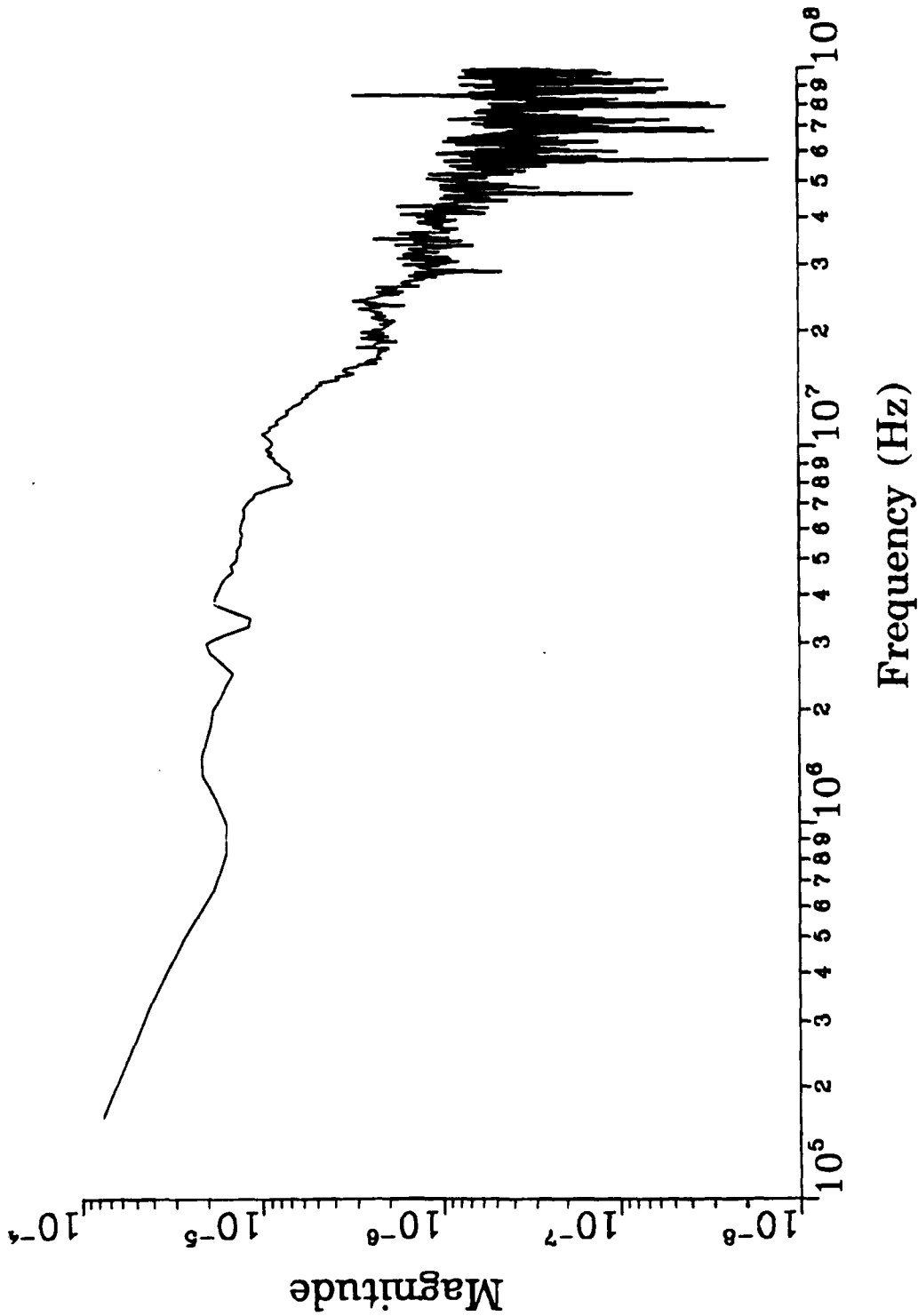


Figure 80. The EMPTAC surface current density on the top of the front fuselage (test point #1) (experimental data obtained from the HPD pulser, E III to fuselage).

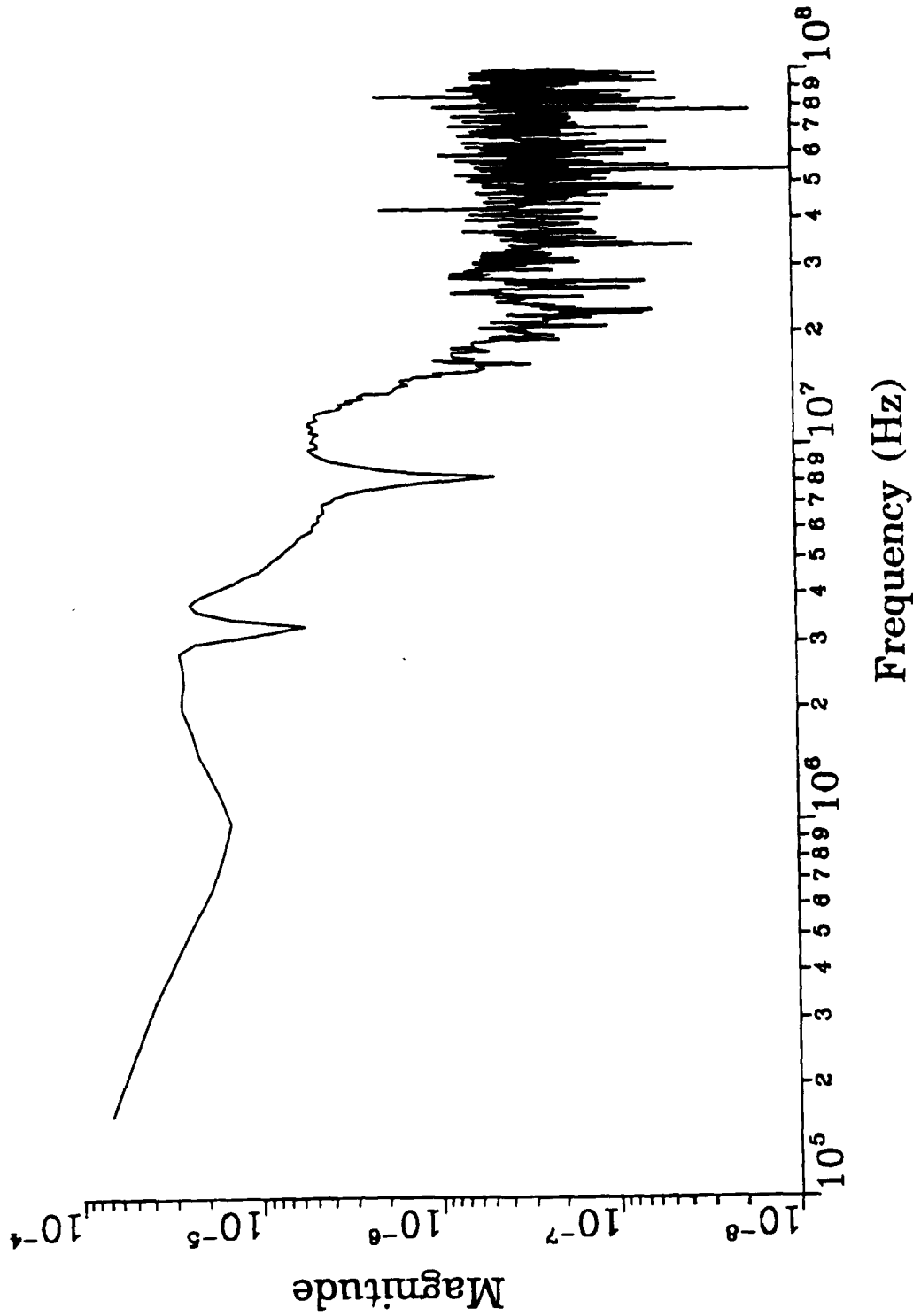


Figure 81. The EMP/TAC surface current density on the bottom of the front fuselage (test point #2) (experimental data obtained from the HPD pulser, E || to fuselage).

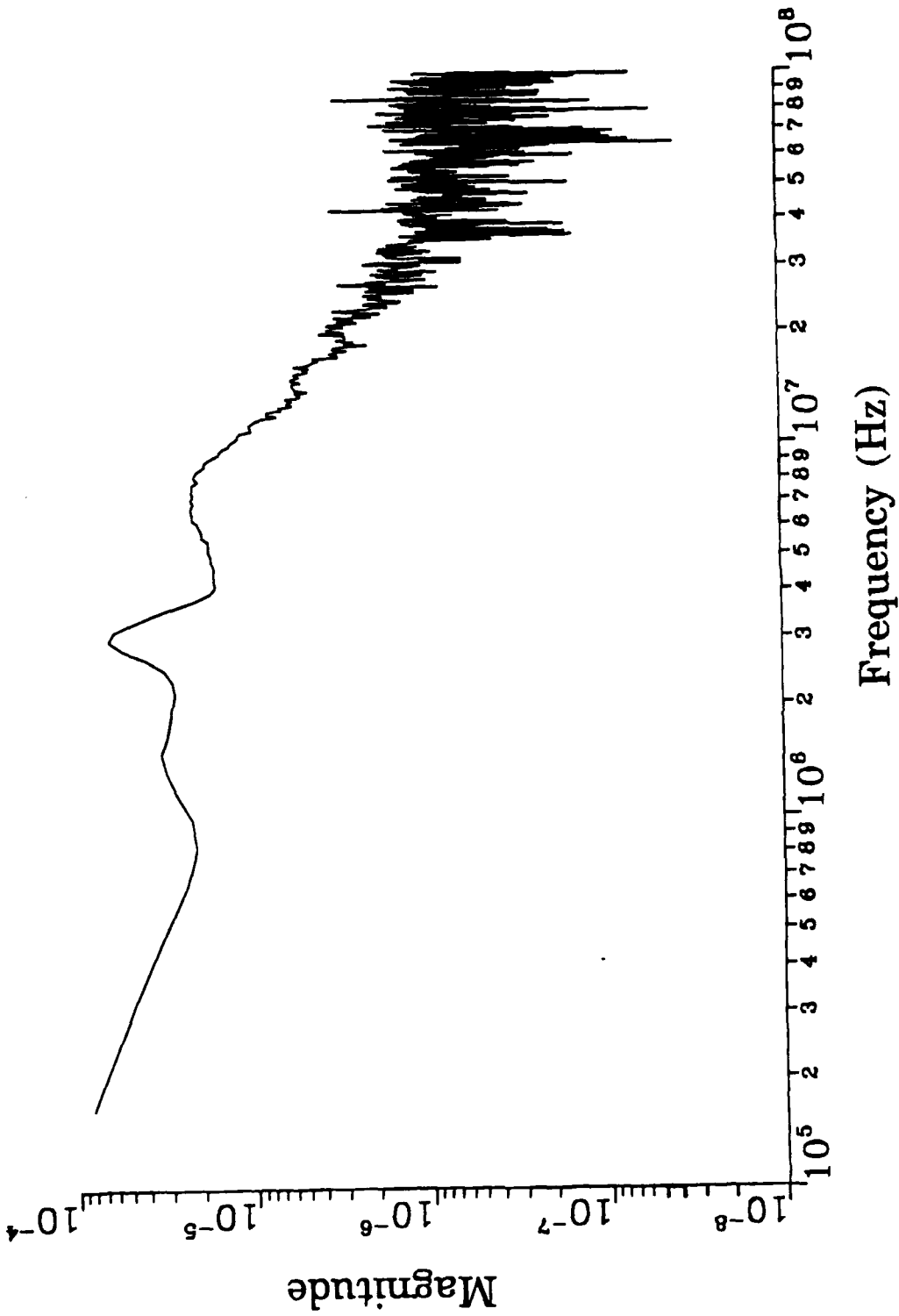


Figure 82. The EMPTAC surface current density on the top of the fuselage (test point #3) (experimental data obtained from the HPD pulser, E || to fuselage).

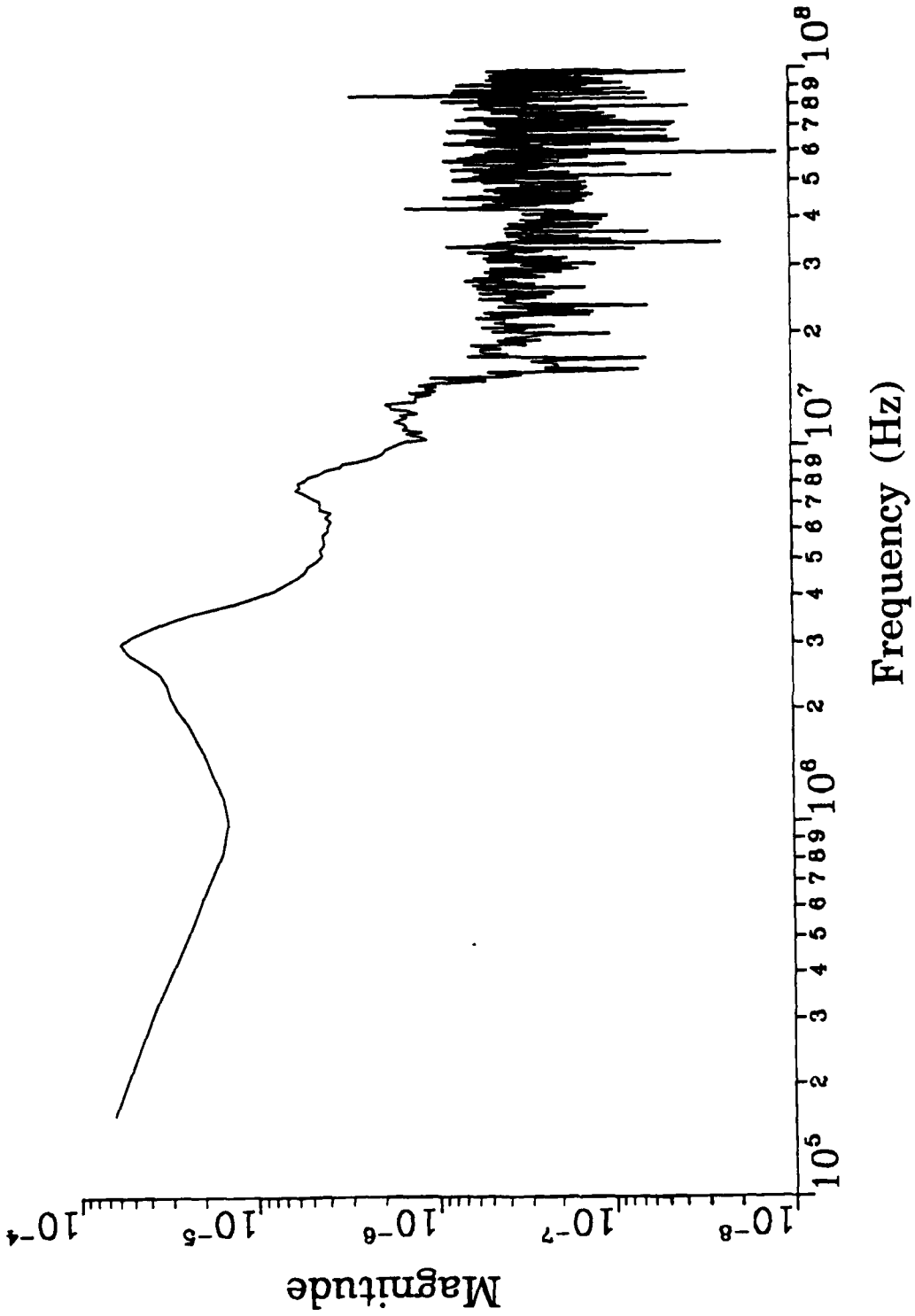


Figure 83. The EMPTAC surface current density on the bottom of the fuselage (test point #4) (experimental data obtained from the HPD pulser, E || to fuselage).

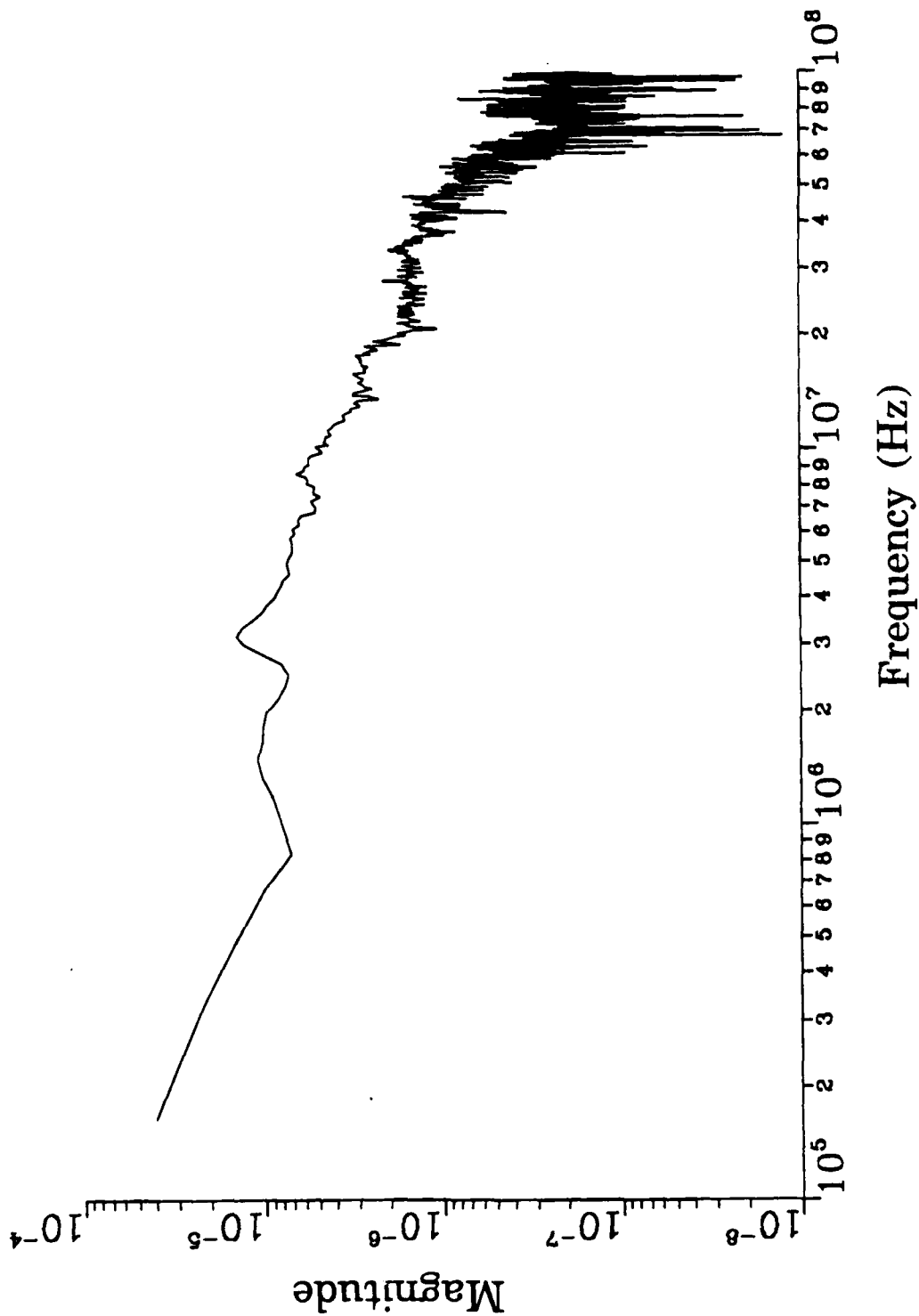


Figure 84. The EMPTAC surface current density on the top of the port wing (test point #5) (experimental data obtained from the HPD pulser, E ⊥ to fuselage).

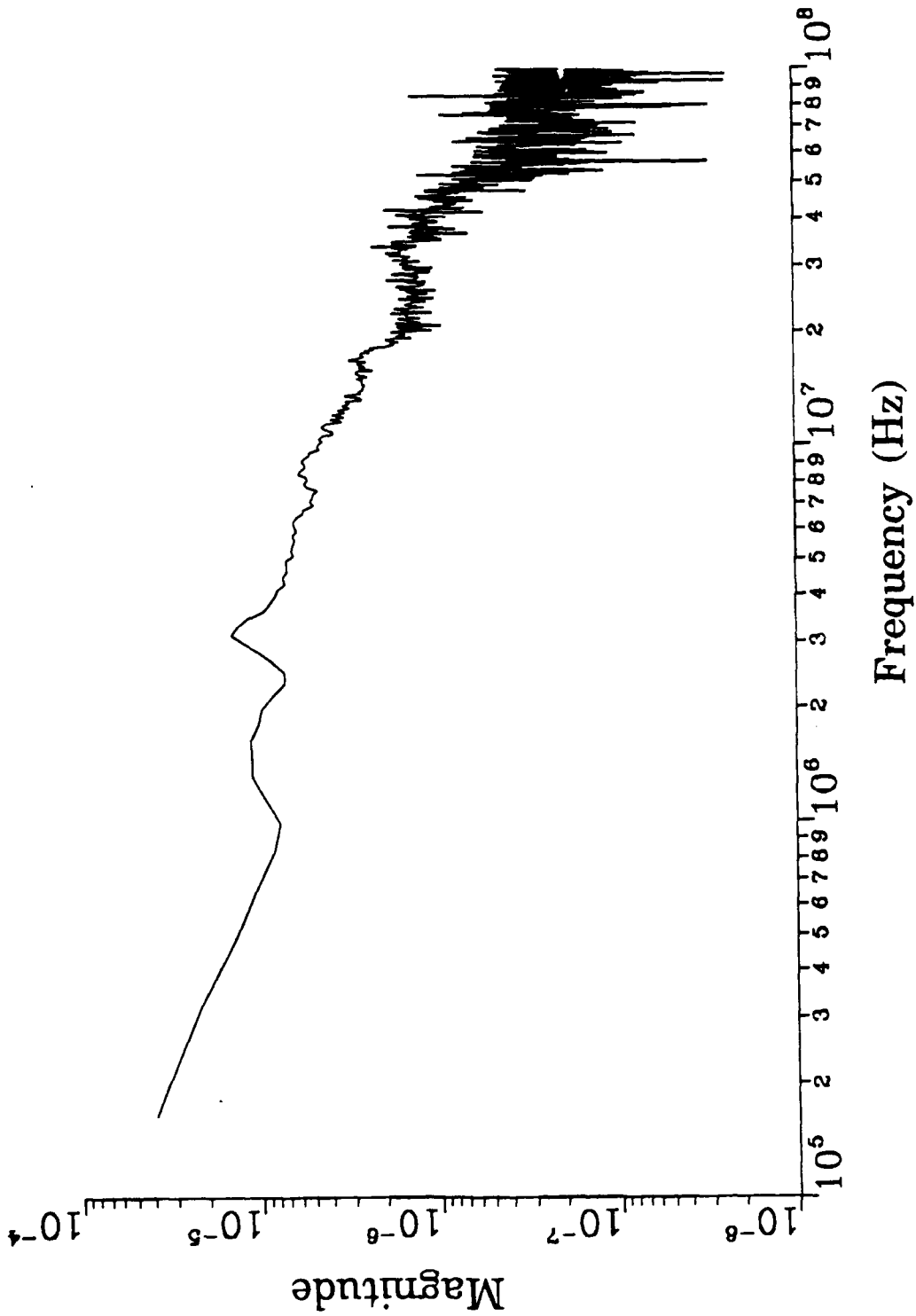


Figure 85. The EMPTAC surface current density on the top of the starboard wing (test point #7) (experimental data obtained from the HPD pulser, E ⊥ to fuselage).

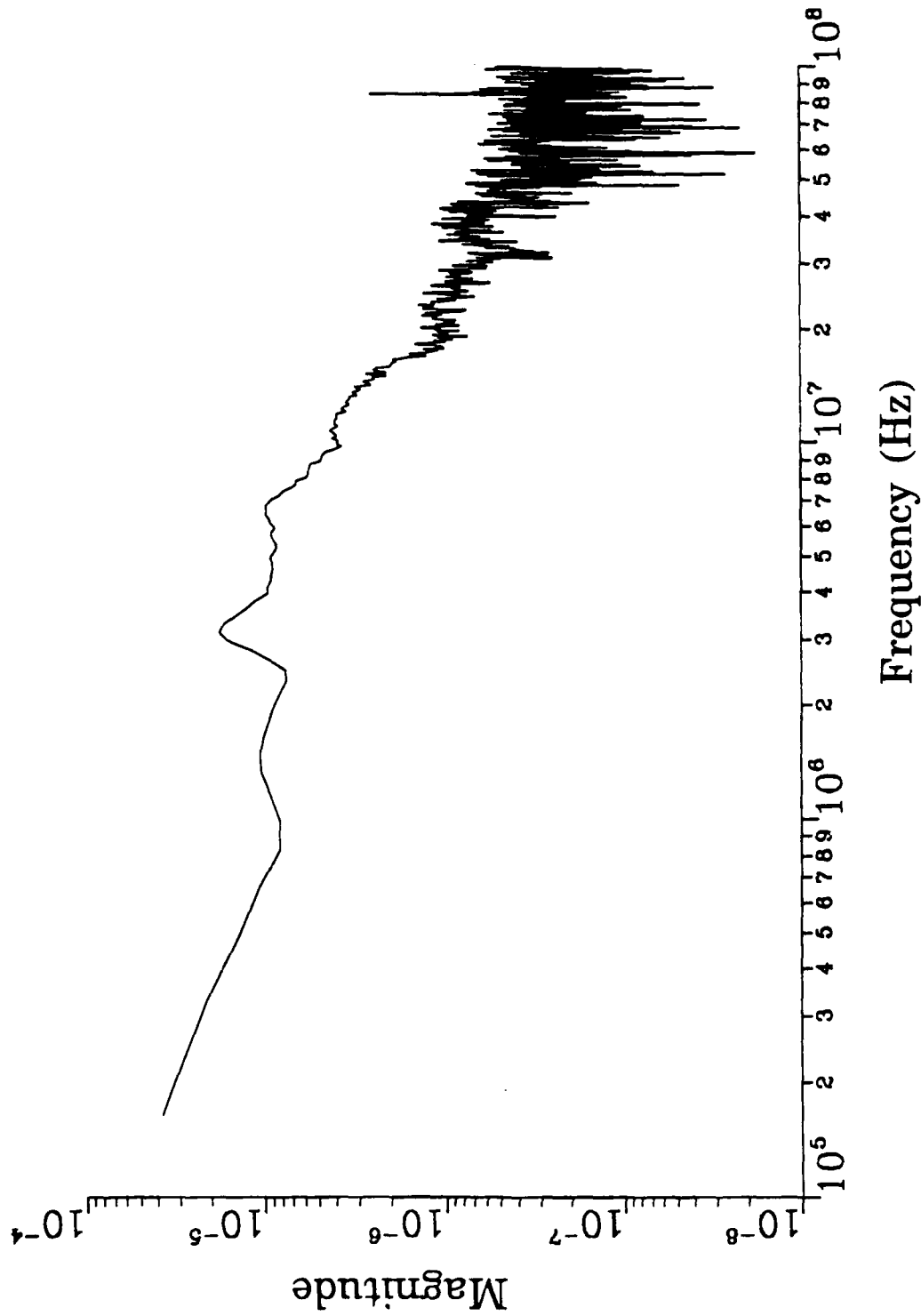


Figure 86. The EMPTAC surface current density on the top of the starboard wing (test point #8) (experimental data obtained from the HPD pulser, E ⊥ to fuselage).

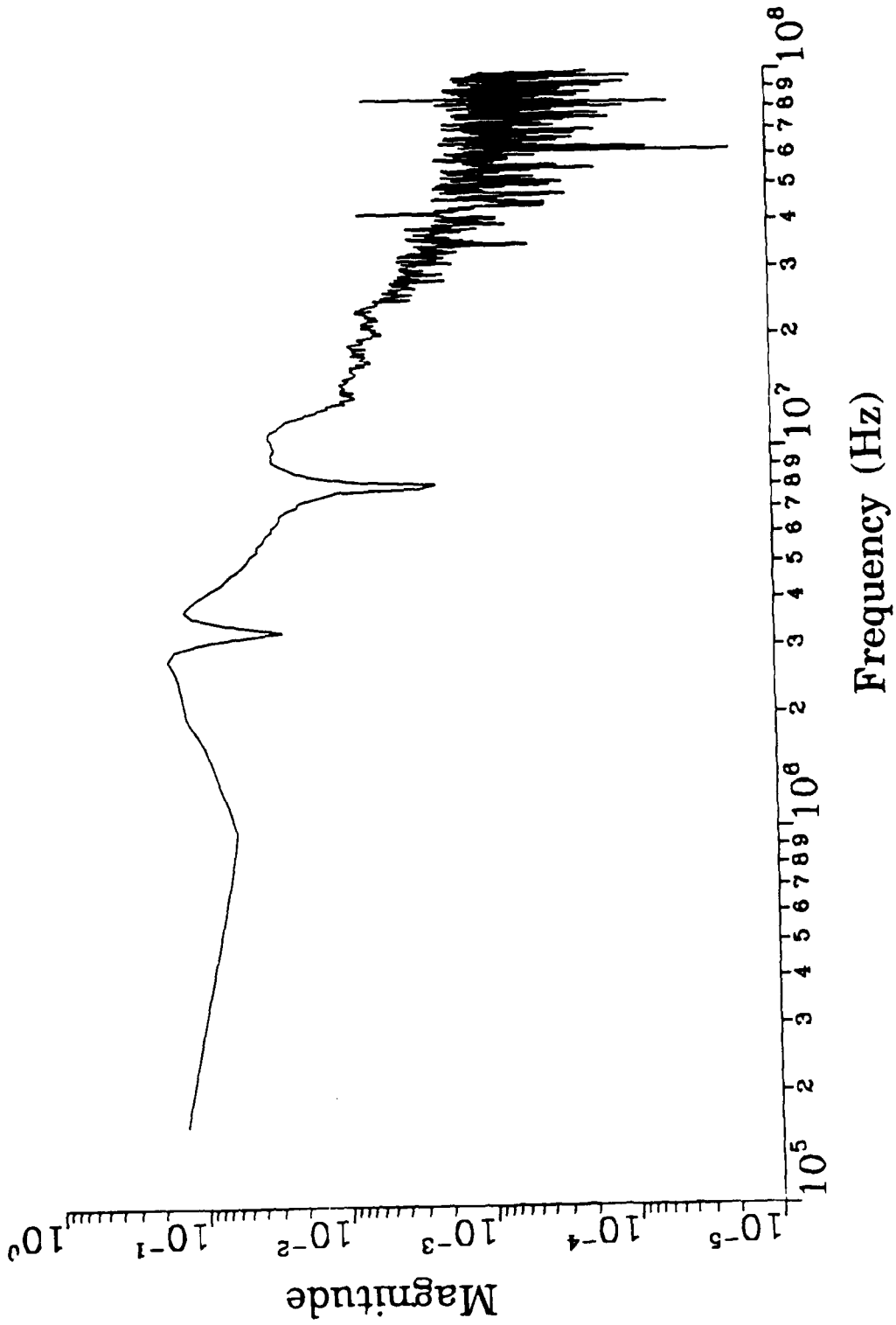


Figure 87. The EMPTAC surface charge density on the nose of the aircraft (test point #9) (experimental data obtained from the HPD pulser, E|| to fuselage).

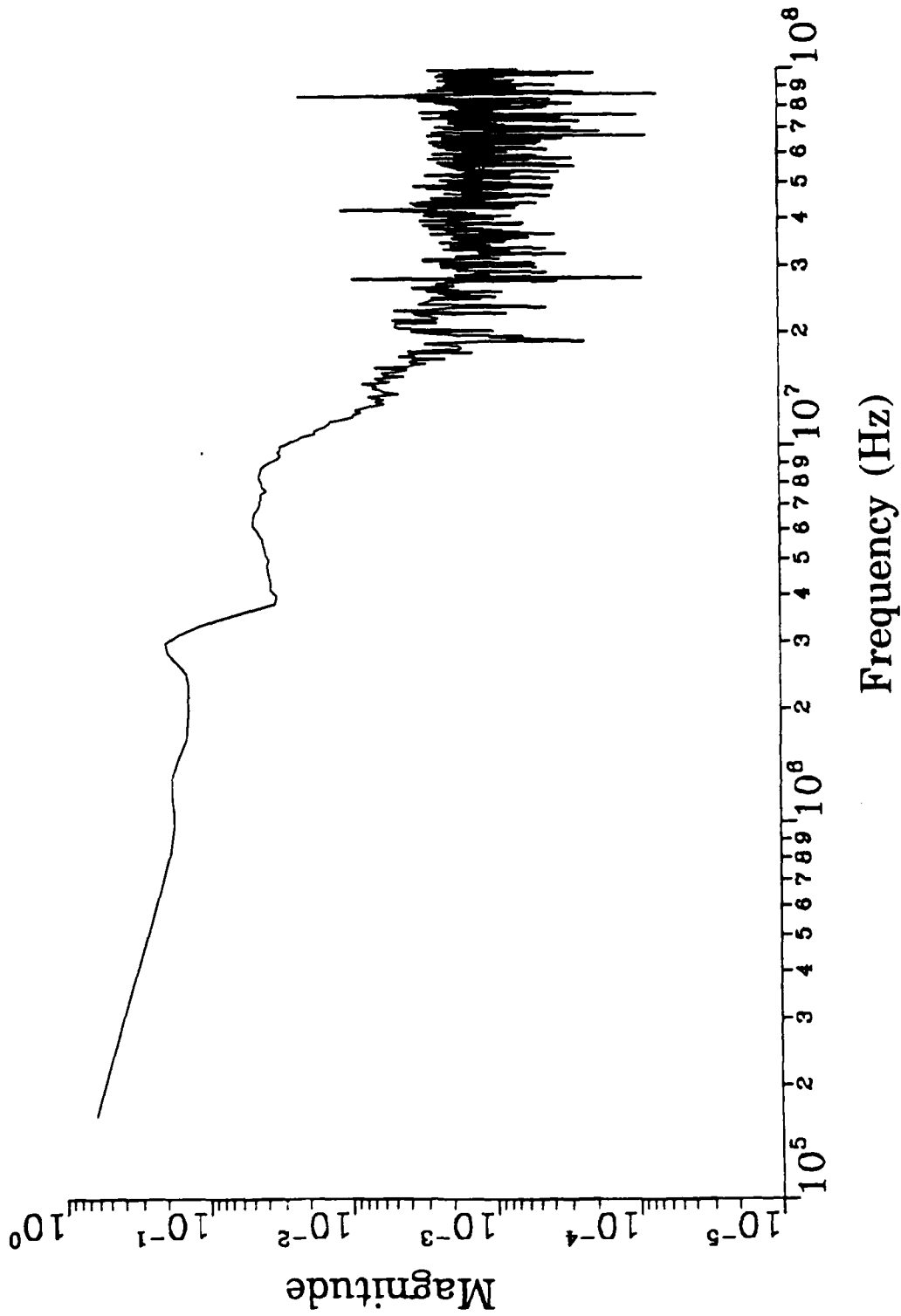


Figure 88. The EMPTAC surface charge density on the vertical stabilizer (test point #10) (experimental data obtained from the HPD pulser, E || to fuselage).

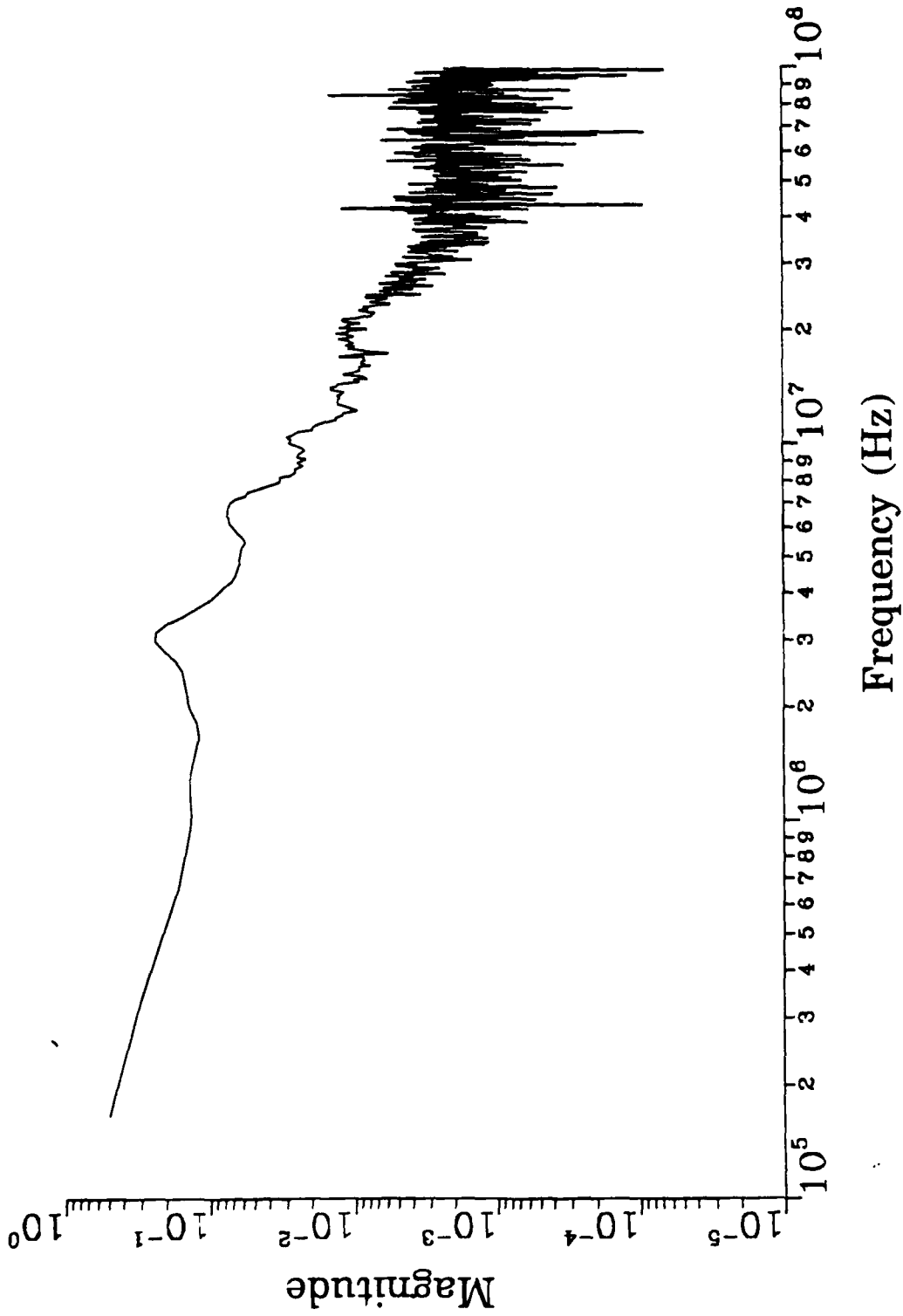


Figure 89. The EMPTAC surface charge density on the tip of the port wing (test point #11) (experimental data obtained from the HPD pulser, E  $\perp$  to fuselage).

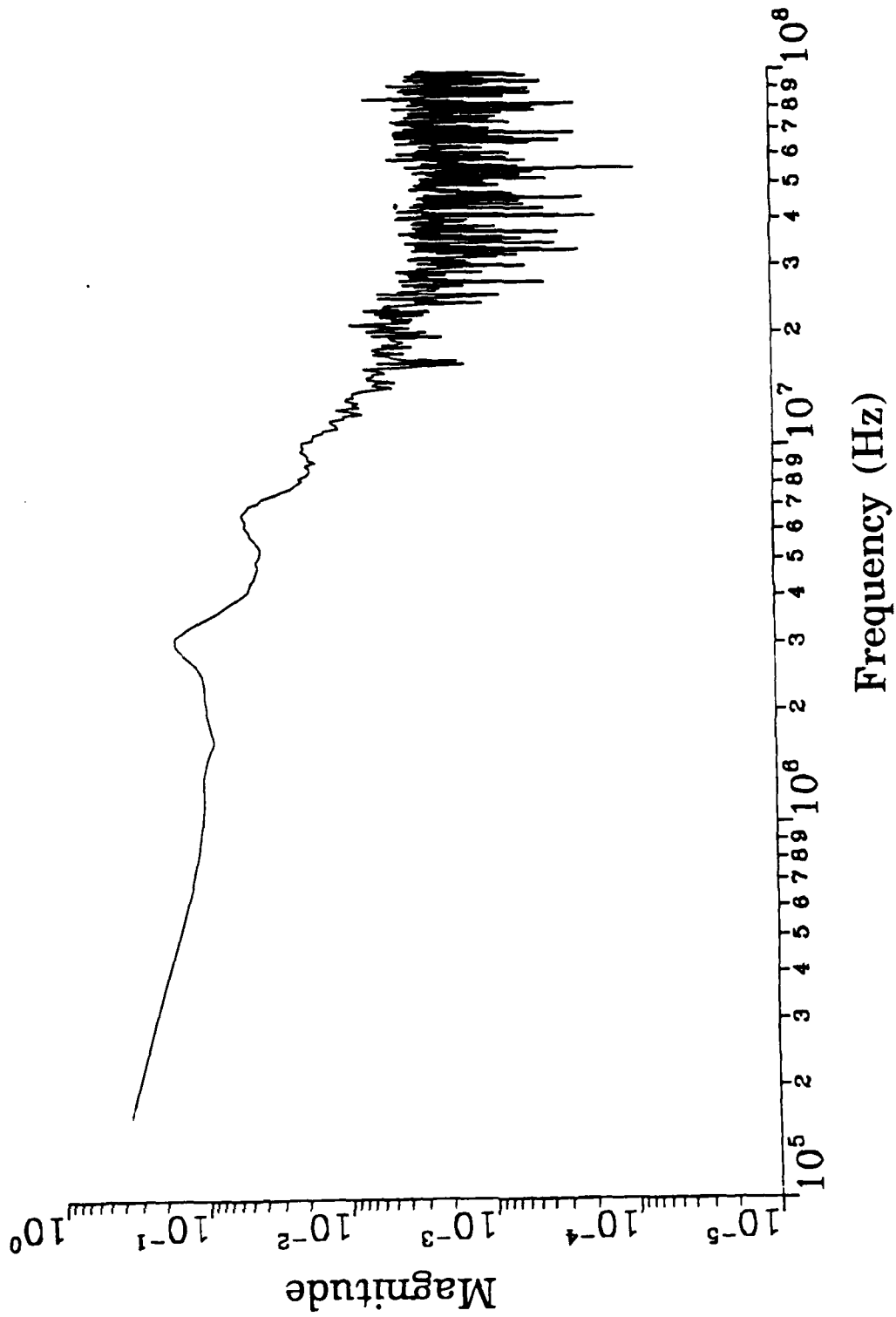


Figure 90. The EMPTAC surface charge density on the tip of the starboard wing (test point #12) (experimental data obtained from the HPD pulser, E 1 to fuselage).

## 6.0 COMPARISON OF THE EMPTAC NATURAL MODES EXCITED VIA PLANE WAVE AND HF ANTENNA EXCITATION

Given the frequency response data generated using the method-of-moments solution (0.5 to 20 MHz) of Section 3.0, the natural modes of the EMPTAC may be obtained numerically as shown by Taylor and Crow (Ref. 4). The two plane wave polarizations considered produce symmetric modes (electric field parallel to the fuselage) and antisymmetric modes (electric field perpendicular to the fuselage).

The general characteristics of the current distributions associated with the resonant frequencies of an aircraft are discussed in Reference 11. The fundamental resonance (lowest symmetric mode) of the EMPTAC is computed and found to be 2.54 MHz. This fundamental resonance is characterized by current flow over the entire length of the aircraft. The second symmetric mode is characterized by current flow over the wings and the front fuselage. The total length of one wing and the front fuselage is approximately one-half wavelength. The frequency of the second symmetric EMPTAC mode is determined to be 4.64 MHz. The frequencies of the third and fourth symmetric modes are 7.30 and 9.23 MHz, respectively. The fundamental antisymmetric frequency is lower than that of the second symmetric mode since the total length of both wings is larger than total length of one wing and the front fuselage. The frequency of the fundamental antisymmetric mode is 3.62 MHz while that of the second antisymmetric mode is 9.85 MHz.

The dominant symmetric EMPTAC resonances excited by a plane wave incident from above with the electric field parallel to the fuselage are determined numerically and shown in Table 6. Both the resonant frequency (MHz) and the associated damping constant ( $\mu s$ ) are given for each mode. Table 7 represents the corresponding antisymmetric resonances excited by a plane wave incident with the electric field perpendicular to the fuselage.

Certain symmetric and antisymmetric modes of the EMPTAC are excited using a given HF antenna configuration. The four dominant symmetric modes defined in Table 6 are excited when driving

Table 6. Dominant symmetric Modes of the EMPTAC obtained for plane wave excitation (E || to the fuselage).

Frequency (MHz)	Damping Constant ( $\mu$ s)
2.54	143
4.64	14.7
7.30	6.25
9.23	5.88

Table 7. Dominant antisymmetric modes of the EMPTAC obtained for plane wave excitation (E  $\perp$  to the fuselage).

Frequency (MHz)	Damping Constant ( $\mu$ s)
3.62	32.9
9.85	3.46

- the fin-cap antenna only
- the nose and fin-cap antennas
- the port and starboard wing antennas

The antisymmetric EMPTAC modes defined in Table 7 are excited only when the port wing antenna is driven. Using the port wing antenna excitation, the symmetric EMPTAC modes are also excited but to a lesser degree than the antisymmetric modes. Figures 91 and 92 show the normalized current density along the top of the forward fuselage for symmetric plane wave and HF antenna excitations at the first and second symmetric resonances, respectively. Figures 93 and 94 represent the corresponding normalized current densities along the top of the mid fuselage while Figures 95 and 96 represent those along the top of the port wing. Figures 97 and 98 represent the normalized current densities along the top of both wings for antisymmetric plane wave and HF antenna excitations.

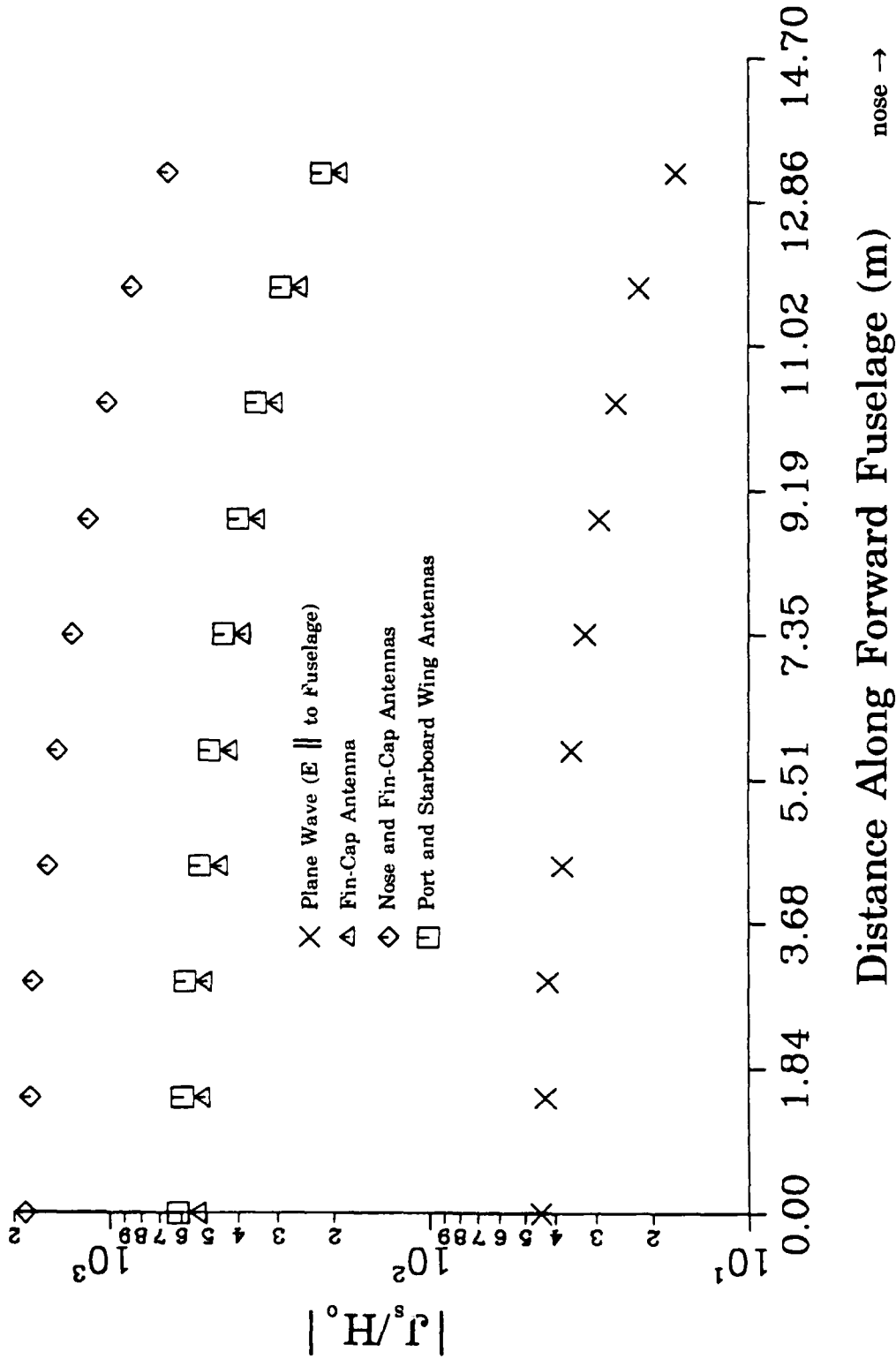


Figure 91. The EMPTAC normalized current density along the top of the forward fuselage at the first symmetric resonance (2.54 MHz) for symmetric plane wave and HF antenna excitations.

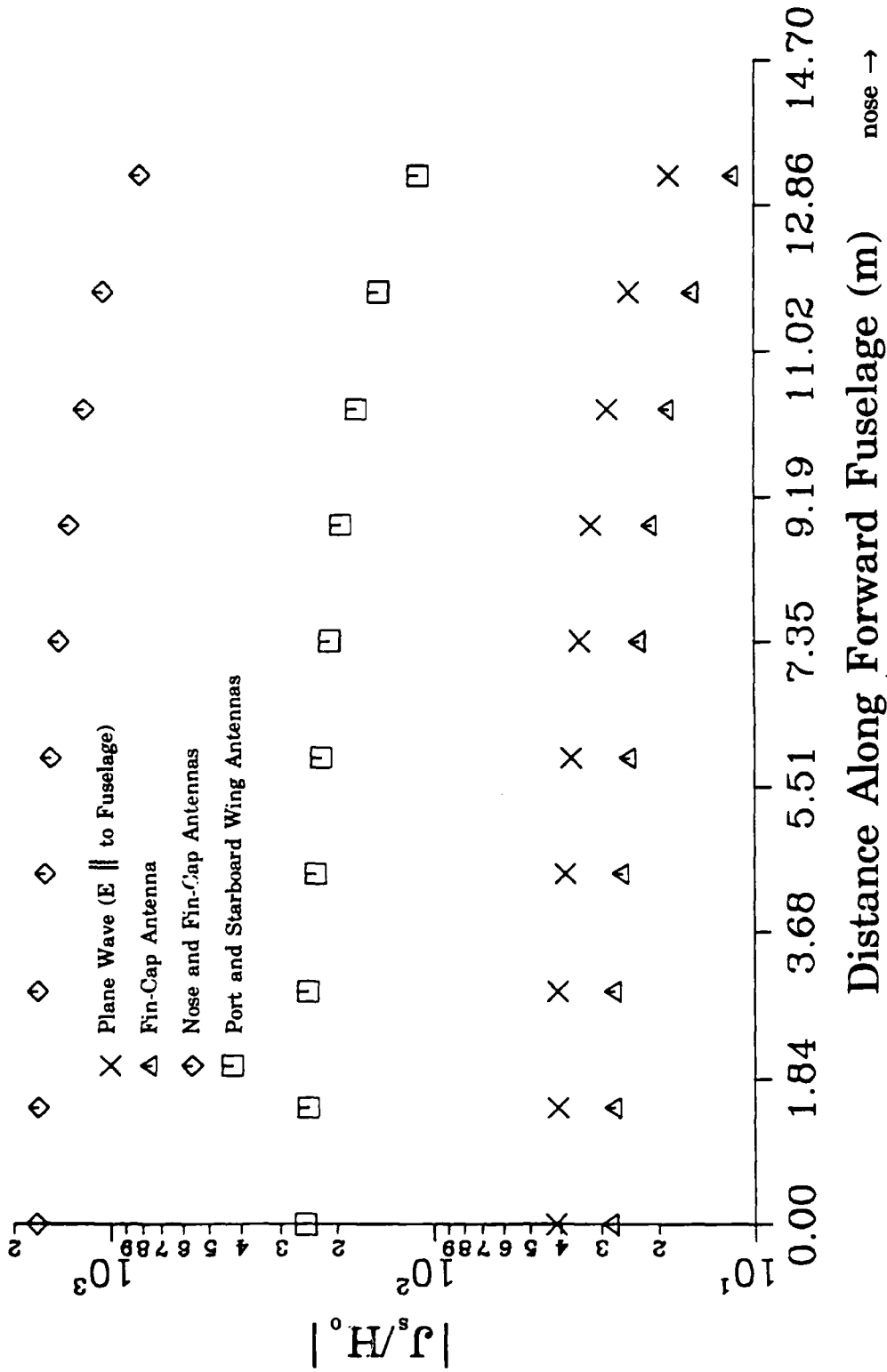


Figure 92. The EMPTAC normalized current density along the top of the forward fuselage at the second symmetric resonance (4.64 MHz) for symmetric plane wave and HF antenna excitations.

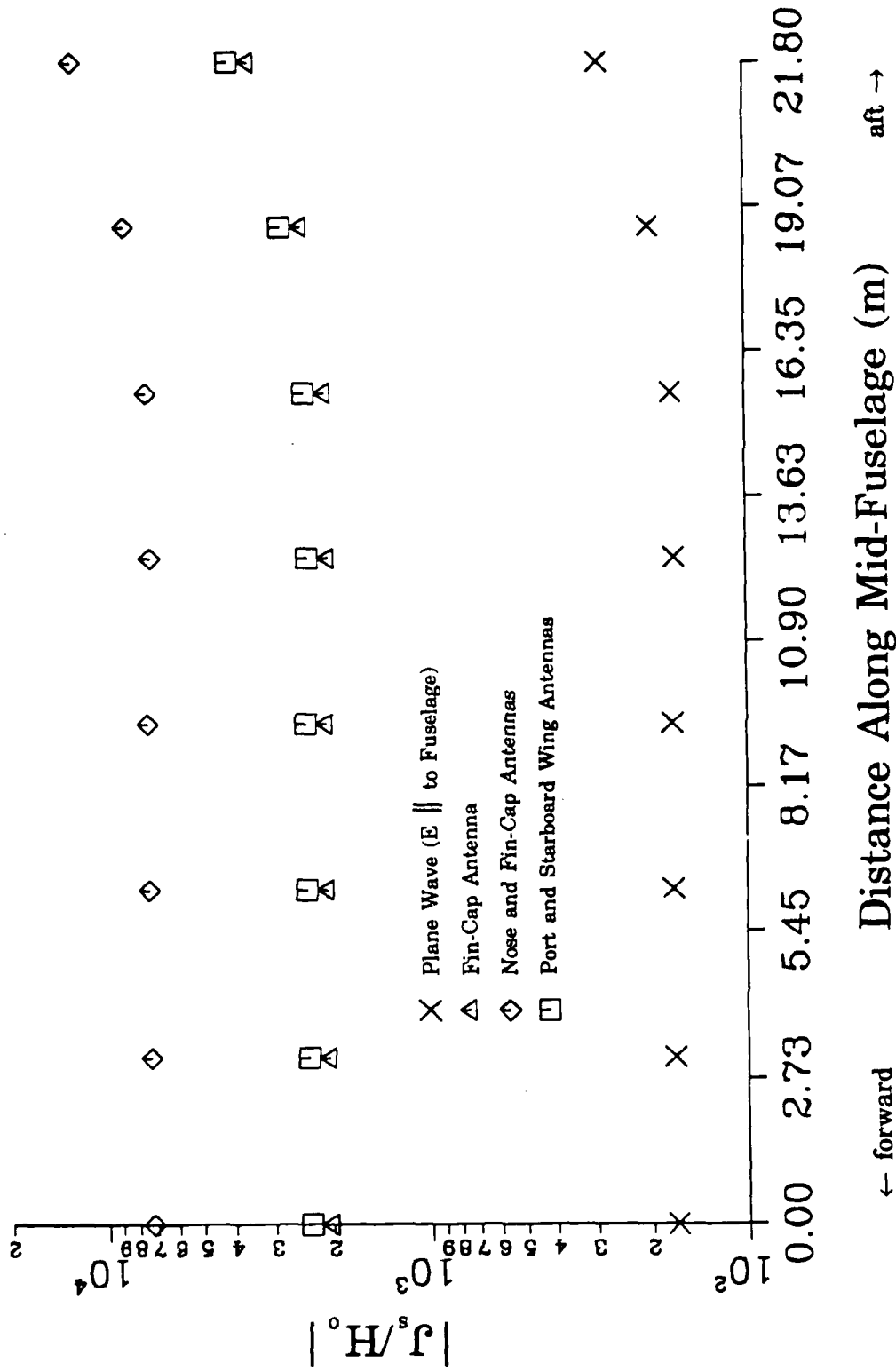


Figure 93. The EMPIAC normalized current density along the top of the mid fuselage at the first symmetric resonance (2.54 MHz) for symmetric plane wave and HF antenna excitations.

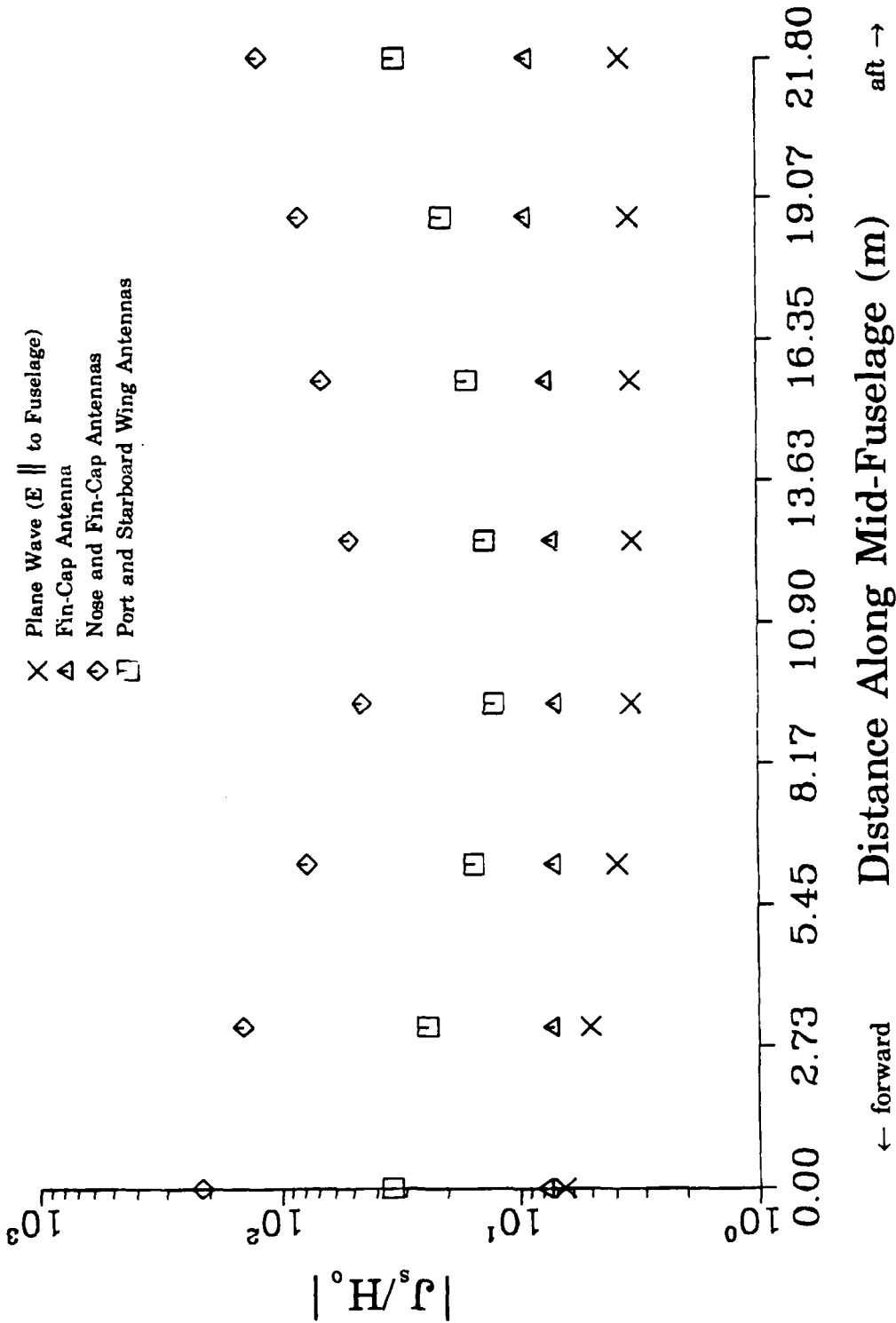


Figure 94. The EMPTAC normalized current density along the top of the mid fuselage at the second symmetric resonance (4.64 MHz) for symmetric plane wave and HF antenna excitations.





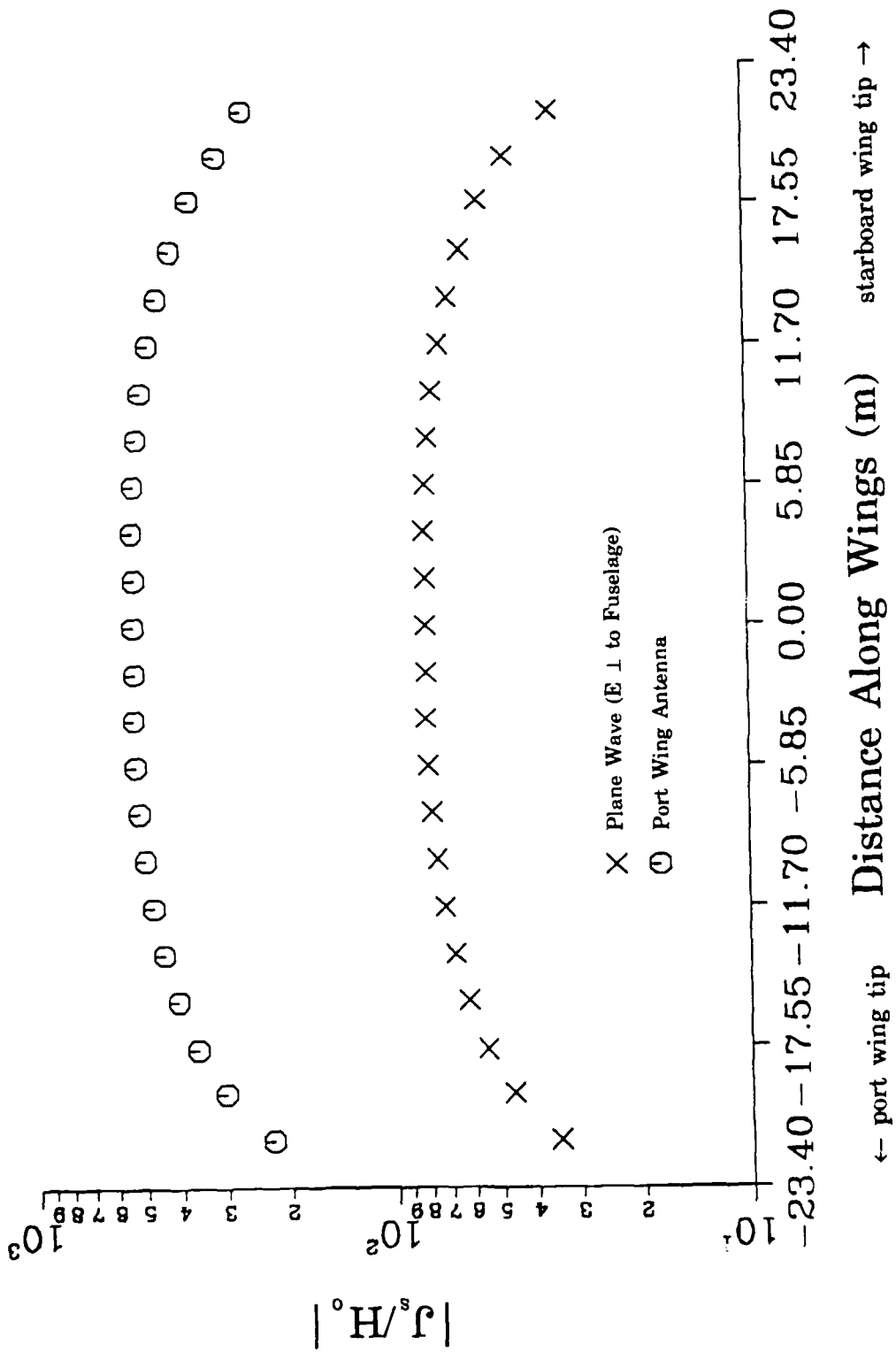


Figure 97. The EMPTAC normalized current density along the top of the wings at the first antisymmetric resonance (3.62 MHz) for antisymmetric plane wave and HF antenna excitations.

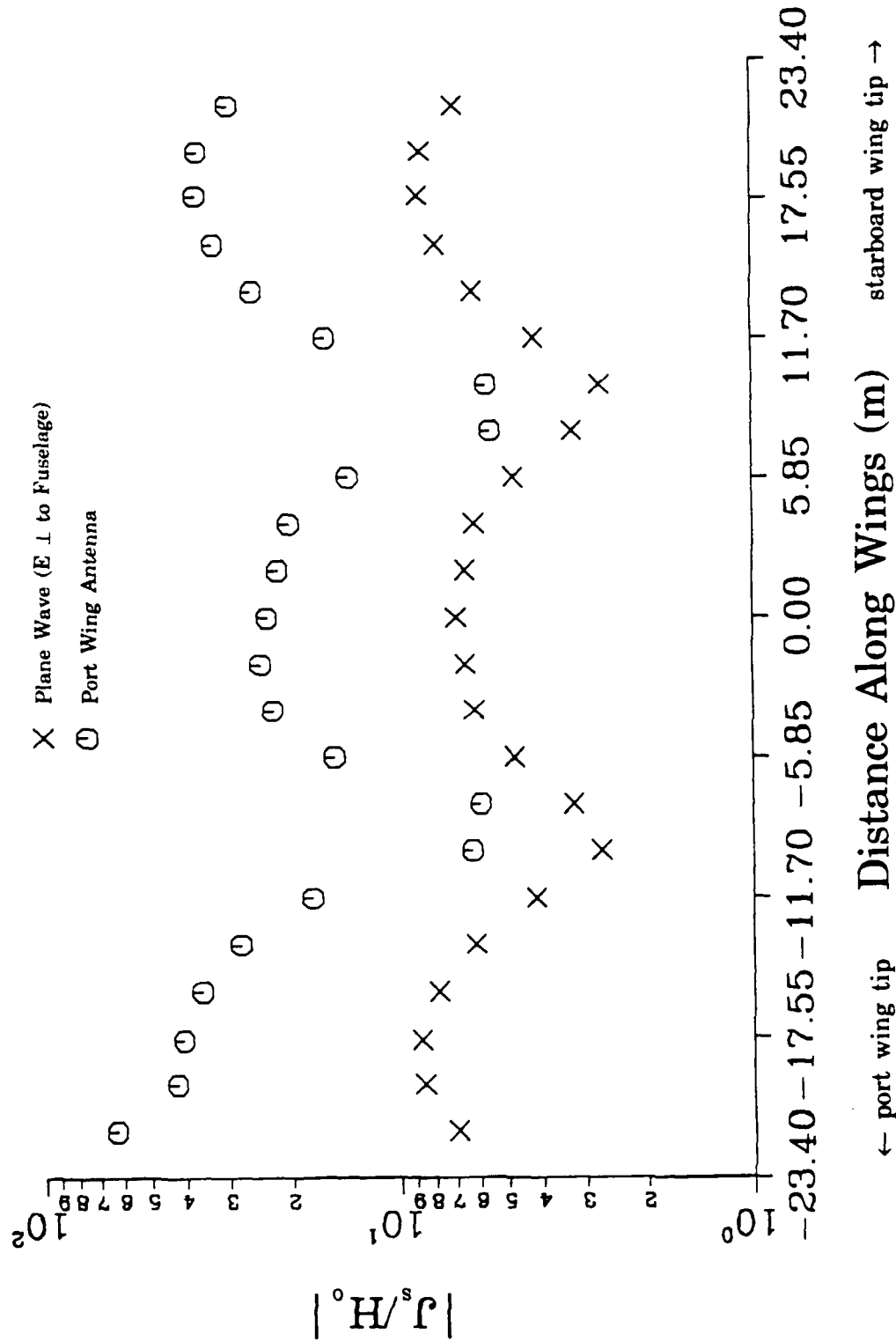


Figure 98. The EMPTAC normalized current density along the top of the wings at the second antisymmetric resonance (9.85 MHz) for antisymmetric plane wave and HF antenna excitations.

## 7.0 RESULTS AND CONCLUSIONS

The surface responses of the EMPTAC to excitation by a plane wave from overhead and various configurations of the onboard HF antennas have been determined. The outer surface of the EMPTAC was modelled as intersecting bodies of revolution. The method-of-moments formulation was used over a frequency range of 500 kHz to 20 MHz while the physical optics approximation was employed between 20 and 100 MHz. Using the frequency responses obtained from the method-of-moments formulation, the dominant symmetric and antisymmetric modes of the EMPTAC produced by plane wave excitation are identified in the surface responses caused by various HF antenna excitations.

The surface responses obtained in Section 3.0 for plane wave and HF antenna excitation exhibit dissimilar magnitudes at low frequencies. This difference in magnitude is caused by the constant radiated power constraint ( $P_{\text{rad}} = 10 \text{ W}$ ) used to model the active HF antennas as discussed in paragraph 3.2. To radiate an average power of 10 W at low frequencies requires a very large antenna drive current which in turn produces large incident field magnitudes in comparison to the assumed plane wave fields ( $E_0 = 1 \text{ V/m}$ ). As the frequency is increased, the radiation resistance of the antenna (dipole,  $h = 2 \text{ m}$ ) increases such that the drive current required to radiate 10 W decreases to a level which produces incident field magnitudes comparable to that of the plane wave case. Thus, the magnitudes of the HF antenna responses at higher frequencies approach those of the plane wave responses.

The symmetric HF antenna drive configurations considered (fin-cap antenna only, nose and fin-cap antennas, and port and starboard wing antennas) give rise to the symmetric modes (those modes generated by symmetric plane wave excitation). The antisymmetric HF antenna drive configuration (port wing antenna only) gives rise to both symmetric and antisymmetric modes with the antisymmetric modes being dominant. Certain HF antenna drive configurations enhance specific modes. For example, the nose and fin-cap antenna excitation generates the second symmetric resonance (4.64 MHz) more efficiently than the fin-cap antenna alone. The port wing antenna excitation does not produce the fundamental resonance as efficiently as the other HF antenna drive configurations. In many cases, certain higher order resonances are enhanced by driving

the HF antennas. Each HF antenna drive configuration considered enhanced the third symmetric resonance (7.30 MHz) when compared to the corresponding plane wave response.

The physical optics approximation (20 to 100 MHz) predicts constant-valued responses to plane wave excitation due to the spatially invariant field magnitudes with frequency. However, the physical optics approximation predicts variation in the surface responses to HF antenna excitation caused by the spatial variation of the incident field with frequency.

The general shape of the measured responses given in Section 5.0 resembles the inflight mode responses to a greater extent than the ground alert responses. Due to the effects of a lossy ground plane beneath the aircraft, the actual response curve should follow the inflight mode results with slightly higher resonant peaks and small shifts in the resonant frequencies. The effect of the antenna lengths on the actual EMPTAC resonant frequencies are not included in this research since the antenna models were assumed to be electrically isolated from the aircraft. However, because the antenna lengths are small in comparison to the individual elements of the aircraft, the shifts in the dominant resonant frequencies should be small. The shifts in the locations of the resonant frequencies due to antenna lengths should become more pronounced at the higher order modes.

## REFERENCES

1. Hoeft, L. O. and Prather, W. D., "Single Point Excitation - A New Technique for Exciting Aircraft for Hardness Surveillance Measurement," Proceedings of the 6th International Conference on Electromagnetic Compatibility, Seattle, Washington, September 1988.
2. Hoeft, L. O., "Refinement of the SPEHS Technique for Application to the E-3A," 402-RTa-88-002, BDMMSC, December 1988.
3. Taylor, C. D., "External Interaction of the Nuclear EMP with Aircraft and Missiles," IEEE Transactions on Electromagnetic Compatibility, Vol. EMC-20, No. 1, pp. 64-76, February 1978.
4. Taylor, C. D. and Crow, T. T., "Calculation of Natural Resonances for Perpendicularly Crossed Wires Parallel to an Imperfect Ground," Electromagnetics, Vol. 3 No. 1, pp. 41-64, January-March 1983.
5. Chen, K. T., "A Study of the EMP Interaction with Aircraft Using Intersecting Bodies of Revolution as a Model", Ph.D Dissertation, Mississippi State University, August 1976.
6. Taylor, C. D. and Wilton, D. R., "The Extended Boundary Condition Solution of the Dipole Antenna of Revolution," IEEE Transactions on Antennas and Propagation, Vol. AP-20, pp. 772-776, November 1972.
7. Wu, T. T. and King, R. W. P., "The Tapered Antenna and Its Application to the Junction Problem for Thin Wires," IEEE Transactions on Antennas and Propagation, Vol. AP-24, No. 1, pp. 42-45, January 1976.
8. Taylor, C. D., "A Simple Procedure for Estimating the Current Induced on Cylinder-Like Conductors Illuminated by EMP," AFWL Interaction Note 176, Air Force Weapons Laboratory, Kirtland AFB, New Mexico, July 1973.
9. Hoeft, L. O., Hofstra, J. S., and Prather, W. D., "Excitation of Aircraft Hardness Surveillance Using the Aircraft's Own HF Antenna," 1989 IEEE National Symposium on Electromagnetic Compatibility, Denver, Colorado, May 1989.
10. King, R. W. P., The Theory of Linear Antennas, Harvard University Press, Cambridge, Massachusetts, 1956.
11. Lee, K. S. H., ed., EMP Interaction: Principles, Techniques, and Reference Data, Hemisphere Publishing, New York, 1986.